

UNIVERSITY OF CALIFORNIA

Los Angeles

Study and optimization of turbulence and transport in mirror configurations in the Large Plasma  
Device

A dissertation submitted in partial satisfaction  
of the requirements for the degree  
Doctor of Philosophy in Physics and Astronomy

by

Philip Nathanael Travis

2025



## ABSTRACT OF THE DISSERTATION

Study and optimization of turbulence and transport in mirror configurations in the Large Plasma  
Device

by

Philip Nathanael Travis  
Doctor of Philosophy in Physics and Astronomy  
University of California, Los Angeles, 2025  
Professor Troy Carter, Chair

Abstract

The dissertation of Philip Nathanael Travis is approved.

Paulo Alves

Christoph Niemann

Jacob Bortnik

Troy Carter, Committee Chair

University of California, Los Angeles

2025

To humanity, I guess  
and Altair, my dog

## TABLE OF CONTENTS

<b>1</b>	<b>Introduction</b>	<b>1</b>
1.1	Nuclear fusion: a brief introduction	1
1.2	Mirror machines as a faster way to fusion power	1
1.3	Machine learning as a faster way to fusion power	1
<b>2</b>	<b>Background</b>	<b>2</b>
2.1	Mirror machines	2
2.2	The Large Plasma Device at UCLA	2
2.2.1	Plasma source	2
2.2.2	Magnetic field	3
2.2.3	Gas fueling	3
2.3	Data acquisition	4
2.4	Diagnostics	5
2.4.1	Langmuir probes: $I_{\text{sat}}$ , sweeps, triple probes	5
2.4.2	Bdot probes	5
2.4.3	The 288 GHz heterodyne interferometer	5
2.4.4	Thomson scattering	6
2.4.5	Fast framing camera	6
2.5	Instabilities in mirrors and the LAPD	6
2.5.1	Rotational interchange	6
2.5.2	Drift waves	6
2.5.3	Interchange	6

2.6	Machine learning and neural networks . . . . .	6
2.6.1	Fundamentals of neural networks . . . . .	7
2.6.2	Common architectures . . . . .	7
<b>3</b>	<b>Turbulence and transport in mirror geometries in the Large Plasma Device . . . . .</b>	<b>8</b>
3.1	Introduction . . . . .	9
3.2	The experiment and device configuration . . . . .	11
3.2.1	The Large Plasma Device (LAPD) . . . . .	11
3.2.2	Diagnostics . . . . .	12
3.3	Mirror-induced changes . . . . .	13
3.3.1	Profile modification . . . . .	13
3.3.2	Reduced particle flux . . . . .	17
3.3.3	Compensating for the Te profile . . . . .	26
3.3.4	Drift waves . . . . .	28
3.3.5	Turbulence modification . . . . .	34
3.3.6	Magnetic fluctuations . . . . .	35
3.4	2d Structure . . . . .	41
3.5	Discussion . . . . .	47
3.5.1	Lack of mirror-driven instabilities . . . . .	47
3.5.2	Instabilities driving LAPD turbulence . . . . .	51
3.5.3	Causes of particle flux reduction . . . . .	53
3.5.4	Differences between DR1 and DR2 . . . . .	56
3.6	Conclusions and future work . . . . .	59

<b>4</b>	<b>Creating a randomized dataset for machine learning tasks . . . . .</b>	<b>61</b>
4.1	Goal and introduction . . . . .	61
4.2	Configuration of the LAPD . . . . .	62
4.3	Signals collected . . . . .	64
4.4	Data cleaning . . . . .	68
4.5	Data bias . . . . .	69
4.6	Azimuthal asymmetry of probe data . . . . .	74
4.7	Applying and improving the dataset . . . . .	75
<b>5</b>	<b>Optimizing mirror configurations in the LAPD using machine learning . . . . .</b>	<b>76</b>
5.1	Introduction . . . . .	76
5.2	Processing of $I_{\text{sat}}$ signals . . . . .	79
5.3	Model development and training . . . . .	82
5.3.1	Model inputs . . . . .	82
5.3.2	Training details . . . . .	83
5.3.3	Validating the training pipeline . . . . .	83
5.3.4	Baselines for mean-squared error . . . . .	84
5.3.5	Effects of training set and model sizes . . . . .	88
5.3.6	Improving performance with machine state flags . . . . .	88
5.3.7	Learning rate scheduling . . . . .	89
5.4	Uncertainty quantification . . . . .	89
5.4.1	$\beta$ -NLL loss . . . . .	89
5.4.2	Cross-validation MSE . . . . .	90
5.4.3	Model calibration via weight decay . . . . .	92

5.5	Evaluating model performance . . . . .	97
5.5.1	Checking geometrical intuition . . . . .	97
5.5.2	Directly comparing prediction to measurement . . . . .	99
5.5.3	Comparison with Thomson scattering . . . . .	101
5.6	Effect of $I_{\text{sat}}$ calibration . . . . .	102
5.7	Inferring trends . . . . .	104
5.8	Optimizing profiles . . . . .	107
5.9	Discussion . . . . .	113
5.9.1	Key achievements . . . . .	113
5.9.2	Current limitations . . . . .	114
5.9.3	Future directions . . . . .	115
5.10	Conclusion . . . . .	115
5.11	The open dataset and repository . . . . .	116
<b>6</b>	<b>Reconstructing missing diagnostics using energy-based models</b> . . . . .	<b>117</b>
6.1	Introduction . . . . .	117
6.2	Problem statement . . . . .	120
6.3	Data preparation . . . . .	120
6.3.1	Architecture . . . . .	124
6.3.2	Training tips . . . . .	124
6.4	Unconditional sampling . . . . .	124
6.5	Conditional sampling of interferometer signals . . . . .	124
6.6	Symmetries and trends in the energy function . . . . .	131
6.6.1	Positional symmetry . . . . .	131

6.7	Future work . . . . .	131
<b>7</b>	<b>Conclusions . . . . .</b>	<b>133</b>
7.1	Future Directions . . . . .	133
<b>A</b>	<b>Evidence for the interchange instability in the LAPD . . . . .</b>	<b>134</b>
<b>B</b>	<b>Acquiring a 29 million shot dataset for machine learning . . . . .</b>	<b>135</b>
B.1	Brief introduction to energy-based models (EBMs) . . . . .	135
B.2	Building a 15 million shot dataset . . . . .	135
B.3	Training the model . . . . .	137
B.4	Unconditional sampling . . . . .	137
B.5	Reconstructing missing diagnostics via conditional sampling . . . . .	137
B.6	Inferring trends and outlook . . . . .	137
<b>C</b>	<b>0D mirror optimization . . . . .</b>	<b>138</b>
C.1	List of assumptions / conditions . . . . .	139
C.2	User specified parameters . . . . .	140
C.2.1	Simple mirror endplug . . . . .	140
C.2.2	Tandem mirror . . . . .	141
C.2.3	Engineering parameters . . . . .	141
C.3	Fusion . . . . .	142
C.3.1	Reactivity . . . . .	142
C.3.2	Fusion power . . . . .	143
C.4	General formulae . . . . .	146

C.5	Radial particle transport . . . . .	148
C.5.1	Classical diffusion . . . . .	149
C.5.2	Bohm diffusion . . . . .	149
C.5.3	Gyro-Bohm diffusion . . . . .	150
C.5.4	ETG-driven transport . . . . .	150
C.6	Mirror-specific derived quantities . . . . .	151
C.6.1	Temperatures and confinement time in a beam-heated mirror from Egedal et al 2022 [EEF22] . . . . .	151
C.6.2	Confinement time given by classical transport . . . . .	153
C.6.3	End Cells/Plugs . . . . .	154
C.6.4	Tandem mirror — central cell . . . . .	158
C.6.5	Overall power balance and plant power estimates . . . . .	160
C.6.6	Instabilities . . . . .	161
C.7	Costs and economics . . . . .	162
C.7.1	Heating . . . . .	162
C.7.2	Magnets . . . . .	162
C.8	Optimization constraints . . . . .	163
C.8.1	Midplane fields regularization via alpha particle confinement penalties . . .	163
C.8.2	Kunal’s suggestions . . . . .	164
C.9	Optimizing mirror configurations . . . . .	165
C.9.1	Gradient descent using SymPy and JAX . . . . .	165
C.9.2	Example: optimizing Q in a simple mirror . . . . .	166
<b>D</b>	<b>Automated Langmuir sweep analysis using machine learning . . . . .</b>	<b>170</b>

E Wisdom acquired . . . . .	171
<b>References . . . . .</b>	<b>172</b>

## LIST OF FIGURES

3.1	Cartoon of the mirror turbulence experiment setup . . . . .	12
3.2	Raw data processing steps . . . . .	14
3.3	Shot-to-shot variation of $I_{\text{sat}}$ profiles . . . . .	17
3.4	Midplane $I_{\text{sat}}$ profile . . . . .	18
3.5	Line-integrated density . . . . .	19
3.6	$T_e$ from Langmuir sweeps at the midplane . . . . .	20
3.7	Plasma potential and derived $\mathbf{E} \times \mathbf{B}$ velocity profiles . . . . .	21
3.8	$I_{\text{sat}}$ and $B_{\perp}$ fluctuation power profiles . . . . .	22
3.9	Cross-field, $\tilde{\mathbf{E}} \times \mathbf{B}$ particle flux . . . . .	24
3.10	Phase and coherency of $I_{\text{sat}}$ current and Vf near $x_{PF}$ . . . . .	25
3.11	Swept vs triple probe measurements . . . . .	27
3.12	Triple probe Te and Te fluctuation profiles . . . . .	27
3.13	Diffusivity relative to $D_B$ . . . . .	28
3.14	Diffusivity with Te compensation relative to $D_B$ . . . . .	29
3.15	$I_{\text{sat}}$ gradients under varying profile smoothing methods . . . . .	29
3.16	$I_{\text{sat}}$ (density) fluctuation power . . . . .	30
3.17	$k_{\parallel}$ and coherency $\gamma$ . . . . .	31
3.18	Normalized density fluctuations vs $\rho_s/L_n$ . . . . .	32
3.19	$I_{\text{sat}}$ scaled by $L_n^2/n^2$ . . . . .	33
3.20	Fluctuation power summed for each $k_y$ . . . . .	34
3.21	$B_{\perp}$ fluctuation power spectra at various locations . . . . .	36
3.22	$B_{\perp}$ fluctuation power profiles for three regions . . . . .	38

3.23	Summed fluctuation power of $B_{\perp}$ in the core . . . . .	39
3.24	$B_{\perp}$ , flat field 500G vs 400G . . . . .	40
3.25	$B_{\perp}$ fluctuations at $x=0$ for different mirror lengths . . . . .	41
3.26	$B_z$ fluctuations in the core and $x_{PF}$ . . . . .	42
3.27	$B_{\perp}$ fluctuation power profiles for low frequencies . . . . .	43
3.28	$B_z$ fluctuation power profiles for low frequencies . . . . .	44
3.29	2d plane of the perpendicular magnetic field and the derived current density for $M = 1$	45
3.30	Perpendicular magnetic field and the derived current density for the $M = 1.9$ and $M = 2.68$ cases . . . . .	46
3.31	Azimuthal mode number $m$ amplitudes of $I_{\text{sat}}$ fluctuations . . . . .	48
3.32	$k_y$ averaged about $x_{PF}$ . . . . .	49
3.33	Gradient scale length $L_n$ . . . . .	52
3.34	Particle flux: breakdown into components . . . . .	54
3.35	$I_{\text{sat}}$ decorrelation time . . . . .	55
3.36	ExB shearing rate . . . . .	56
3.37	Discharge power vs mirror ratio . . . . .	57
3.38	$I_{\text{sat}}$ profiles ( $M=1$ ), DR1 vs DR2 . . . . .	58
3.39	Line integrated density, DR1 vs DR2 . . . . .	58
3.40	$I_{\text{sat}}$ calibration factor over runs . . . . .	59
4.1	A demonstration of Latin-hypercube sampling vs random sampling . . . . .	63
4.2	LAPD configuration and diagnostics for the ML datarun . . . . .	66
4.3	Example machine state information and diagnostic signals . . . . .	67
4.4	Example interferometer skips . . . . .	69

4.5	Cleaning Thomson scattering spectra . . . . .	70
4.6	Time-averaged $I_{\text{sat}}$ distribution over shots . . . . .	71
4.7	Distribution of probe x-coordinates in the dataset . . . . .	72
4.8	y-axis profile before and after shifting the y-coordinate . . . . .	74
5.1	Cartoon of the experiment setup . . . . .	79
5.2	$I_{\text{sat}}$ traces from the swept probe . . . . .	80
5.3	Gas puff timings and example $I_{\text{sat}}$ time series at three different z-axis locations from three different dataruns. Note that some discharges do not achieve steady state in $I_{\text{sat}}$ . . .	81
5.4	Examples of $I_{\text{sat}}$ profiles from DR2 . . . . .	82
5.5	Training and validation losses when overfitting the model . . . . .	84
5.6	Linear predictions of $I_{\text{sat}}$ profiles . . . . .	86
5.7	The loss and MSE for the training, validation, and test sets . . . . .	91
5.8	Cross-validation test set error . . . . .	93
5.9	Cross-validation training set error . . . . .	93
5.10	Z-score distributions for the training and test sets for $\lambda = 0$ . . . . .	94
5.11	Model performance and calibration for different weight decays . . . . .	95
5.12	Model extrapolation performance and uncertainty . . . . .	96
5.13	Mirror configuration predictions scaled to the cathode radius . . . . .	98
5.14	Predictions compared with validation dataruns . . . . .	100
5.15	Comparison of original DR2 profiles with the profiles from DROpt . . . . .	102
5.16	Comparison of $I_{\text{sat}}$ predictions with Thomson scattering measurements . . . . .	103
5.17	Discharge voltage scan: effect on x and z profiles . . . . .	105
5.18	Predictions of axial gradient . . . . .	106

5.19 Optimized axial profiles, predicted and measured . . . . .	110
6.1 Distribution of batches in replay buffer samples . . . . .	123
6.2 EBM arch . . . . .	125
6.3 Blocks used in the EBM arch . . . . .	126
6.4 Training curves . . . . .	127
6.5 Unconditional samples of diode 3 at 16 ms and the mirror coil magnetic field inputs, chosen as representative examples. The EBM learns all modes of the distributions, though the probability mass is not well-aligned. . . . .	128
6.6 Left: all scaled inputs from the training set vs samples inputs. The distributions are similar, but the EBM does not appear to learn more extreme values. Right: corresponding energy distribution. The EBM learns all the modes, but the probability mass is not properly distributed. . . . .	128
6.7 MCMC energies, gradients, and integrated trajectory length for unconditional samples. Left: the model converges after approximately 50 sampling steps. Middle: the gradients approach an asymptote; long-term samples are realistic. Right: integrated trajectory length show that individual MCMC trajectories vary in total distance traveled along the energy surface. . . . .	129
6.8 Reconstructing the interferometer signal for a test-set datarun. Given only the inputs (left), the interferometer signal reconstruction uncertainty is quite large with many possible modes. When given other diagnostics signals, the RMSE improves by $1 \times 10^{17}$ m <sup>-2</sup> , but the uncertainty increases. If the model is sampled by instead initializing all inputs on real data and freezing the gradients (right), the model produces unphysical results and is poorly calibrated. The datarun chosen (DR2_02) is representative of performance across the test set. . . . .	130
6.9 . . . . .	131

C.1	DT reactivities . . . . .	143
C.2	DD reactivities . . . . .	144
C.3	DT, DD, and D-He3 reactivity comparison . . . . .	144
C.4	Simple mirror: cost function and gradient magnitude for each step . . . . .	167
C.5	Simple mirror: magnetic fields for each step . . . . .	168
C.6	Simple mirror: fusion power and Q for each step . . . . .	168
C.7	Simple mirror: temperatures for each step . . . . .	169

## LIST OF TABLES

3.1	Magnetic mirror lengths and ratios . . . . .	13
3.2	LAPD plasma parameters . . . . .	15
3.3	$x_c$ and $x_{PF}$ locations for each mirror ratio . . . . .	16
4.1	Data breakdown by class and dataset (percent) . . . . .	73
5.1	Summary of test set losses for different training data and ensembles . . . . .	87
5.2	Machine inputs and actuators for model inference . . . . .	108
5.3	Machine inputs and actuators for optimized axial profiles . . . . .	111

## ACKNOWLEDGMENTS

I acknowledge peeps

## VITA

- 2017      B.S. (Engineering Physics), University of Illinois at Urbana-Champaign
- 2018      Masters (Physics), University of California, Los Angeles
- 2025      Ph.D. (Plasma Physics), University of California, Los Angeles

## PUBLICATIONS

Pubs

# **CHAPTER 1**

## **Introduction**

**1.1 Nuclear fusion: a brief introduction**

**1.2 Mirror machines as a faster way to fusion power**

**1.3 Machine learning as a faster way to fusion power**

# CHAPTER 2

## Background

### 2.1 Mirror machines

### 2.2 The Large Plasma Device at UCLA

The Large Plasma Device (LAPD)[GPL16a, QGP23a] is a 26 meter long linear plasma device located Basic Plasma Science Facility (BaPSF) at the University of California, Los Angeles. This device is built for basic plasma science and can create quiescent, long-lived (read: longer than the timescales of interest) plasmas. The LAPD produces up to 18 m long, 1 m diameter plasmas.

#### 2.2.1 Plasma source

Typically, plasmas are produced using a hot cathode and anode at the south end of the device. This cathode was originally barium oxide (BaO)-plated nickel [GPL16a], but was recently upgrade to a segmented lanthanum hexaboride ( $\text{LaB}_6$ ) source [QGP23a]. The BaO cathode was 72 cm in diameter which mapped to 60 cm in a flat field magnetic field configuration. A 72 cm diameter, 50% transparent molybdenum anode was used to accelerate electrons from the cathode down the length of the machine. This BaO source could reach densities of  $4 \times 10^{12} \text{ cm}^{-3}$  and up to 8 eV. The  $\text{LaB}_6$  cathode is 35 cm across and electrons are accelerated through a 64.4 cm diameter, 66% transparent molybdenum anode. The  $\text{LaB}_6$  cathode can form hotter, denser plasmas with densities up to  $3 \times 10^{13} \text{ cm}^{-3}$  and temperatures up to 20 eV, though typical operation yields temperatures around 5 eV, and is also more robust to accidental atmospheric exposure. The  $\text{LaB}_6$  cathode is

heated to  $\approx 1700$  °C using a  $\approx 2$  kA heater. Both of these cathodes were used in the work presented here. An insertable, smaller (20 cm diameter) LaB<sub>6</sub> source also exists at the north end of the machine but is not used in this work.

The voltage applied across the cathode and anode is supplied by a 4.2 Farad capacitor bank switched by group of IGBTs. The discharge voltage is configurable up to 180V before triggering the over-voltage protection, though the capacitors are rated up to 200V. Current through the cathode can exceed 10 kA. Discharges can last as long as 70 ms, though a typical duration is around 15-20 ms. Discharge duration, power, and repetition rate are governed by the size of the capacitor bank and the charging power supply. The discharge repetition rate is configurable between 0.1 and 1 Hz.

### 2.2.2 Magnetic field

The LAPD has 13 independently-configurable magnet power supplies to shape the geometry of the axial magnetic field. Two of the supplies control the source region field, one controls the north end field where the smaller LaB<sub>6</sub> source resides, and the remaining 10 supplies control the field of the main plasma column. The source field can reach up to 8 kG and the main plasma column field up to 1.6 kG. A 1 kG field leads to an ion gyroradius of 2 mm at 1 eV, and a electron gyroradius of 50  $\mu$ m at 5 eV, so these plasmas are highly magnetized.

### 2.2.3 Gas fueling

There are two main ways of providing the neutral gas necessary for producing plasmas: the static fill system and gas puffing. The static fill system utilizes mass flow controllers to fill the chamber to the desired pressure, usually between  $10^{-5}$  and  $5 \times 10^{-4}$  Torr. The LAPD can be filled with a variety of (nonreactive) gasses, helium being the most common, followed by hydrogen and argon. The gas puff system utilizes piezo valves to puff gas into the chamber halfway between the cathode and anode. Gas puff duration and valve voltage can be set which influence the total amount of gas puffed and thus plasma density. Plasma breakdown using gas puffing is very reliable. Without

fueling the LAPD has a base pressure of  $5 \times 10^{-7}$  Torr.

A cartoon of the LAPD and relevant coordinate system can be seen in [TODO: fig.](#). Gratuitous LAPD shots can be seen in [TODO: appendix](#)

## 2.3 Data acquisition

Probes can sample virtually any point in this plasma through unique ball valves placed every  $\approx 32$  cm along the length of the device, enabling the collection of time series data with high spatial resolution. Four probe drives can simultaneously be used to move probes in the x-y plane. An x-y-z probe drive is also available for collecting volumetric data.

There are also 3 permanently attached probe drives mounted  $45^\circ$  up from the -x axis, on which, at the time of this writing, are mounted Langmuir probes. These drives have a limited motion compared to the standard x-y probe drives used during dataruns.

Primarily, probe data acquisition is handled through the main data acquisition system, simply referred to as the “DAQ”. The DAQ consists of SIS 3302 digitizers (theoretically 32 channels total) capable of sampling signals between  $\pm 2.5$  V at 100 MHz at 16 bits. Typically sample averages are taken (16 samples for my data) to reduce data transfer and file size. The DAQ is set up through a LabView-based control system.

This LabView system manages “dataruns” which are a series of discharges with a particular LAPD, DAQ, probe motion control, and general device configuration. This system also manages probe drive configuration. Probe motion can be lines or planes using this LabView system. Typically collect many shots per location to get good statistics. Can control other devices like oscilloscope

The machine state information system (MSI) Information about the discharge (current, voltage), auxiliary diagnostic signals (used to record interferometer) Also records gas information (puffing is not digitized, however) Uses a National Instruments PCIe-6346, 16 bits, 8 analog inputs, 500 kS/s Records state of magnets, calculated field Auxiliary python system to collate diagnostics from

multiple sources

## 2.4 Diagnostics

LAPD can field many different diagnostics and other equipment through the ball-valve ports as well as much larger box-shaped ports. Probe diagnostics typically go through an isolation amplifier before heading into the DAQ, along with attenuators so the signals fit the DAQ range

### 2.4.1 Langmuir probes: $I_{\text{sat}}$ , sweeps, triple probes

Pics of Langmuir probe Here is an IV curve of a Langmuir probe Sweeping along voltage gives you a “sweep” This is the equation for a swept curve This is a plot showing it  $I_{\text{sat}}$  is the portion with most negative signal; collects as many ions as possible Triple probe offsets  $V_f$  with  $I_{\text{sat}}$  giving you a third point, and from that you can get  $T_e$  Triple probe equation

### 2.4.2 Bdot probes

Magnetic flux probe Uses two loops on each axis, differentially amplified to remove electrostatic effects Each axis is calibrated using a Helmholtz coil and a spectrum analyzer (compensate for crosstalk and imperfect pointing of the coils) Bdot probe pic

### 2.4.3 The 288 GHz heterodyne interferometer

Rapidly sweeps through a bunch of frequencies and uses that to measure the density Very accurate Read through an oscilloscope, can interface with labview or python

#### **2.4.4 Thomson scattering**

Shoot a 532 nm laser into the plasma, 0.3J, polarized Collect spectrum on a camera, make sure to take dark frame Analyze by fitting a Gaussian to get temperature. Density depends on photon count – needs absolute calibration, otherwise not reliable

#### **2.4.5 Fast framing camera**

Phantom v7.3, can record at over 35k frames per second at 256x256. Monochrome, 14 bits Great for building an intuition on the structures at play inside the plasma Makes for some pretty pictures and videos

### **2.5 Instabilities in mirrors and the LAPD**

#### **2.5.1 Rotational interchange**

#### **2.5.2 Drift waves**

Pressure gradient in a slab Any resistivity leads to charge separation and instability growth Show diagram

#### **2.5.3 Interchange**

Pressure gradient aligned with curvature vector Showstopper for earlier mirror machines

### **2.6 Machine learning and neural networks**

Neural networks are a way of expressing a function Can represent any function given sufficient capacity (universal approximation theorem)

## **2.6.1 Fundamentals of neural networks**

Weights, nonlinearities, biases Train using gradient descent

## **2.6.2 Common architectures**

Dense: every input connects to every output  
CNNs: scan filter across input  
Attention blocks: model learns to pay attention to certain features

## CHAPTER 3

# Turbulence and transport in mirror geometries in the Large Plasma Device

In this chapter we study turbulence and cross-field particle transport in LAPD mirror configurations. Mirror machines are once again rising in prominence as a candidate for commercial fusion reactors with the advent of highly-funded commercial ventures and high-field high-temperature superconducting magnets [EAB23, FAE24], so development of a functional understanding of cross-field transport in mirrors is imperative. Using the LAPD, multiple mirror ratios from  $M = 1$  to  $M = 2.68$  and three mirror-cell lengths from  $L = 3.51\text{m}$  to  $L = 10.86\text{m}$  were examined. Langmuir and magnetic probes were used to measure profiles of density, temperature, potential, and magnetic field. The fluctuation-driven  $\tilde{E} \times B$  particle flux was calculated from these quantities. Two probe correlation techniques were used to infer wavenumbers and two-dimensional structure. Cross-field particle flux and density fluctuation power decreased with increased mirror ratio. Core density and temperatures remain similar with mirror ratio, but radial line-integrated density increased. The physical expansion of the plasma in the mirror cell by using a higher field in the source region may have led to reduced density fluctuation power through the increased gradient scale length. This increased scale length reduced the growth rate and saturation level of rotational interchange and drift-like instabilities. Despite the introduction of magnetic curvature, no evidence of mirror driven instabilities — interchange, velocity space, or otherwise — were observed. For curvature-induced interchange, many possible stabilization mechanisms were present, suppressing the visibility of the instability.

This chapter is largely a copy of my 2025 publication in the Journal of Plasma Physics titled "Turbulence and transport in mirror geometries in the Large Plasma Device" [tra], with some additions and small changes

### 3.1 Introduction

Historically, mirror research has prioritized the main issues with mirror confinement: stabilizing the interchange instability, stabilizing velocity-space (loss-cone-driven) instabilities, and minimizing axial electron heat losses. Nevertheless cross-field transport remains an important topic in magnetic-confinement fusion reactor development, in both linear and toroidal geometries. Insight into edge-relevant turbulence, and its coupling to interchange and other mirror-driven instabilities, performed in a basic plasma science device may be useful for a mirror-based reactor. Although not at fusion-relevant core temperatures or densities, the Large Plasma Device (LAPD) operates at conditions similar to the edge of fusion devices and can provide insight into the physical processes in that region. A characterization of edge fluctuations has been undertaken, with emphasis on interpreting these fluctuations within the context of mirror.

Non-classical cross-field particle transport is often caused by low-frequency, large-amplitude fluctuations. These fluctuations are the result of various instabilities. One such process is the "universal" drift instability, which appears in the presence of a density gradient and finite resistivity. Drift wave turbulence and the effect on transport has been extensively studied in the past [Hor99, TFM09]. In the presence of sufficiently high rotation or sheared flow, rotational interchange and the Kelvin-Helmholtz instabilities also contribute or couple to these fluctuations.

Various gradient-, rotation-, and shear-driven instabilities (and suppression of such) have been studied previously in the LAPD experimentally [SCR12, SCR13, Sch13] and in simulations using BOUT, a 3d fluid turbulence code, and an eigenvalue solver [PUC10]. The LAPD has a sufficiently high spontaneous rotation rate that rotation-driven instabilities may be excited without artificial drive. Simulations using BOUT++ [FCU13] have also suggested that a rapidly growing nonlinear

instability may dominate over all other linear instabilities.

Imposing a magnetic mirror configuration introduces magnetic curvature. The alignment of the curvature vector with a pressure gradient vector component causes the flute-like interchange instability if no stabilization mechanism is present. This interchange mode could couple to finite  $k_{\parallel}$  drift waves. The coupling of drift waves to curvature-induced interchange modes has been studied in toroidal devices such as TORPEX [PBD06, FLM06], where curvature was seen as the driving component for the unstable drift-interchange modes. Drift-like fluctuations have also been observed in the GAMMA-10 mirror [MII91, YMM10]. Flute-like modes and drift waves have been studied in other linear devices, such as Mirabelle [BGB05], where the appearance of flute-like modes or drift waves were controlled by varying the field and limiter diameter.

The rotational interchange and curvature interchange can both be flute-like modes. Rotational interchange (also called the “centrifugal instability”) is driven by the aligned centrifugal force and pressure gradient vectors, but curvature-driven interchange is instead driven by magnetic curvature and is typically referred to as simply the “flute” or “interchange” instability. Rotational interchange [Jas72] has been observed in the LAPD in the past [SCR12, Sch13], and the curvature-driven interchange instability has been observed in many other mirror machines [WV82, FWD83, Pos87].

Biassing or modifying the electrical connection of the plasma with the end wall has proven to be an important actuator in many mirror machines such as TMX-U [HBF84], GAMMA-10 [MII91], and GDT [BLZ03, BBS07, BBC10], and will be utilized on WHAM [EAB23]. Active biassing was not attempted in this study, but the intrinsic rotation and strong electrical connection to the source region may provide a useful analog for edge biassing in other mirror machines.

The LAPD exhibits a high degree of turbulence so it is difficult to identify the dispersion relation of the modes that are present. Nevertheless, the LAPD has good coverage of perpendicular spectra using correlation-plane techniques, and some measure of parallel spectra using the correlation between two axially-separated probes. A space-time spectral characterization of the many instabilities present in this low beta, moderate aspect ratio, gas-dynamic trap regime is attempted.

This goal of this study was to investigate the changes to turbulence and transport in LAPD mirror configurations. Of particular interest were the potential coupling of the interchange instability with drift waves or other modes, and the effect of the mirror geometry on cross-field particle flux. Presented is a characterization of the observed modes and the effect of introducing a mirror geometry. This paper is organized as follows. Sec. 3.2 discusses the configuration of the LAPD and the diagnostics used. Sec. 3.3 covers the changes seen when imposing a magnetic mirror configuration on profiles, particle flux, drift waves, turbulence, and magnetic fluctuations. Sec. 3.4 explores the changes in 2d (x-y plane) structure. Sec. 3.5 discusses the active and expected instabilities and reasons for their modification. Sec. 3.6 summarizes the study and discusses the requirements for a deeper investigation.

## 3.2 The experiment and device configuration

### 3.2.1 The Large Plasma Device (LAPD)

In this study, the plasma was formed using an emissive, 72 cm diameter barium-oxide (BaO) cathode [GPL16b] (mapped to 60 cm in a flat field) and a 72 cm diameter, 50% transparent molybdenum anode that accelerate electrons across a configurable 40 – 70V potential; voltages of 60 and 63V were used in this study. The source has since been upgraded to a lanthanum hexaboride (LaB6) cathode [QGP23b] that enables access to higher-density, higher-temperature regimes, but all the data in this study are from plasma formed by a BaO cathode.

The flexible magnetic geometry of the LAPD was used to construct a variety of magnetic mirror configurations. The discharge current, fill pressure, and other machine parameters were held constant. The typical plasma parameters observed in this study can be seen in table 3.2. Data in several mirror ratios and lengths were collected (see table 3.1) but emphasis is placed on the short cell because the highest mirror ratio possible ( $M = 2.68$ ) with a 500 Gauss midplane field could be accessed and probes were able to be placed outside of the mirror cell. An overview of the axial magnetic field for the the short mirror configurations and probe locations can be seen in fig. 3.1. 2-

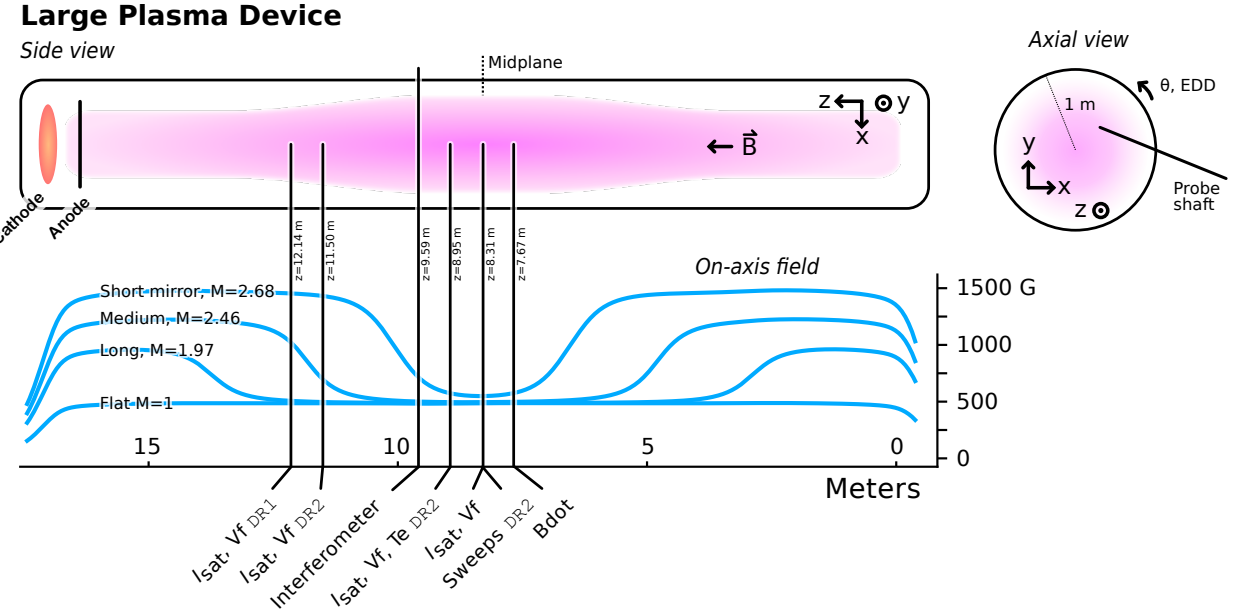


Figure 3.1: Cartoon of the Large Plasma Device and the coordinate system used. Only four of the eleven mirror configurations studied are plotted for clarity (mirrors of the same length have similar shapes and simply scale with mirror ratio). Diagnostic set varied by datarun; unlabeled diagnostics were used in both dataruns.

or 3-cell mirror configurations were also explored but are not examined in this study. All results presented below are from the short mirror cell configuration unless otherwise specified.

### 3.2.2 Diagnostics

All diagnostics were recorded with a effective sampling rate of 6.25 MHz (16-sample average at 100 MSPS) and a spatial resolution of 0.5 cm. When necessary, averaging over time is done in the approximate steady-state period of the plasma discharge (4.8 to 11.2 ms from the 1 kA trigger signal). Unless otherwise noted, all data presented will be from probes inside the mirror region ( $z \approx 7\text{ m}$ ). An example of a raw  $I_{\text{sat}}$  signal and processing steps can be seen in fig. 3.2. The raw signals are detrended by subtracting the mean across shots to obtain the fluctuations only. FFTs are then taken of these fluctuations for calculating power spectra and cross-correlated quantities.

Mirror length	Mirror ratios ( $M$ )
Flat	1
3.51 m (short)	1.47 1.90 2.30 2.68
7.03 m (medium)	1.49 1.98 2.46
10.86 m (long)	1.47 1.97 2.44

Table 3.1: Magnetic mirror lengths and ratios. The lengths are measured where the curvature changes sign and the ratio is the maximum divided by the minimum. Approximately 3.5m must be added to the length if the good-curvature region is included. In the case of small asymmetries, the field strengths were averaged before calculation of the mirror ratio.

Frequencies above 200 kHz are dominated by electronics and instrumentation noise and thus are also ignored. Fluctuation power profiles can then be constructed.

The data presented were collected in two phases. The first phase ("datarun"), DR1, collected Langmuir probe ( $I_{\text{sat}}$  and  $V_f$ ) and magnetic fluctuation ("Bdot") [EPC09] traces. 50 shots were taken at each position for every configuration. The second phase, DR2, was conducted with a similar set of diagnostics focused on temperature measurements (swept and triple probe) and 2d x-y structure. 15 shots were taken at each position, except for Langmuir sweeps with 64 shots. When appropriate, all data for each position were shot-averaged. " $I_{\text{sat}}$ " will be used interchangeably with "density" and be presented with units of density (assuming a flat  $T_e = 4.5$  eV profile).

### 3.3 Mirror-induced changes

#### 3.3.1 Profile modification

Because the field at the plasma source increases with  $M$ , the midplane plasma expands by a factor of  $\sqrt{M}$ . The physical locations of the peak fluctuation region –  $x_{PF}$  (maximum gradient) – and the cathode radius  $x_c$  can be seen in tab. 3.3. This expansion leads to broader plasma profiles and

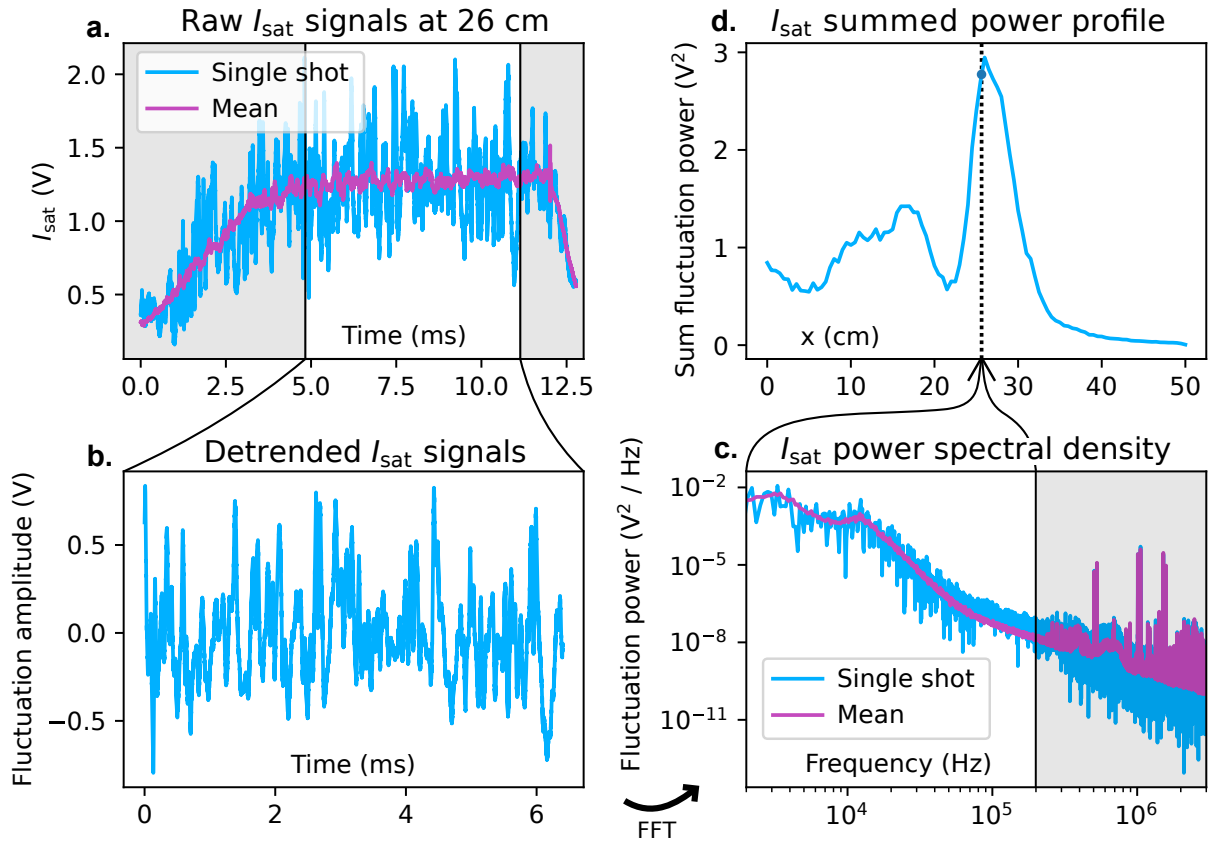


Figure 3.2: Raw data and basic processing steps for LAPD probe diagnostics as demonstrated by an  $I_{\text{sat}}$  trace from a DR1,  $M = 1$  mirror at 26 cm. Data are truncated from 4.8 to 11.2 ms (a) and detrended (b). Power spectral density is calculated (c), and a power profiles can be constructed (d). The shaded regions are excluded from this analysis.

Cathode radius (M=1)	$x_c$	30	cm
Machine radius	$R$	50	cm
Plasma length	$L$	$\sim 17$	m
Primary species		He-4 1+	
Electron-helium mass ratio		$1.37 \times 10^{-4}$	
Neutral pressure		$6 - 20 \times 10^{-5}$	Torr
Quantity		Core	$x = x_{\text{PF}}$
			Unit
Density	$n_e$	$1.25 \times 10^{12}$	$0.6 \times 10^{12}$ cm $^{-3}$
Ion temperature	$T_i$	$\sim 1$	— eV
Electron temperature	$T_e$	4	5 eV
Beta (total)	$\beta$	$9 \times 10^{-4}$	$6 \times 10^{-4}$
Midplane magnetic field	$B_{\text{mid}}$	500	— G
Plasma freq	$\Omega_{pe}$	10	7.1 GHz
Ion cyclotron freq	$\Omega_{ci}$	200	— kHz
Electron cyclotron freq	$\Omega_{ce}$	1.4	— GHz
Debye length	$\lambda_D$	0.013	0.021 mm
Electron skin depth	$\lambda_e$	30	43 mm
Ion gyroradius	$\lambda_{ci}$	5.8	— mm
Electron gyroradius	$\lambda_{ce}$	0.13	0.15 mm
Ion thermal velocity	$\bar{v}_i$	6.94	— km/s
Electron thermal velocity	$\bar{v}_e$	1190	1330 km/s
Sound speed	$c_s$	13.0	13.9 km/s
Alfvén speed	$v_a$	446 – 1140	–1620 km/s
Ion sound radius	$\rho_s$	65	69 mm
Ion-ion collision freq	$\nu_{ii}$	730	380 kHz
Electron-ion collision freq	$\nu_{ei}$	6.77	2.59 MHz
Electron collision freq	$\nu_{ee}$	9.57	3.66 MHz
Ion mean free path	$\lambda_{i,\text{mfp}}$	26	50 mm
Electron mean free path	$\lambda_{e,\text{mfp}}$	175	512 mm
Spitzer resistivity	$\eta$	192	$\mu\Omega$ m

Table 3.2: LAPD machine information and plasma parameters in the core and peak-fluctuation region ( $x = x_{\text{PF}}$ ) at the midplane in this study. Dashed quantities are assumed to be identical to core quantities.

Mirror ratio	1	1.47	1.90	2.30	2.68
Scale factor	1	1.21	1.38	1.52	1.64
$x_c$ (cm)	30	36	41	45	49
$x_{PF}$ (cm)	26	32	36	40	43

Table 3.3:  $x_c$  and  $x_{PF}$  locations for each mirror ratio when scaled by the expected magnetic expansion.

decreased core density but are similar in the core and at  $x_{PF}$  when magnetically-mapped to the cathode radius  $x_c$  as seen in fig. 3.4. Dips between the core ( $x/x_c = 0$ ) and the peak fluctuation region ( $x = x_{PF}$ ) are seen, but fluctuation power from this region ( $x/x_c = 0.5$  to 0.7) is not significant (fig. 3.8) so this region is not the focus of this study. The line-integrated density as measured by a 56 GHz heterodyne interferometer increases up to  $\sim 35\%$  from the M=1 case of  $\approx 8 \times 10^{13} \text{ cm}^{-2}$  (fig. 3.5) but does not increase past a mirror ratio of 2.3.

The error of on the  $I_{\text{sat}}$  profiles as represented by the standard deviation (scaled by the time-averaged profiles) can be seen in fig. 3.3. The error is relatively small and should not play a factor in our analysis – rarely are differences between quantities of the different mirror ratios that small.

Discharge power increases only slightly (3%) at higher mirror ratios suggesting negligible impact on density. Langmuir sweeps and triple probe measurements of  $T_e$  (DR2) show slightly (less than 25%) depressed core and slightly elevated edge  $T_e$  with increasing mirror ratio (fig. 3.6) but otherwise remains unaffected. The temperature affects  $I_{\text{sat}}$  measurements through the  $\sqrt{T_e}$  term so small changes are insignificant. The low temperatures indicate that the plasma is collisional given the length scales of the system (as seen in table 3.2) and isotropic. Plasma potential decreases across the plasma (fig. 3.7) when the mirror ratio exceeds 1.9. This drop in plasma potential may be caused by the grounding of the anode to the wall, which should begin at  $M = 1.93$  given the 72 cm anode and 100 cm vessel diameters. The reason for the local minimum in the M=2.68 is unknown. This potential profile creates a sheared  $\mathbf{E} \times \mathbf{B}$  velocity profile (fig. 3.7) limited to 500 m/s in the core and exceeding  $\sim 3$  km/s at the far edge. The flow does not exceed 4% of the sound speed

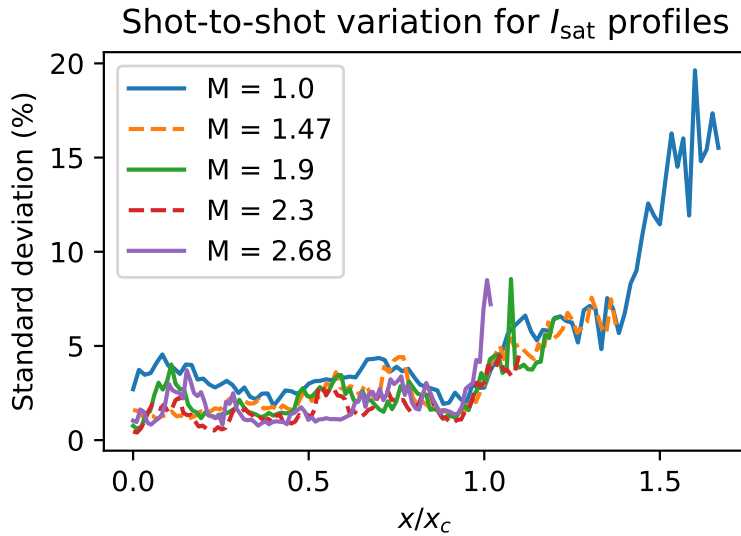


Figure 3.3: Shot-to-shot variation of  $I_{\text{sat}}$  profiles

(tab. 3.2) in the core or gradient ( $x = x_{PF}$ ) region. The mirror ratio does not appear to significantly alter azimuthal flow. The floating potential (Vf) profile also exhibits similar behavior to the plasma potential (fig. 3.7), but is modified by the presence of primary electrons.

### 3.3.2 Reduced particle flux

The density fluctuation power peaks at the steepest gradient region ( $x_{PF} = x/x_c \sim 0.88$ ) as expected as seen in fig. 3.8.  $x_{PF}$  occurs at nearly the same magnetically-mapped coordinate for each mirror ratio. These density fluctuations are a large driver of changes in the cross-field particle flux (eq. 3.1). Vf fluctuations also peak at the same location, but the total power across mirror ratios are similar and, relative to density fluctuations, much lower in the core. Core density fluctuations below 2 kHz are substantial in the core at lower mirror ratios, possibly caused by hollow profiles, nonuniform cathode emissivity, or probe perturbations, but are outside the scope of this study.

A spectral decomposition technique is used to calculate the time-averaged particle flux [Pow74]

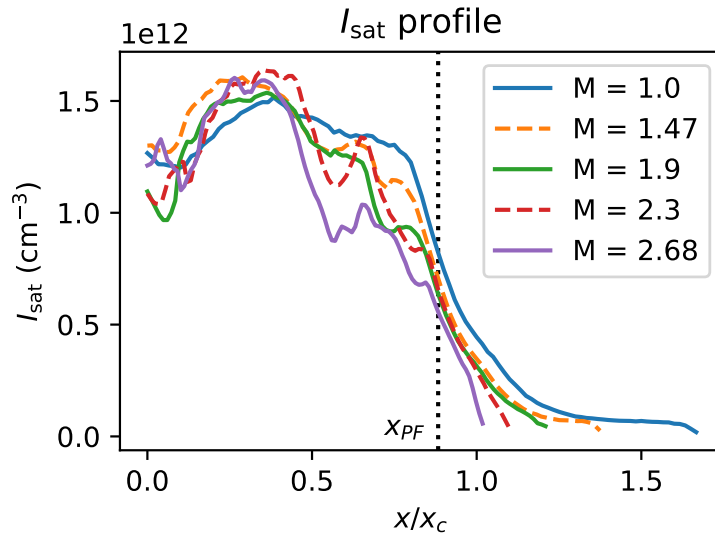


Figure 3.4: Midplane  $I_{\text{sat}}$  profile, shot-averaged and time-averaged from 4.8 to 11.2 ms (assumed of  $T_e = 4.5$  eV based on triple probe and Langmuir sweep measurements). Effective area was calibrated using a nearby interferometer. Profile shape remains similar in the core and gradient region when mapped to the cathode radius  $x_c$ . The dips in profiles at higher  $M$  below  $x = x_{\text{PF}}$  are of unknown origin and are not the focus of this study. Shot-to-shot variation is less than 5% for  $x \leq 0.95x_c$  and less than 9% for  $x \leq 1.4x_c$  for all cases.

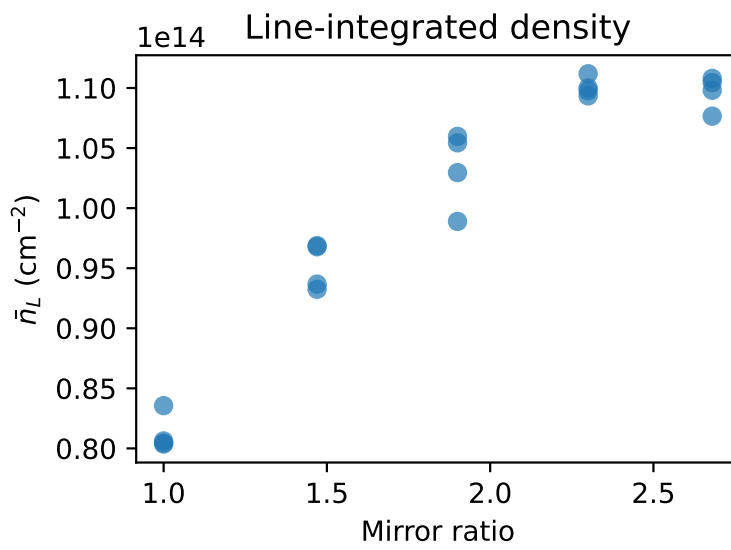


Figure 3.5: Line-integrated density as measured by a 56 GHz heterodyne interferometer as a function of mirror ratio, taken from four discharges for each mirror configuration. Density increases up to a mirror ratio of 2.3 where it appears to level off. The interferometer is located in the mirror cell bad-curvature region at 9.59m, 1.3m closer to the cathode from the midplane.

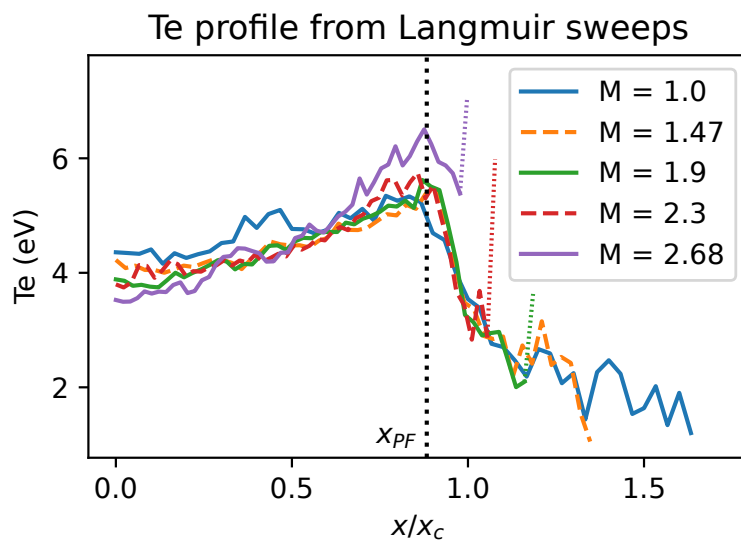


Figure 3.6:  $T_e$  from Langmuir sweeps (DR2) at the midplane. Triple probe results are nearly identical. The increased temperatures directly at the plasma edge, indicated by dotted portions of the curves, are likely artifacts caused by sheath expansion in lower densities. Changes in mirror ratio lead to at most 25% change in  $T_e$ . The plasma is collisional and isotropic.

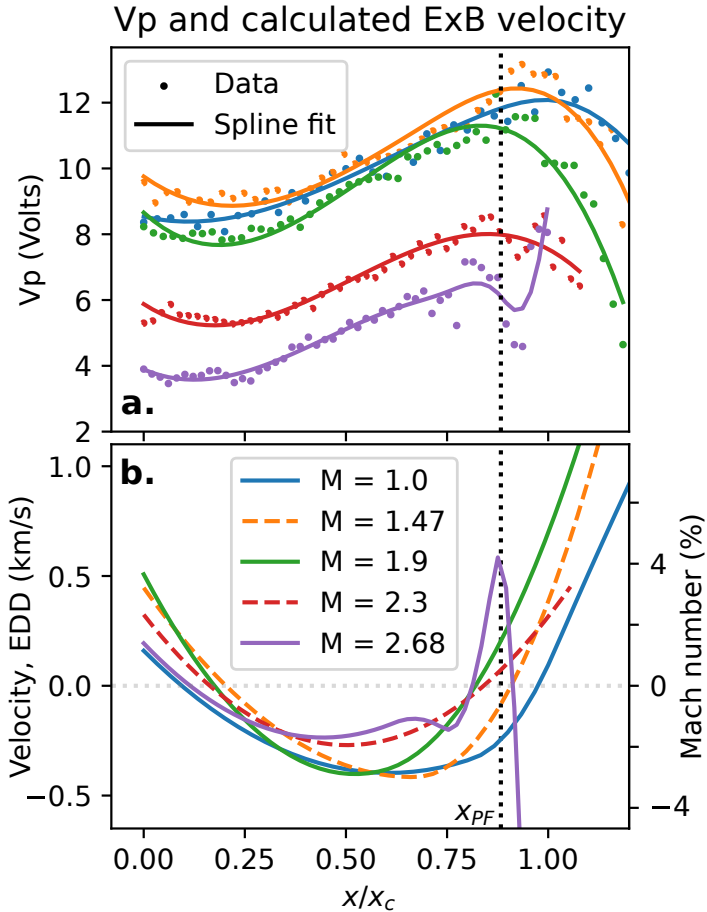


Figure 3.7: Plasma potential (a) and derived  $\mathbf{E} \times \mathbf{B}$  velocity profiles (b) from Langmuir sweeps at the midplane.  $x/x_c > 1.2$  has been excluded from the graph for greater clarity in the core and gradient region. The electric field was calculated by taking the gradient of the spline-smoothed plasma potential profile. The Mach number (in percent) is calculated using the approximate sound speed evaluated at  $x = x_{PF}$  (tab. 3.2). The overall structure of the flows does not appreciably change when mirror ratio is varied.

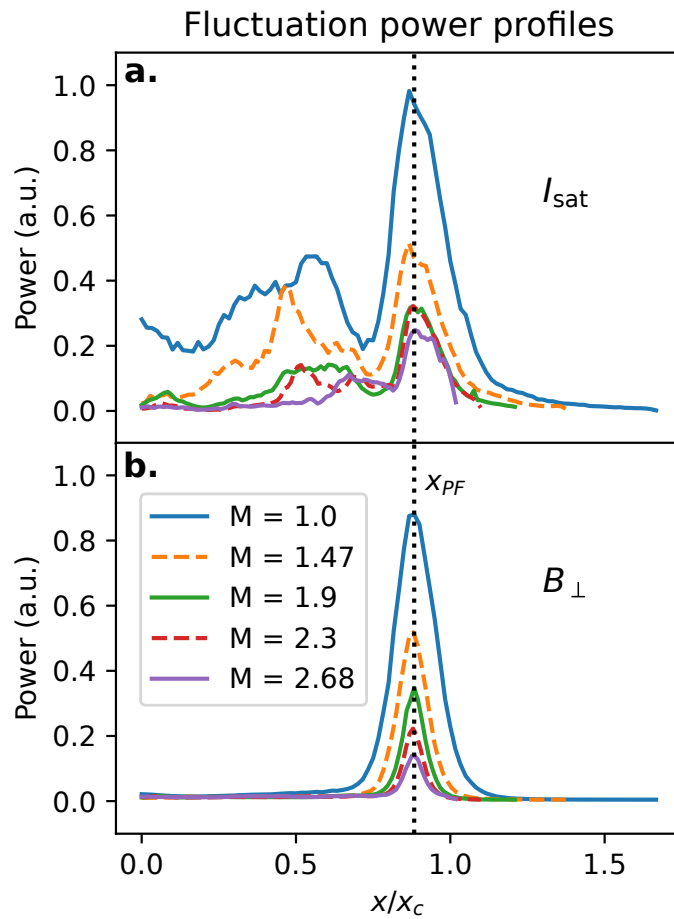


Figure 3.8:  $I_{\text{sat}}$  (a) and  $B_{\perp}$  (b) fluctuation power profiles for signals 2 kHz and up at  $z=8.3\text{m}$  (midplane) and  $z=7.7\text{m}$ , respectively. The lower frequency components in  $I_{\text{sat}}$  are associated with bulk profile evolution, dominate the core region, and are not the focus of this study.

as seen in fig. 3.9:

$$\Gamma_{\tilde{E} \times B} = \langle \tilde{n} \tilde{v} \rangle = \frac{2}{B} \int_0^{\infty} k(\omega) \gamma_{n\phi}(\omega) \sin(\alpha_{n\phi}) \sqrt{P_{nn}(\omega) P_{\phi\phi}(\omega)} d\omega \quad (3.1)$$

where  $k$  is the azimuthal wavenumber,  $\gamma$  is the coherency,  $\alpha$  is the cross-phase, and  $P$  the power spectrum. This method is more robust than the naive time-integration of  $n(t) \tilde{E}(t)$  because it accounts for the coherency of the density-potential fluctuations. This representation also enables inspection of each contributing term in the event of surprising or problematic results. A plot of the  $I_{\text{sat}}$ -Vf phase can be seen in fig. 3.10. The flattened particle flux in the core is likely caused by primary electrons emitted by the cathode. These electrons have long mean free paths (greater than a few meters) and sample fluctuations along the length of the machine, mixing the phases of these fluctuations. Since floating potential is set by the hotter electron population, the measured Vf fluctuations are no longer related to the local plasma potential fluctuations of a wave by bulk  $T_e$  [CM09]. These primary electrons have a significant effect in the core within the region mapped to the cathode  $x \lesssim x_c$ .  $I_{\text{sat}}$  fluctuations are not affected.

Azimuthal wave number is measured by two Vf probe tips 0.5 cm apart. This wavenumber estimation technique yields good agreement with correlation plane measurements (fig. 3.31). Note that  $\tilde{E}$  is not directly measured – it is instead calculated through the  $k(\omega) \sqrt{P_{\phi\phi}(\omega)}$  terms. The  $\tilde{E} \times B$  particle flux clearly decreases with mirror ratio; most of this decrease is attributed to the decrease in density fluctuation power. The particle flux for each mirror ratio was normalized to the  $M = 1$  case via the plasma circumference to compensate for the increased plasma surface area at the same magnetically-mapped coordinate  $x/x_c$ . This particle flux is on the order of Bohm diffusion  $D_B = \frac{1}{16} \frac{T_e}{B} \approx 6.25 \text{ m}^2 \text{s}^{-1}$  as observed in other transport studies [MCT07].

$T_e$  profiles and fluctuations may affect particle fluxes but measurements of both were not taken in the same datarun; nevertheless, a quantification of the effect of  $T_e$  on particle flux is attempted.  $T_e$  fluctuations affect  $I_{\text{sat}}$ -based density measurements through the  $T_e^{-1/2}$  term, and triple probe and Langmuir sweep  $T_e$  measurements suggest that temperature gradients have a negligible impact. A naive incorporation of temperature fluctuation data from DR2 into particle fluxes from DR1 suggest that cross-field particle flux may be underestimated by up to 50% via the  $I_{\text{sat}}$  temperature term, but

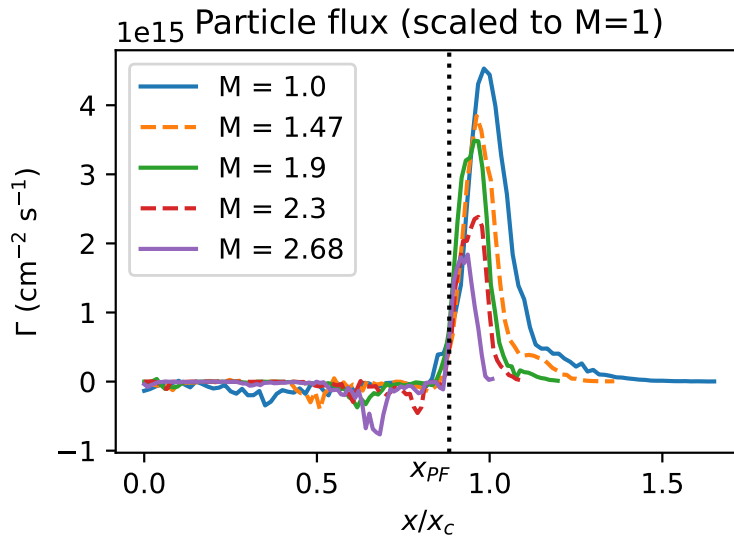


Figure 3.9: Cross-field,  $\tilde{E} \times B$  fluctuation-based particle flux (calculated using eq. 3.1) with respect to mirror ratio. A monotonic decrease in particle flux is observed with increasing mirror ratio at the midplane. Particle flux is normalized by plasma circumference to the  $M = 1$  case to account for the geometry-induced decrease in particle flux caused by a larger-diameter plasma.

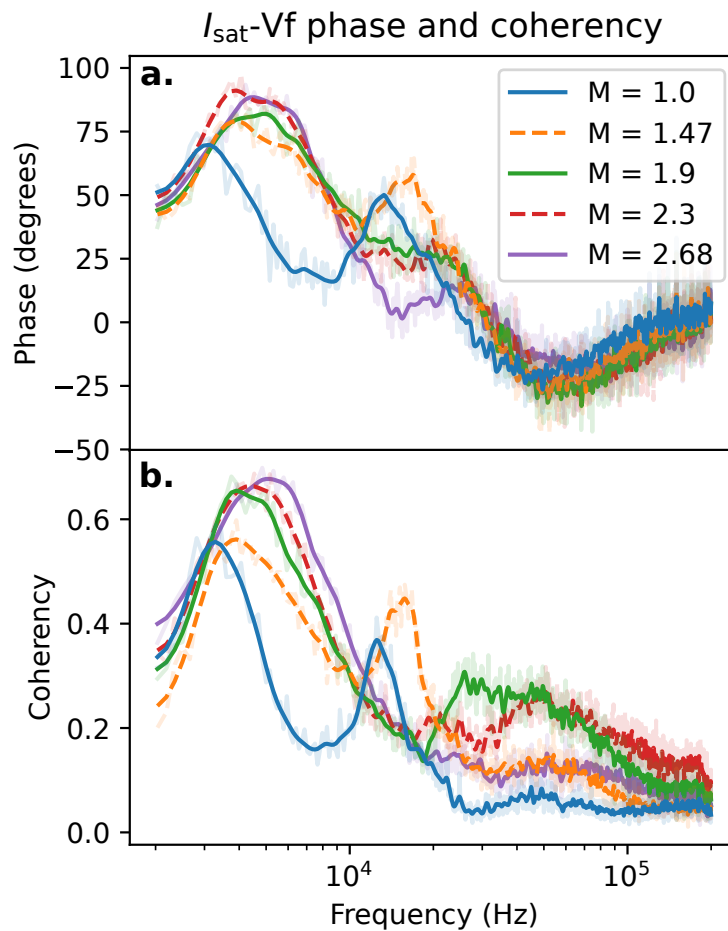


Figure 3.10: Phase (a) and coherency (b) of  $I_{\text{sat}}$  current and Vf near  $x_{PF}$  at the midplane, smoothed. Positive phase means  $I_{\text{sat}}$  leads Vf. Peaks in coherency occur between 3-5 kHz and at the drift-Alvén wave peaks between 12 and 25 kHz. These coherency peaks tend to have larger phase shifts than other nearby frequencies.

the trend and relative fluxes across mirror ratios remain unchanged. Such a naive incorporation should be treated with suspicion because of the sensitive nature of the flux with respect to the gradient and the differences in profiles between DR1 and DR2. These difference in profiles made be caused by cathode condition, deposits on the anode, or a different gas mix and are difficult to account for.

### 3.3.3 Compensating for the Te profile

Electron temperature (Te) compensation for the  $I_{\text{sat}}$  measurement can be done in several ways. One way is to account for the average temperature (i.e., steady state) when calculating the density from  $I_{\text{sat}}$ . Te can be gathered from triple probe or swept measurements. Triple probe measurements are generally less reliable than swept probe measurements. The difference between swept and triple probe Te measurements can be seen in fig. 3.11. The two techniques have roughly good agreement, though the triple probe appears to slightly underestimate the temperature. The spikes in the edge are likely from sheath expansion of the probe in the swept measurements (see fig. 3.6).

Te fluctuations can affect  $I_{\text{sat}}$  fluctuation measurements through the  $\sqrt{\text{Te}}$  term. In this case, Te measurements are difficult to compensate for in DR1 because of the changes in profiles between DR1 and DR2, so the Te fluctuations were included by finding the ratio in DR2 of  $I_{\text{sat}}$  fluctuations before and after including these Te fluctuations. This ratio was then applied to DR1. The issue of mismatched profiles still persists but this method allows for changes in fluctuation power between the two datarun sets. In general,  $\tilde{\text{Te}}/\text{Te}$  fluctuations are at most than 30% (near the edge), and much lower in the core seen in fig. 3.12.

This Te compensation becomes particularly important when calculating the  $I_{\text{sat}}$  profile gradients which is needed when calculating the diffusivity. A calculation of the diffusivity scaled to the Bohm diffusivity  $D_B = \frac{1}{16} \frac{T}{eB}$  can be seen in fig. 3.13. This calculation uses the particle flux calculated earlier (in the paper) and tanh fit on the density profile for a density smooth gradient. In general, mirror ratios higher than two have a lower diffusivity. When the particle flux is compensated for

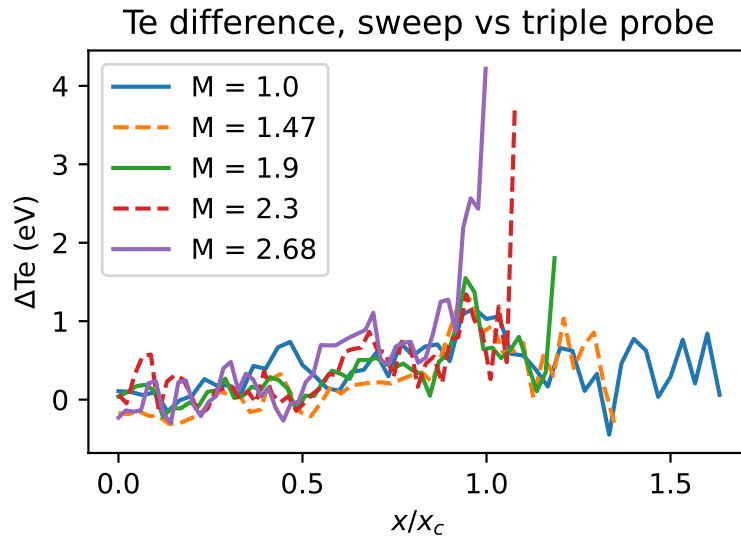


Figure 3.11: Difference between swept and triple probe temperature measurements. The triple probe appears to slightly underestimate the temperature and temperature gradient.

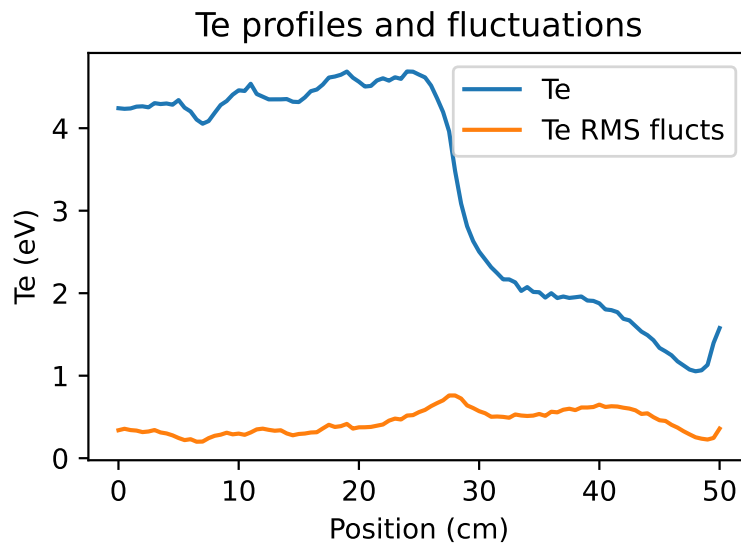


Figure 3.12:  $Te$  and  $Te$  fluctuation profiles from the triple probe. RMS electron temperature fluctuations are not particularly large.

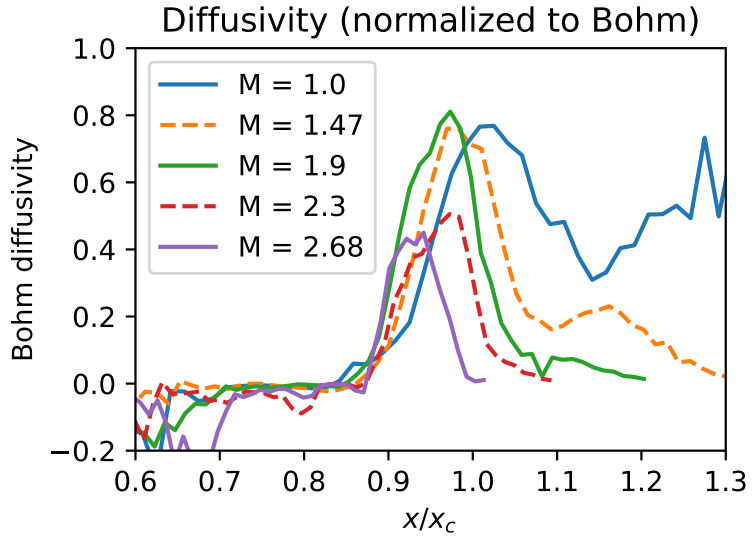


Figure 3.13: Diffusivity relative to  $D_B$  using a tanh fit for the density profile and the particle flux measurement assuming a constant  $T_e$  of 4.5 eV across the profile.

$T_e$  fluctuations, the temperature profile used in for the Bohm diffusion coefficient, and the density profile is smoothed convoluting a  $\sigma = 2$  cm gaussian, the diffusion coefficient relative to  $D_B$  are roughly 2.5 times greater, seen in fig. 3.14. The trend, however, remains relatively the same: higher mirror ratios tend to have a lower diffusivity. The impact of different profile smoothing methods on the density gradient can be seen in fig. 3.15.

### 3.3.4 Drift waves

The  $I_{\text{sat}}$  fluctuation power spectra in the region of peak power  $x \sim x_{\text{PF}}$ , also where the density gradient is strongest, can be seen in fig. 3.16. Notably, the fluctuation peaks shift to higher frequencies and decrease in total fluctuation power. The shift in frequency may be the Doppler shift caused by the change  $\mathbf{E} \times \mathbf{B}$  plasma rotation seen in fig. 3.7 at the location  $x/x_c \approx x_{\text{PF}}$ . The shift in frequency is somewhat smaller than what would be expected from the field line-averaged increase in Alfvén speed at the longest possible wavelength. The phase angle of  $I_{\text{sat}}$  and  $V_f$  provides insight

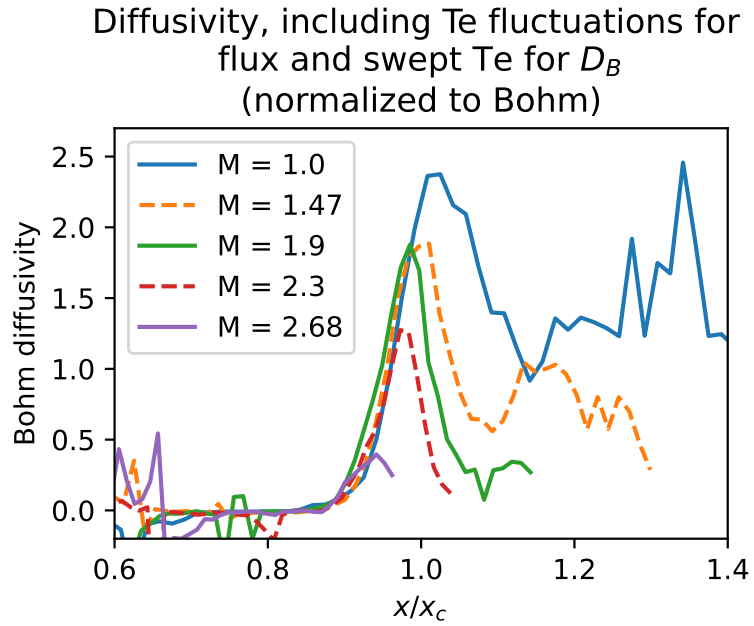


Figure 3.14: Diffusivity with Te compensation relative to  $D_B$ . The particle flux is compensated for Te fluctuations, and the swept-probe temperature profile is used for Te. The diffusivity is around 2.5 times higher than without compensation, but the trend remains similar.

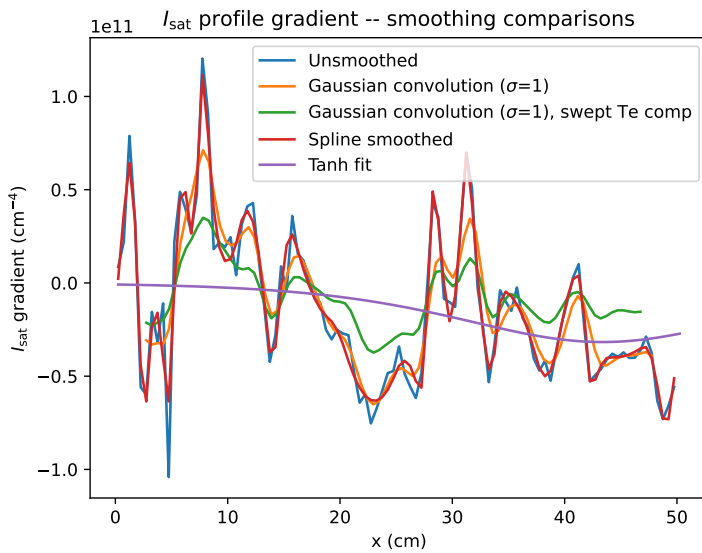


Figure 3.15:  $I_{\text{sat}}$  gradients under varying profile smoothing methods

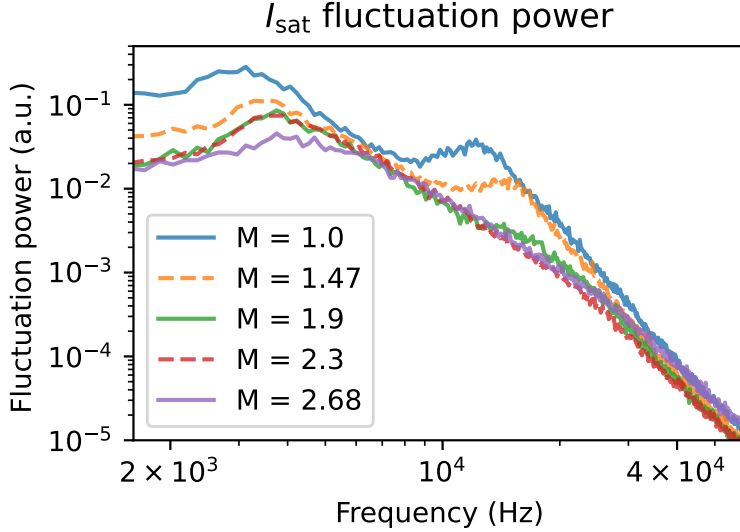


Figure 3.16:  $I_{\text{sat}}$  (density) fluctuation power averaged over a 1 cm region around  $x_{\text{PF}}$  at the midplane. The fluctuation power is largely featureless below 2 kHz and beyond 40 kHz aside from electronics noise.

into the nature of the driving instability. Including a nonzero resistivity  $\eta$  in the drift wave leads to a small phase shift  $\delta$  between density and potential. This phase shift  $\delta$  in a collisional plasmas is on the order of  $\delta \approx \omega v_e / k_{\parallel}^2 \bar{v}_e^2$  [Hor99]. Estimating this quantity using measured and typical values ( $k_{\parallel} = 0.18$  rad/m,  $\bar{v}_e = 1300$  km/s,  $v_e = 3.7$  MHz,  $\omega = 12$  kHz) yields a substantial phase shift of  $\delta \approx 46^\circ$ , which roughly agrees with the phase shifts in fig. 3.10, though the implied increased phase shift at higher frequencies does not agree with measurements. As seen in fig. 3.10, the phase difference between  $I_{\text{sat}}$  and Vf fluctuations are larger below 10 kHz, implying the presence of additional modes beyond or significant modification of resistive drift wave fluctuations. The phase difference between two Vf probes, 3.83 m apart, was used to calculate the parallel wavelength  $\frac{2\pi}{\lambda} = k_{\parallel} = \phi_{Vf1, Vf2} / \Delta z$  assuming the wavelengths are greater than 7.66 m. The two probes mapped to the same field line only in the  $M = 1$  configuration, so parallel wavenumbers are available only for the flat case. Parallel wavenumbers are theoretically calculable from 2d correlation planes but the coherency dropped dramatically when a mirror geometry was introduced. A 34 m wavelength mode likely contributes to

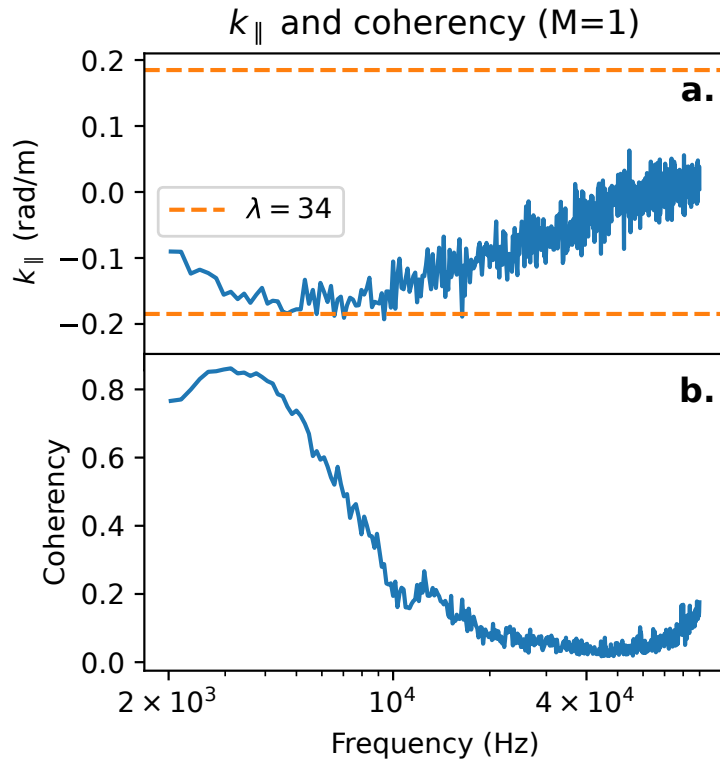


Figure 3.17:  $k_{\parallel}$  (a) and coherency  $\gamma$  (b) as a function of frequency. Only results from the  $M = 1$  case are available, but it is clear that there are long ( $\gtrsim 34$ m) wavelength modes at 3 and 12 kHz. The probes used for calculating  $k_{\parallel}$  were located at the midplane ( $z=8.31$ ) and  $z=12.14$  m, 3.83 m apart.

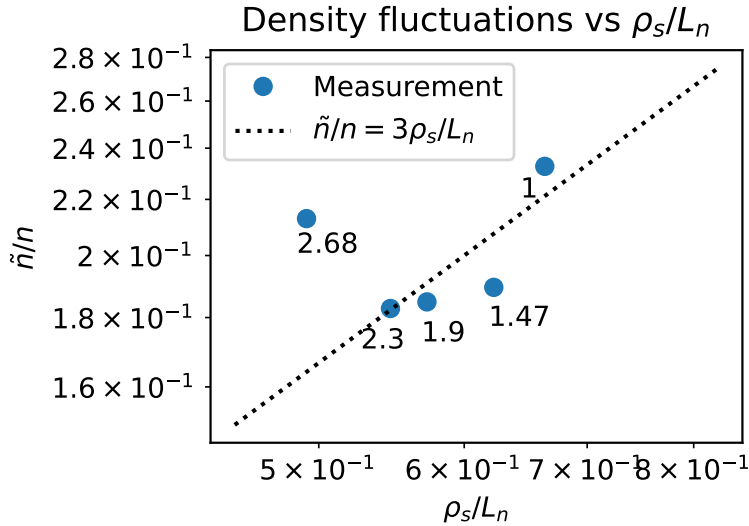


Figure 3.18: Normalized density fluctuations vs  $\rho_s/L_n$ . The measured values fall close to the  $\tilde{n}/n = 3\rho_s/L_n$  line which is consistent with theory.

the measured  $k_{\parallel}$  from 3 to  $\gtrsim 10$  kHz (fig 3.17). Drift waves are long-wavelength modes so coherent density and potential fluctuations along the flux tube are expected. The coherency is a measure of similarity of the spectral content of two signals, in this case Vf probes 1 and 2. The coherency is defined as  $\gamma = \frac{|\langle P_{1,2} \rangle|}{\langle |P_{1,1}|^2 \rangle \langle |P_{2,2}|^2 \rangle}$  where  $P_{x,y}$  is the cross-spectrum between signals  $x$  and  $y$  and the angle brackets  $\langle \rangle$  denote the mean over shots. The coherency between the two Vf probes drops off with increasing frequency, with a slight bump at around 12 kHz. There are several candidates for the driving mechanism of the 3-5 kHz mode, but the 12 kHz mode is most likely a drift-Alfvén wave.

Drift wave theory[Lie85] suggests that the normalized density fluctuation level  $\tilde{n}/n$  should fall near 3-10  $\rho_s/L_n$ . A plot of this relation using experimental data can be seen in fig. 3.18. However, comparison of  $\tilde{n}/n$  with  $1/(k_y L_n)$  show that the normalized density fluctuations are about an order of magnitude too small for the  $1/(k_y L_n)$  observed which is unexpected and this conflict has not been able to be resolved in this study.

Another issue with this drift-wave interpretation of results is that the electron thermal diffusion along the field line is too high. The plasma must be collisional enough that thermal equilibrium is

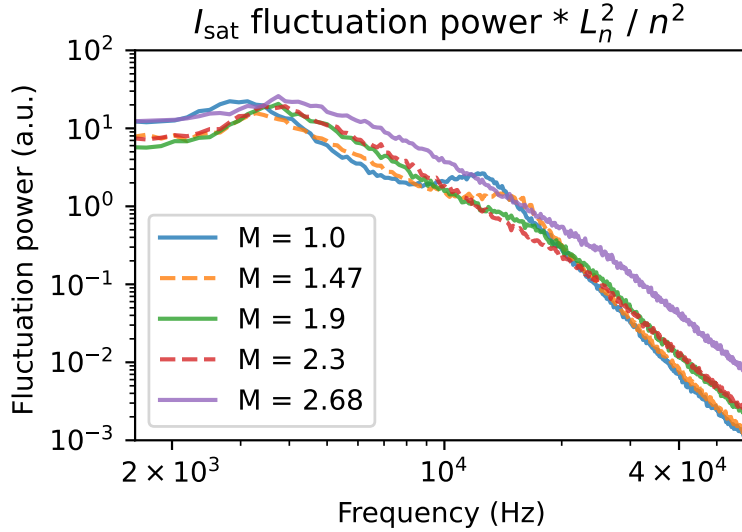


Figure 3.19:  $I_{\text{sat}}$  fluctuation power when scaled by the square of the gradient scale length and the squared density. We expect this value to be constant (assuming the same  $k_{\perp}$ ).

guaranteed (i.e., the temperature is Maxwellian) , but if the collision rate is too high then thermal gradients can develop along the field line[Gol95]. This condition on thermal diffusivity condition for the drift wave  $\omega$  and  $k_z$  is  $\omega \ll k_z^2 v_{e,th}^2 / v_{ei}$ . Plugging in values from the experiments yields frequencies at least 5 times greater than mandated by the diffusivity condition and the condition is violated. This condition violation may be responsible for the odd phase shifts seen between the density and potential fluctuations.

In saturated drift wave turbulence, the normalized density fluctuation amplitude is expected to scale with the gradient scale length  $L_n$ , so the fluctuation power then scales with  $L_n^2$ . A plot of this can be seen in fig. 3.19. This assumes the same  $k_y$ , but as mentioned earlier, that scaling and the relationship in general is not consistent with theoretical predictions for saturated drift wave turbulence.

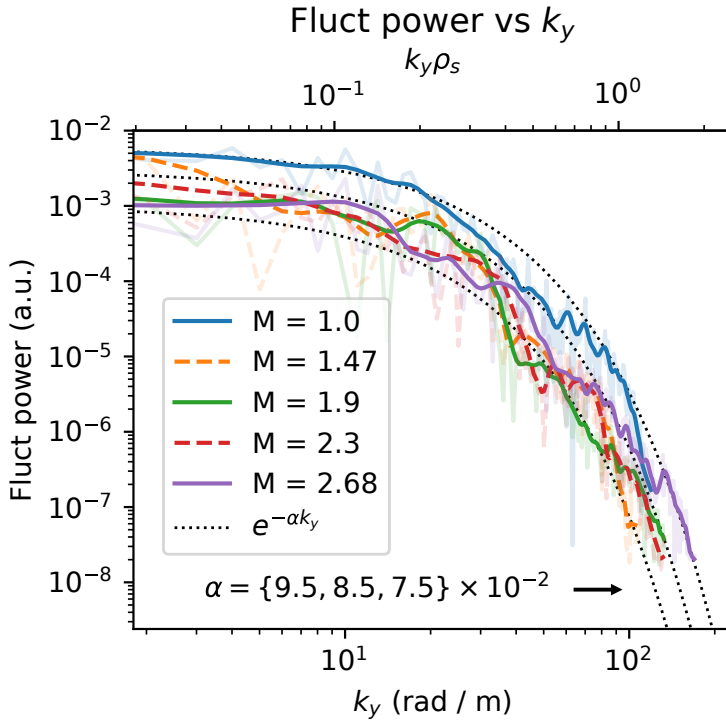


Figure 3.20: Fluctuation power summed for each  $k_y$  for frequencies up to 100 kHz, smoothed. The contribution to fluctuation power is negligible past 100 kHz. The fluctuation power decreases substantially when a mirror configuration is introduced, but no trend is seen otherwise and the  $k_y$  spectra remain exponential. Note the logarithmic scale.

### 3.3.5 Turbulence modification

The wavenumber-power relation in fig. 3.20 shows decreased fluctuation power when a mirror configuration is introduced. However, there is no discernible trend when the mirror ratio is increased further. The exponential nature of the curve also remains unchanged. The greatest decrease in fluctuation power occurred in low and high  $k_y$ 's, around 10 and 70 rad/m. The shape of the power- $k_y$  curves follow an exponential distribution, and is inconsistent with a 2d drift-wave turbulent cascade (Wakatani Hasegawa  $k^{-3}$ ) [WH84]. The steep dropoff in fluctuation power with  $k_y$  suggests that higher-wavenumber fluctuations do not have a significant effect on transport.

Previous simulations in a flat field [Fri13] predicted frequency and wavenumber spectra that can be fit with many power laws or exponentials, but the data presented here (figs. 3.16, 3.21, 3.20) appear to follow an exponential relationship within measurement variation.

Turbulence measurements can be directly compared to theoretical predictions and other devices, summarized by Liewer [Lie85]. For saturated drift wave turbulence, one expects the normalized fluctuation level  $\tilde{n}/n \sim 1/\langle k_{\perp} \rangle L_n$ , where  $k_{\perp}$  is some typical wavenumber. The power-weighted  $k_y$  (calculated from fig. 3.20) was approximately 15 rad/m, which is an order of magnitude too small to satisfy this relationship.  $\tilde{n}/n$  scaling with  $\rho_s/L_n$ , however, is roughly consistent with drift wave turbulence level saturation: the latter is  $\approx 3$  times larger. These comparisons suggest that the large, low frequency fluctuations ( $\sim 3$  kHz, which had even smaller  $k_y$ ) may have a drift wave turbulence component but are dominantly driven by other instabilities. No trend is seen in  $\rho_s/L_n$  and  $1/k_y L_n$  when mirror ratio was varied.

Core fluctuations appear to decrease dramatically as seen in the  $I_{\text{sat}}$  fluctuation power (fig. 3.8). The  $I_{\text{sat}}$  decorrelation time increases from  $\sim 0.7$  ms for  $M = 1$  to  $\sim 2.5$  ms for  $M = 2.68$ . At  $x = x_{PF}$ , decorrelation times for all mirror ratios remained at 0.2 ms.

### 3.3.6 Magnetic fluctuations

The perpendicular magnetic fluctuation ( $B_{\perp}$ ) component of the drift-Alfvén wave can be seen in fig. 3.21. These  $B_{\perp}$  fluctuations are spatially and spectrally coincident with the electrostatic fluctuations (fig. 3.16). Drift-Alfvén waves have been studied in the LAPD in the past [MM97, VG06]; strong coupling is observed for  $\beta_e > m_e/m_i$  which is satisfied in this study. The Alfvén speed  $\omega/k_{\parallel} = v_A = B/\sqrt{4\pi n M}$  (given  $\omega \ll \Omega_{ci}$ ) when averaged over the entire column ranges from  $\sim 450$  to  $\sim 1600$  km/s. A  $k_{\parallel}$  corresponding to a wavelength  $\lambda = 34$ m roughly falls within the bound established by the kinetic and inertial Alfvén wave dispersion relations at the frequency peaks observed at  $x \sim x_{PF}$  seen in fig. 3.21. The lengthening of field lines caused by curvature accounts for at most 10% of the change in frequency.

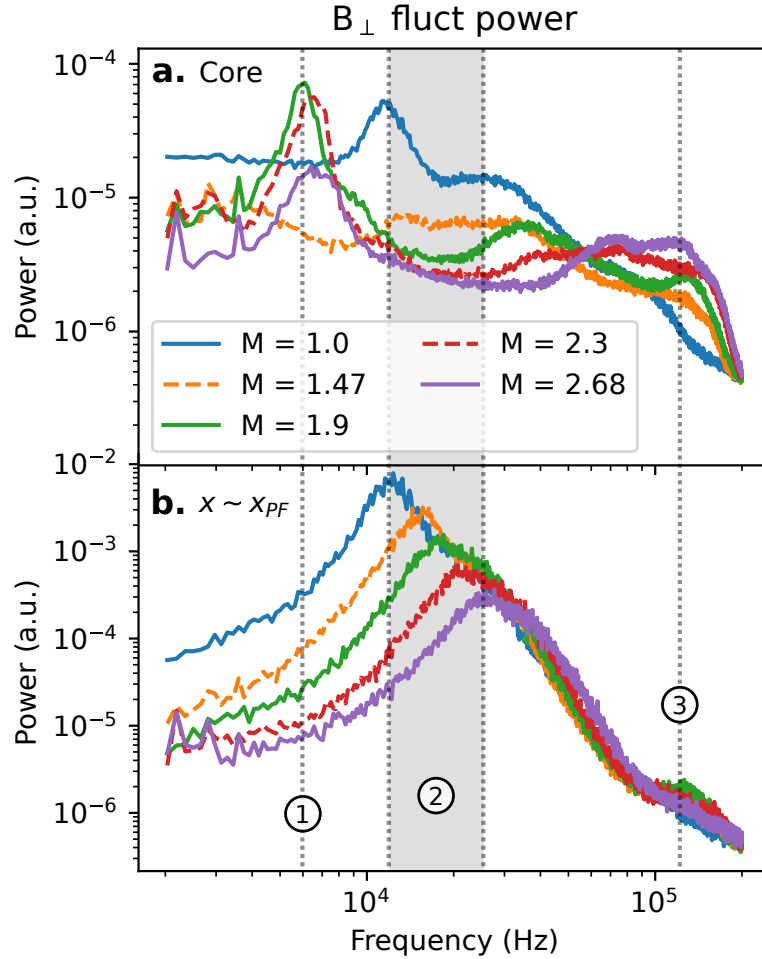


Figure 3.21:  $B_{\perp}$  fluctuation power averaged at the core from 0 to 3 cm (a) and around the peak fluctuation point ( $x \sim x_{PF}$ ) (b). Fluctuation power decreases across the board with mirror ratio except for core frequencies close to  $\Omega_{ci}$ . Peaks around 10 – 30 kHz at  $x_{PF}$  are consistent (region 2) with drift-Alfvén waves and the near-cyclotron frequency features in the core may be resonating Alfvén waves created by the magnetic mirror. Frequencies below 2 kHz and dominated by instrumentation noise and thus excluded.

The spatial extent of the  $B_{\perp}$  features identified in fig. 3.21 are plotted in fig. 3.22. Feature 1 at  $\approx 6$  kHz shows increased fluctuation amplitudes at  $x = 0$  for mirror ratios 1.9 and above, but for  $M = 1$  and  $M = 1.47$  there is no increase in fluctuation power. A similar feature, but at a much smaller level, is observed in  $I_{\text{sat}}$  fluctuation power in the core as well. This core feature may be caused by the hole in the core seen in the  $I_{\text{sat}}$  profile (fig. 3.4) driving low-amplitude waves or instabilities. Feature 2 in fig. 3.22 is the magnetic component of the drift-Alfvén wave. The fluctuation power peaks at the gradient region and corresponds with the peak in density fluctuations (fig. 3.8).

Feature 3 is particularly interesting because this the only fluctuating quantity to *increase* with mirror ratio, seen in fig. 3.23. This feature may be broad evanescent Alfvénic fluctuations from the plasma source. These fluctuations have been observed in the LAPD in the source region alongside an Alfvén wave maser [MMC05]. Note that the Alfvén maser cannot enter the mirror cell at mirror ratios greater than 1.75 because the Alfvén maser resonates at  $0.57 f_{ci}$  but the midplane is always at or near 500G.

The sub-2 kHz modes in  $B_{\perp}$  and its harmonics are nearly constant in power across the entire plasma; these features are likely perturbations from the magnet power supplies and thus ignored. The lack of radial, azimuthal, and axial structure in these magnetic signals below 2 kHz and narrow bandwidth indicate a non-plasma origin. Significant radial and azimuthal structure in  $B_{\perp}$  fluctuation power starts to appear in frequencies larger than 4 kHz.

The drift-Alfvénic nature of the 12 kHz Bdot feature is confirmed by changing the flat field from 500G to 400G: the feature shifts down in frequency from 12 to 10 kHz seen in fig. 3.24. From the drift wave and Alfvén wave dispersion relations the frequency is expected to be  $400G / 500G = 0.8$  of the original, which is approximately what is observed. The  $k_y$  of the drift-Alfvén wave also has an effect and may be responsible for a  $10 \text{ kHz} / 12 \text{ kHz} = 0.83$  factor instead.

There may be some sort of resonator made by the mirror cell and its interaction with Alfvén waves. In fig. 3.25, the behavior of the  $B_{\perp}$  spectrum in the core changes dramatically between 1 and 10 kHz in the short mirror when compared with the medium and longer mirrors. It's unlikely

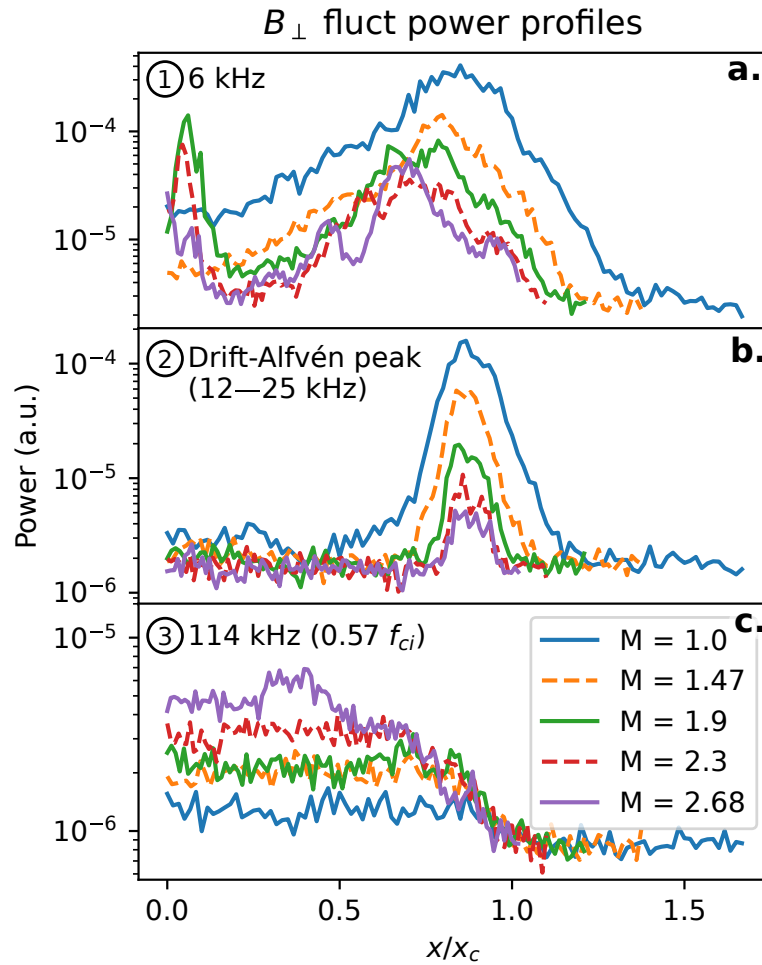


Figure 3.22:  $B_{\perp}$  fluctuation power profiles for the three regions shown in fig. 3.21: region 1 (6 kHz) (a), region 2 — where frequencies are taken from the peaks of the drift-Alfvén waves for each mirror ratio (b), and region 3 (114 kHz) (c).

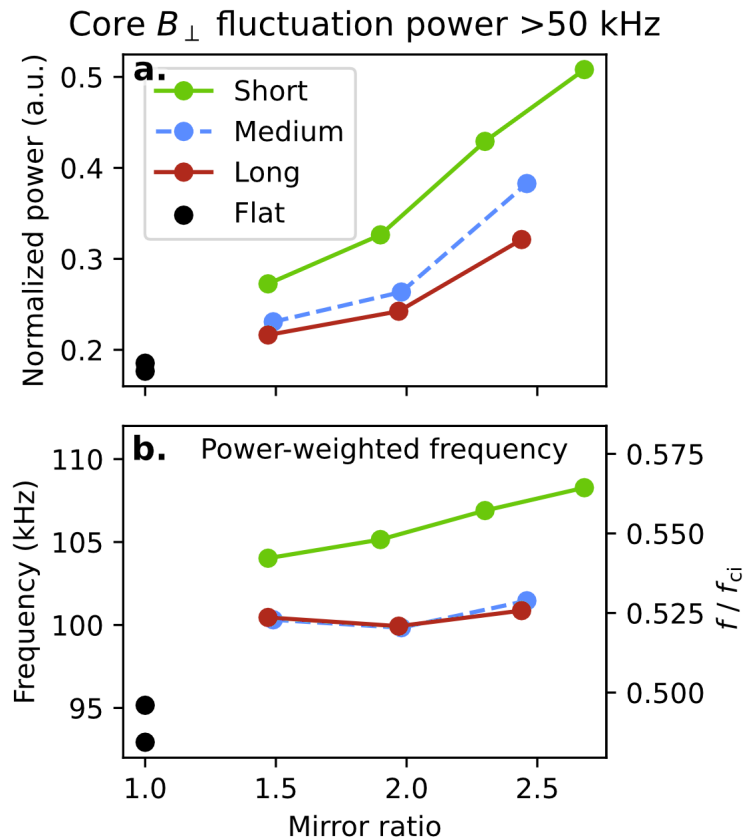


Figure 3.23: Summed fluctuation power of  $B_{\perp}$  in the core ( $x/x_c \leq 0.3$ ) as a function of mirror length and ratio. Top (a): the fluctuation power is normalized by the sum of the full-spectrum summed power. Bottom(b): the frequency of the power distribution > 50 kHz weighted by the fluctuation power.

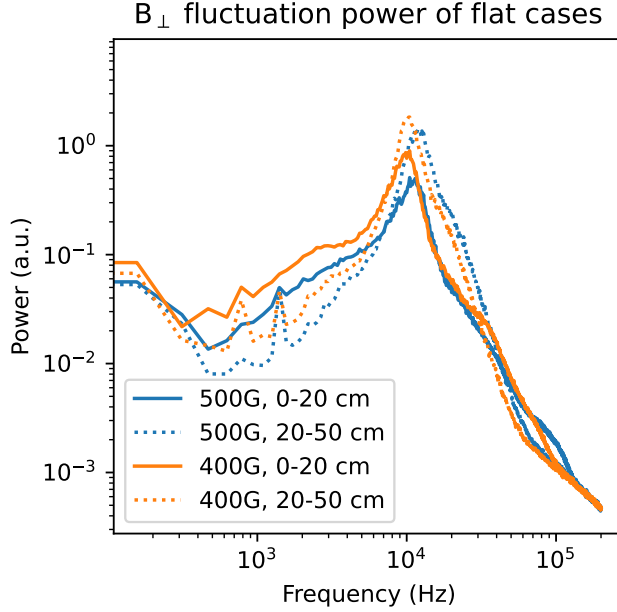


Figure 3.24:  $B_{\perp}$  flat field for 500G and 400G flat fields. The frequency of the identified drift-Alfvén wave at 12 kHz drops when the field is lowered, as expected.

that this is an Alfvénic fluctuation because the wavelength is an order of magnitude too large to fit in the machine.

For completeness,  $B_z$  fluctuation measurements are seen in fig. 3.26. The peaks in the 10 kHz region are likely crosstalk or slight coil misalignment of the probe and are picking up  $B_{\perp}$  fluctuations. The profile low frequency  $B_z$  fluctuations can be seen

The low frequency fluctuations in the Bdot spectra may seem important but plotting the spectra as a function of position (fig. 3.27) clearly shows the harmonics of the signal and the narrow bandwidth of them. This spectral feature is present regardless of mirror ratio, but changes in magnitude in approximate proportion with the field, i.e., the magnet power supply current. This power supply-induced field fluctuation can easily be seen in the  $\approx 625$  Hz mode in  $B_z$ , seen in fig. 3.28. The fluctuation power is largely constant across the entire plasma column, with the fluctuation power increasing with increased mirror fields. The taper of the fluctuation power at the

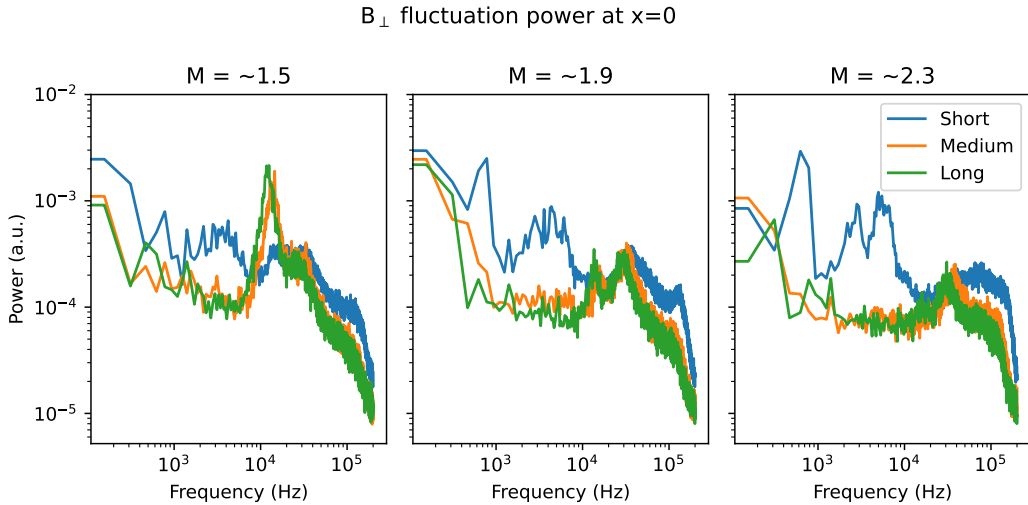


Figure 3.25:  $B_{\perp}$  at  $x=0$  for different mirror lengths. The origin of fluctuations between 1 and 10 kHz is unknown.

edge could be caused by the background field vector no longer pointing in the  $z$  direction as the probe approaches the magnet coil. In general, the probe valves are not centered between the magnet coils, leading to rotation of the field vector as the probe is pulled out.

### 3.4 2d Structure

The perpendicular magnetic field structure is measured by collecting x-y planar bdot ( $dB_{\{x,y,z\}}/dt$ ) data alongside a stationary, axially separated  $I_{\text{sat}}$  reference probe (DR2). This probe provides a phase reference for the magnetic field fluctuations, allowing a 2d map of relative phase to be constructed over many shots. Only the region around  $x_{PF}$  was measured because of constraints on probe movement. The amplitude and phases for each magnetic field component are then used to reconstruct the local magnetic fluctuation vector  $\mathbf{B}$ . The axial current density structure,  $j_z$ , can be derived from this vector field.  $\mathbf{B}$  and the corresponding  $j_z$  for the flat-field ( $M = 1$ ) case can be seen in fig. 3.29. Two main current channels can be seen with the magnetic fields circulating around them. This structure quickly decoheres in time as expected in a turbulent plasma. At higher mirror

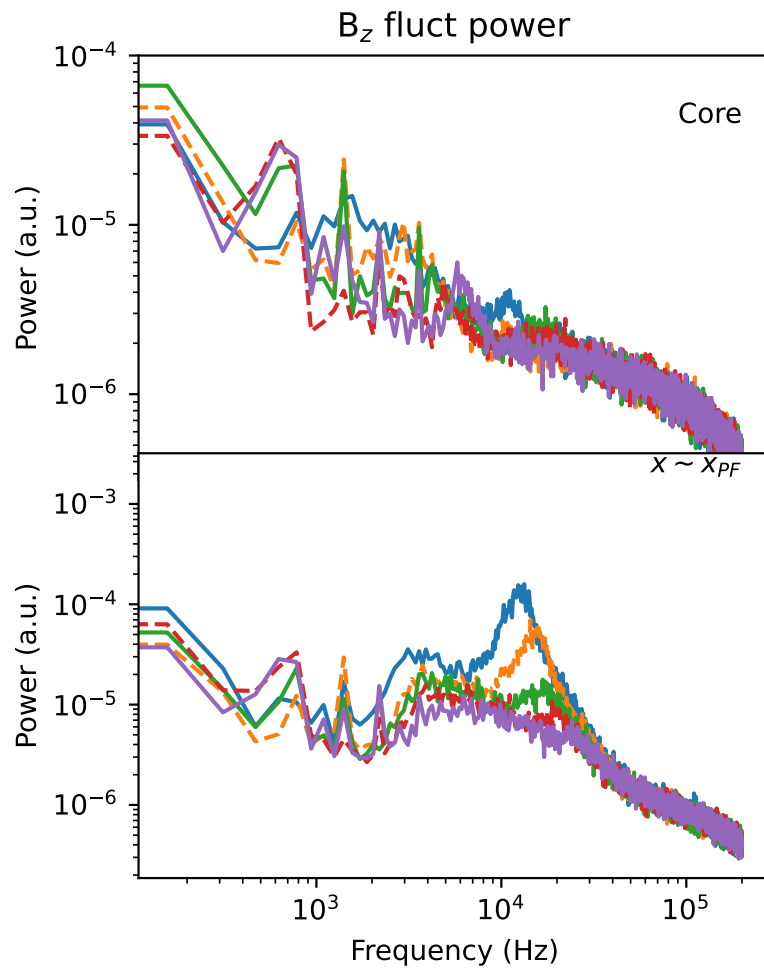


Figure 3.26:  $B_z$  fluctuations in the core and  $x_{PF}$ . Aside from picking up some  $B_\perp$  signal, the spectra are largely featureless.

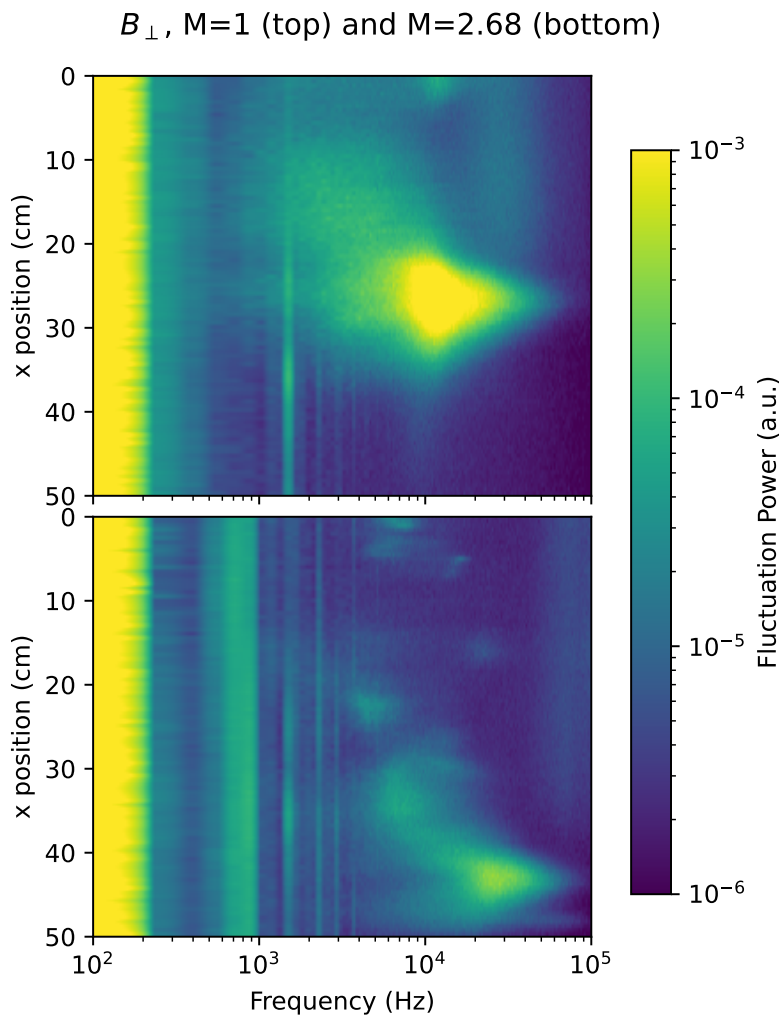


Figure 3.27:  $B_{\perp}$  fluctuation power for mirror ratios of 1 and 2.68. Lower frequencies are shown and the colorbar clipped to show detail in what appears to be power supply fluctuations.

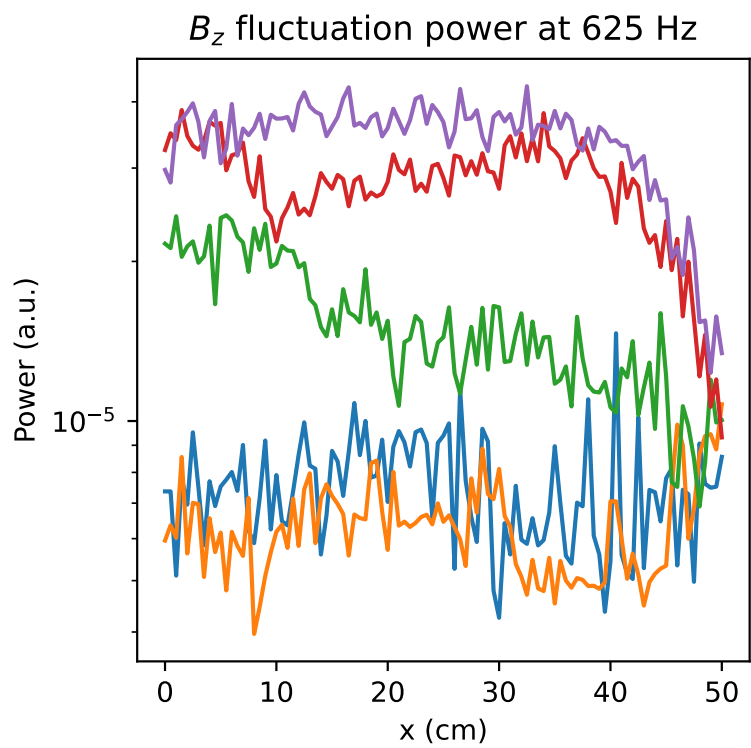


Figure 3.28:  $B_z$  fluctuation power profiles for all mirror ratios at 625 Hz.

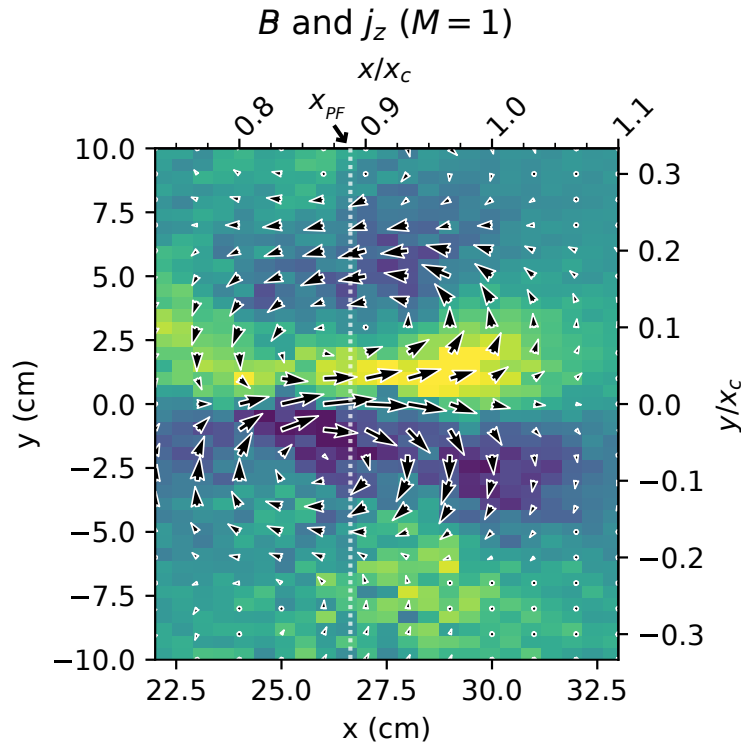


Figure 3.29: Perpendicular magnetic field and the derived current density for the flat-field ( $M = 1$ ) case using a Bdot probe with an axially-separated  $I_{\text{sat}}$  reference (DR2). The x-y plane was centered near  $x_{PF}$ .

ratios, the field magnitude and corresponding current density decrease (which was also seen in DR1: fig. 3.21). Similar structure is seen in the mirror configurations; the  $M = 1.9$  and  $M = 2.68$  cases can be seen in fig. 3.30.

Using two, axially-separated, correlated  $I_{\text{sat}}$  measurements (DR2), with one collecting x-y planar data, the azimuthal mode number  $m$  (radially integrated) was calculated. Higher-frequency and higher- $m$  features are seen with increasing mirror ratio (fig. 3.31). The increased frequencies may be caused by a change in Doppler shift by the  $\mathbf{E} \times \mathbf{B}$  flow. This higher- $m$  trend suggests that azimuthal structures do not scale with increased plasma radius but instead remain roughly the same size. The limited planar probe movement caused an increase in the lower bound on  $m$  in higher

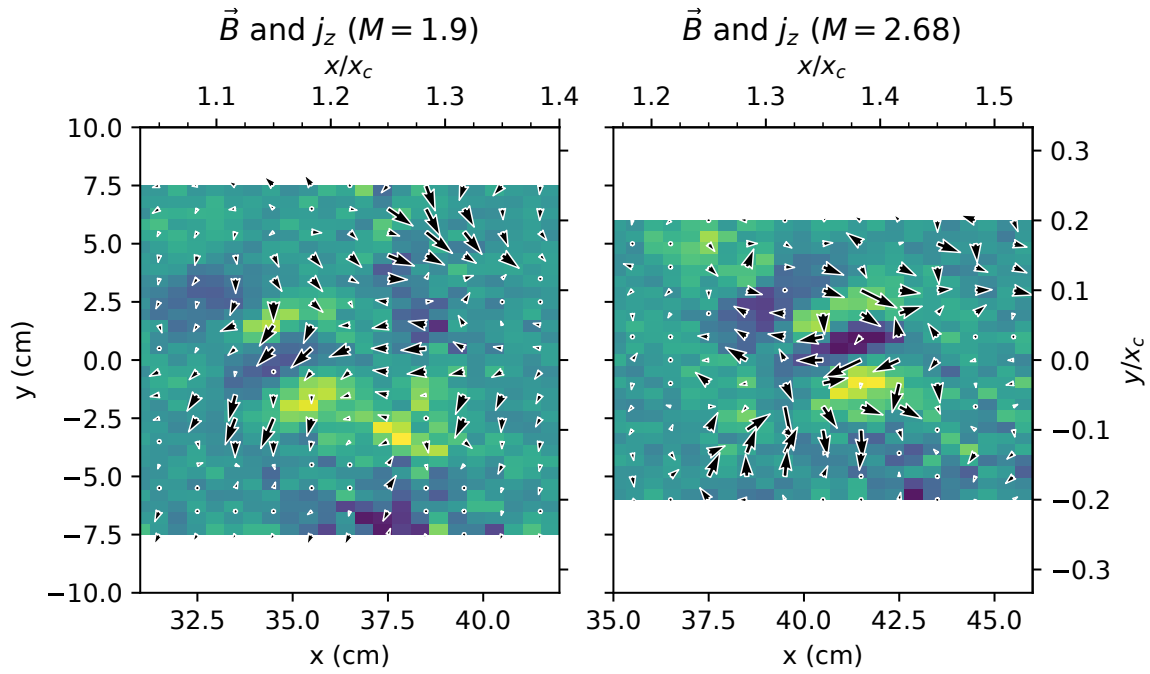


Figure 3.30: Perpendicular magnetic field and the derived current density for the  $M = 1.9$  and  $M = 2.68$  cases computed in the same manner as fig. 3.29. The x-y planes were centered near  $x_{PF}$ , and the view size was kept constant across the plots. The structure is much less obvious in the mirror cases, but all exhibit the expected Alfvèn wave pattern

mirror ratios. At mirror ratios 1.47 and higher, the lower frequency component ( $< 10$  kHz) appears to decrease significantly in amplitude. Calculating  $k_{\perp}$  from  $m$  evaluated at  $x \sim x_c$  yields similar  $k_y$  values as the two-tip technique (fig. 3.32). The average  $k_y$  for a given frequency can be calculated using two Vf tips on the same probe by calculating the phase difference and dividing by the spatial separation of 5 mm:  $k_y = \phi_{vf1, vf2}/\Delta y$  [BKP82]. The maximum  $|k_y|$  measurable before aliasing is  $\pi/\Delta y \approx 628$  rad/m. As seen in fig. 3.32, the  $k_y$  spectrum remains similar across mirror ratios, but the wavenumber extends further into higher frequencies with increasing mirror ratio. These azimuthal mode numbers and gradient scale lengths are consistent with linear simulations using the 3d fluid code BOUT [PUC10] in the flat, unbiased case.

## 3.5 Discussion

### 3.5.1 Lack of mirror-driven instabilities

No evidence is seen for mirror-driven instabilities — curvature, loss-cone, or otherwise. Given the LAPD parameters in this study (tables 3.1 and 3.2), the collision frequencies are sufficiently high such that the mirror is in the gas-dynamic regime: losses out of the mirror throat are governed by gas-dynamic equations rather than free streaming through the loss cone. To be in the gas-dynamic regime, the mirror length must exceed the mean free path of the ions [IP13]:

$$L > \lambda_{ii} \ln M/M \quad (3.2)$$

where  $L$  is the mirror length,  $\lambda_{ii}$  is the ion mean free path, and  $M$  is the mirror ratio. These collisions populate the loss cone and maintain a (cold) Maxwellian distribution, eliminating the possibility of loss-cone-, ion-driven instabilities like the AIC [CS82] or DCLC [Sim76, Kan79] instabilities that have been observed in other (historic) devices.

The paraxial, approximate interchange growth rate is [Pos87, RBC11]

$$\Gamma_0 = \frac{c_s}{\sqrt{L_M L_P}} \quad (3.3)$$

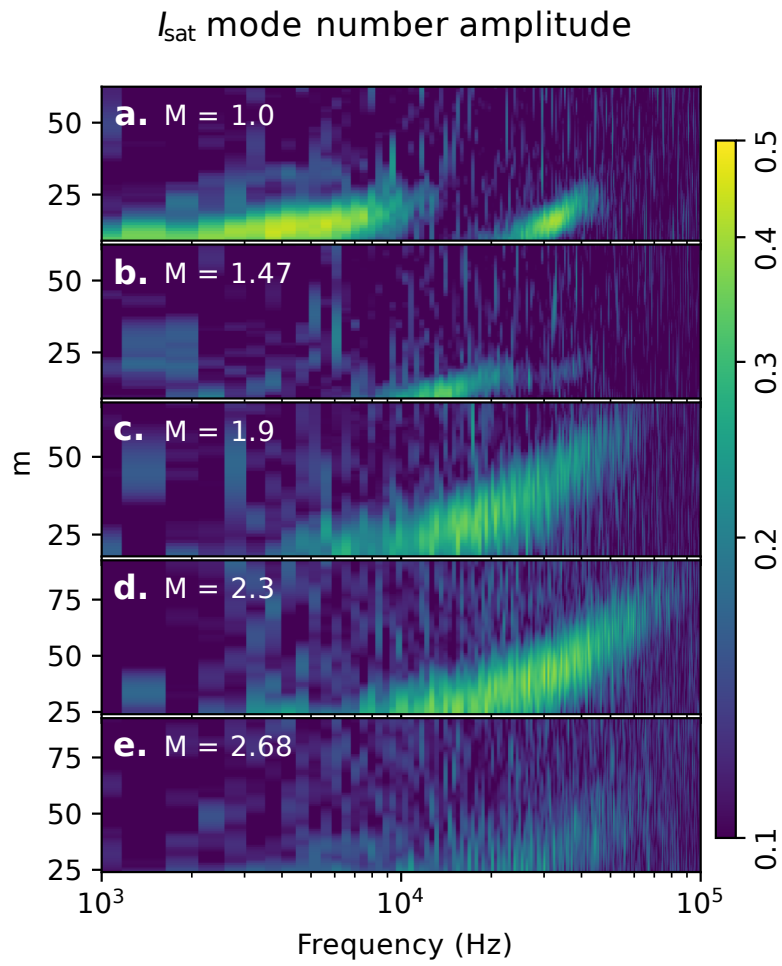


Figure 3.31: Azimuthal mode number  $m$  amplitudes calculated from two axially-separated, correlated,  $I_{\text{sat}}$  probes. Increasing mirror ratio (a to e) leads to increased  $m$  at higher frequencies. (DR2)

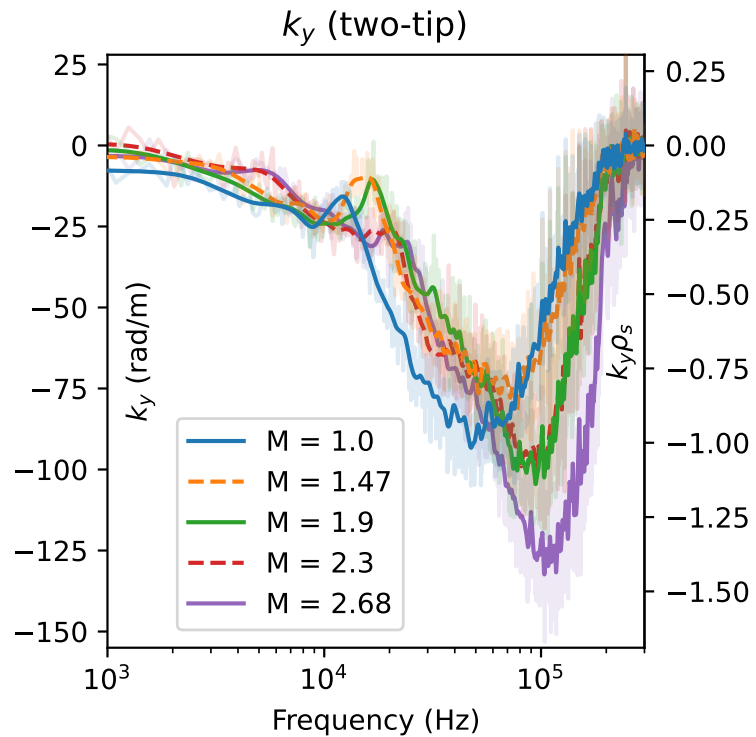


Figure 3.32:  $k_y$  averaged about  $x_{PF}$  and smoothed for each mirror ratio calculated using two vertically-separated Vf tips on the same probe. Little change is seen in  $k_y$  at lower frequencies but higher frequencies tend towards larger  $k_y$  at higher mirror ratios.

which yields  $\Gamma_0 \approx 1.2$  kHz using  $L_M \approx 7$ m and  $L_P = 17$ m.  $c_s$  is used instead of  $\bar{v}_i$  because  $T_i \ll T_e$  and mirror length  $L$  is split to distinguish between the contributions of the plasma length and mirror length to inertia and to curvature drive, respectively. Interchange is not visible in-part because the aspect ratio of these mirrors is quite large, limiting the growth rate of interchange. The length of the mirror (3.5 m), radius of curvature (6-7 m), and plasma column (17 m) are much larger than the radius of the plasma (0.5 m maximum), so the plasma inertia is large relative to the instability drivers. Line-tying to the cathode may further lower the growth rate. The hot cathode used for plasma formation could function as a thermionic endplate that can supply current to short out the flute-like interchange perturbations. Line-tying has been seen in flux rope experiments on the LAPD using a hotter, denser source [VGP11], also in other devices [FKR79], and is why interchange was not seen in the earliest mirror machines [Pos87]. Note that the plasma terminates on the cathode or end plates before the magnetic field flares out, so there is no contribution to stability from an expander tank as seen in other GDTs [RBC11, IP13]. Finite Larmor radius (FLR) effects may provide a stabilizing effect for larger azimuthal mode numbers. At the highest mirror ratio, assuming a plasma radius of  $a_0 = \sqrt{2.68} * x_{PF} = 43$  cm, the FLR stability criterion  $\frac{m}{2} \frac{\rho_i L}{a_0^2} > 1$  [RBC11] suggests a stabilizing effect may be present for azimuthal mode numbers  $m > 4$ .

If the curvature-induced interchange instability were observable, then introducing a mirror configuration would lead to new features in  $I_{\text{sat}}$  and  $B_{\text{dot}}$  fluctuations. In particular, low-frequency mode(s) – likely less than 10 kHz given the low m-number and plasma rotation rates – would be observed growing from the pressure gradient region. For onset of the interchange instability, the mirror curvature or plasma pressure would need to be increased but the precise conditions required for this onset are not yet known for the LAPD.

Interchange could also be at least partially stabilized by the continuous production of electrons in the core that are electrostatically trapped by the ambipolar potential [GH71]. The intuition behind this stabilization mechanism is as follows: electrons are continuously produced via ionization of neutrals, and any change in the local potential will cause more or fewer electrons to be lost out the ends of the device along that field line, counteracting the potential change. This stabilization

mechanism has been experimentally demonstrated to completely suppress interchange when the ambipolar potential  $\Phi \gtrsim 6T_e$  [KHS87].

The  $\mathbf{E} \times \mathbf{B}$  shear flow present (fig. 3.7) may also make a contribution to the stabilization of interchange [RBC11, BLZ03, BBS07, BBC10]. The estimated shearing rate is between 3 and 10 kHz, which is greater than the estimated  $\approx 1.2$  kHz growth rate of the interchange mode.

### 3.5.2 Instabilities driving LAPD turbulence

Rotational interchange can be significant driver of the broadband turbulence spectrum in the LAPD, particularly when a biased limiter is installed. This observation has been confirmed by both linear simulations [PUC10] and biasing experiments [Sch13].

This rotational interchange mode has the following attributes, as summarized by [Jas72]: flute-like ( $k_{\parallel} = 0$ ),  $|e\tilde{\phi}/T_e|/|\tilde{n}/n| \gtrsim 1$ , radial potential phase variation 45 to 90°, maximum possible  $|e\tilde{\phi}/T_e| < 1$ . All of these attributes are seen for the lower frequency (3 kHz) mode. The Vf radial phase variation when  $M > 1$  is not clearly seen because the coherency is dramatically reduced along the field line. The rotational interchange mode could couple with the drift wave at  $k_{\parallel} = \pi/L \sim 0.37$  rad/m ( $n = 0.5$ ), which has been observed in the past [Sch13] and likely present here. Estimates of shearing rate from the  $\mathbf{E} \times \mathbf{B}$  flow velocity profile (fig. 3.7), calculated fluctuation ratios, and radial phase shift variation suggest that Kelvin-Helmholtz-driven turbulence is not significant, if present at all. Historically, biasing a limiter has been required to clearly observe the Kelvin-Helmholtz instability [HPC05, SCR12, Sch13].

Low frequency density fluctuations may also be driven by a flute-like conducting-wall temperature-gradient instability which only requires an electron temperature gradient to grow (even with straight field lines) [BRT91]. Simulations of turbulence in the LAPD suggest the possible presence of these conducting wall modes (CWM) which have the highest growth rate for  $m \leq 20$  [FCU13]. This lower- $m$  mode could be responsible for the peak around 3 kHz in the  $M = 1 I_{\text{sat}}$  fluctuation (fig. 3.16) and azimuthal mode numbers (fig. 3.31) and for the low-frequency low- $k_{\parallel}$  or flute-like

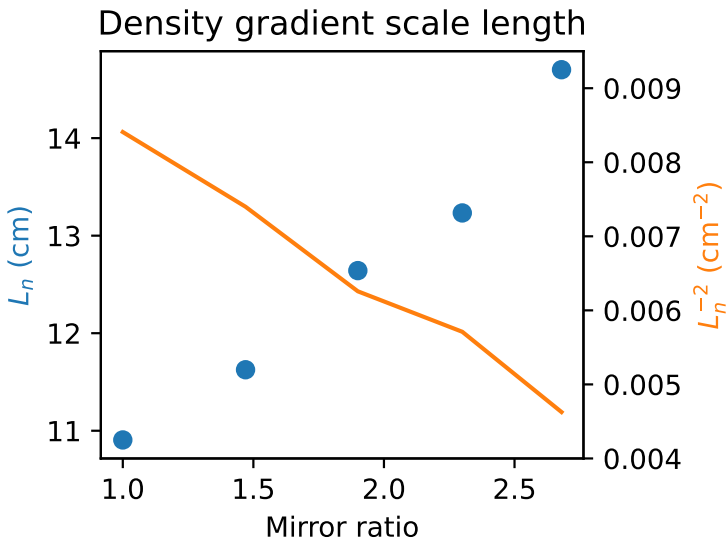


Figure 3.33: Gradient scale length  $L_n$  and the associated term in the drift wave growth rate  $L_n^{-2}$ . This scale length was calculated over a 3 cm region around  $x_{\text{PF}}$  (peak fluctuation region) at the midplane. Increasing the mirror ratio increases the gradient scale length, which suggests weakening of the underlying instability driver.

behavior (fig. 3.17). This CWM may also be responsible for flatter electron temperature profiles seen in previous studies [PMC22, Sch13] (fig. 3.6).

These linearly unstable modes may be outgrown by a rapidly-growing nonlinear instability that couples to drift-like modes as suggested by simulations [FCU13]. This nonlinear instability is driven by the density gradient at an axial modenumber of  $n = 0$  and nonlinearly transfers energy to  $n \neq 0$  fluctuations.

The conducting wall mode and nonlinear instability may be present in these mirror experiments but the spectra are adequately explained by linearly unstable modes. Precise identification these modes requires further study; neither of these instabilities have been directly observed in the LAPD.

### 3.5.3 Causes of particle flux reduction

The reduction in particle flux explained by a reduction in density fluctuations likely caused by a increased gradient scale length  $L_n = \frac{n}{\nabla n}$  (fig. 3.33), decreasing the linear drift wave growth rate and saturation level seen in sec. 3.3.5. This gradient length reduction may also reduce the growth rate of the rotational interchange instability, which may be the dominate driver for the low-frequency large-amplitude density fluctuations. The influence of this density fluctuation reduction appears reduced at higher mirror ratios past  $M = 1.9$ , where the wavenumber and phase angle appear to decrease in magnitude. The plot showing this breakdown in particle flux can be seen in fig. 3.34. The changes in  $I_{\text{sat}}$  fluctuation power is the most obvious driver, but the  $I_{\text{sat}} - V_f$  phase difference, coherency and wavenumber also seem to have an effect. The  $V_f$  fluctuation power remains largely consistent across the different mirror ratios. Note that this particle flux appears somewhat different because this is using the uncalibrated  $I_{\text{sat}}$  values and the flux is not scaled by solid angle. This flux also does not use temperature-compensated  $I_{\text{sat}}$  measurements.

The decorrelation time of  $I_{\text{sat}}$  time series data is around 0.15 ms at  $x_{PF}$ . An estimate of the  $\mathbf{E} \times \mathbf{B}$  flow shear from fig. 3.7 (DR2) yields a shearing time between 0.1 and 0.3 ms at  $x_{PF}$ . These times suggest that spontaneous flow shear may be important for suppressing turbulence, as seen in other studies [SCR13, CYK05], at all mirror ratios. However, no clear trend in shearing strength is seen with mirror ratio.

The decorrelation time of a signal is calculated by taking the autocorrelation of a signal –  $I_{\text{sat}}$  in this case – and finding the full-width half-max of the envelope using a Hilbert transform. This decorrelation time can be seen in fig. 3.35. The decorrelation is minimized at  $x_{PF}$  and maximized in the core, further confirming the turbulent nature of the fluctuations at  $x_{PF}$ .

The estimated shearing rate from DR2 can be seen in fig. 3.36. The rate is plotted instead of time because of the singularity when the flow reverses. At around  $x_{PF}$  ( $x/x_c \approx 0.87$ ), the shearing rate is around 2 to 8 kHz meaning the shearing time is around 0.5 to 0.125 ms. This is fairly close to the decorrelation time from the  $I_{\text{sat}}$  time series measurements (fig. 3.35). These similar times/rates

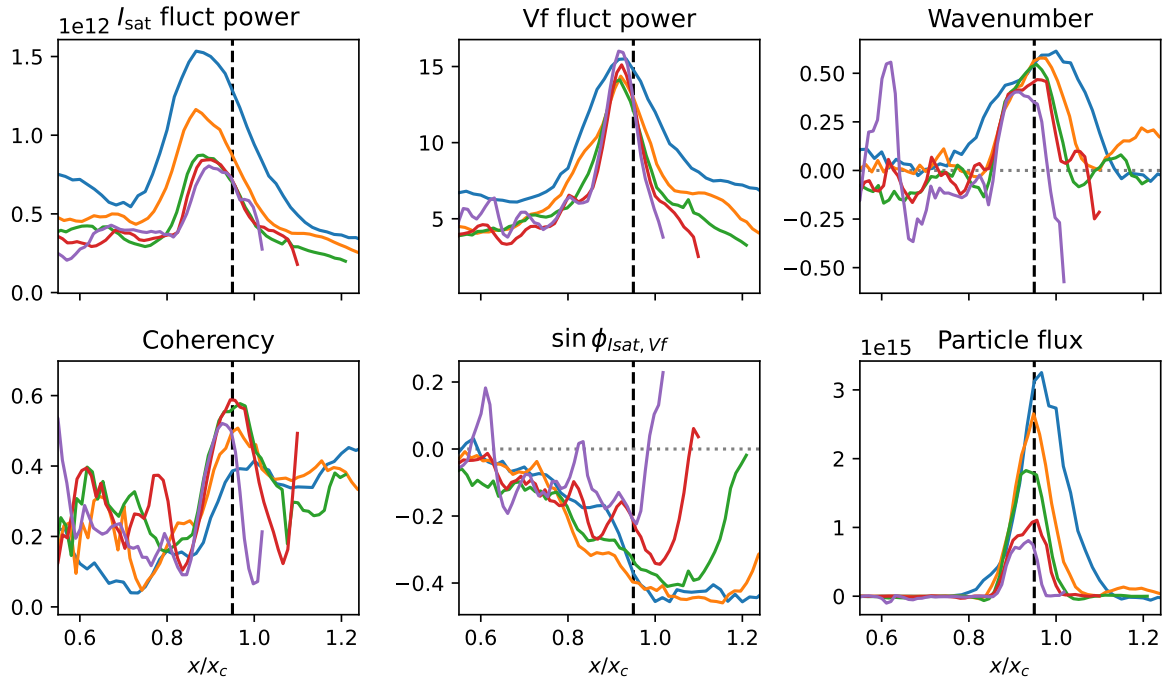


Figure 3.34: The particle flux broken down into the components used to calculate it. The dashed black line is simply a visual reference near the peak particle flux at  $x/x_c = 0.95$ . The  $I_{\text{sat}}$  fluctuation power appears to be the largest driver in changes in particle flux. The colored lines correspond to mirror ratio as seen in earlier plots.

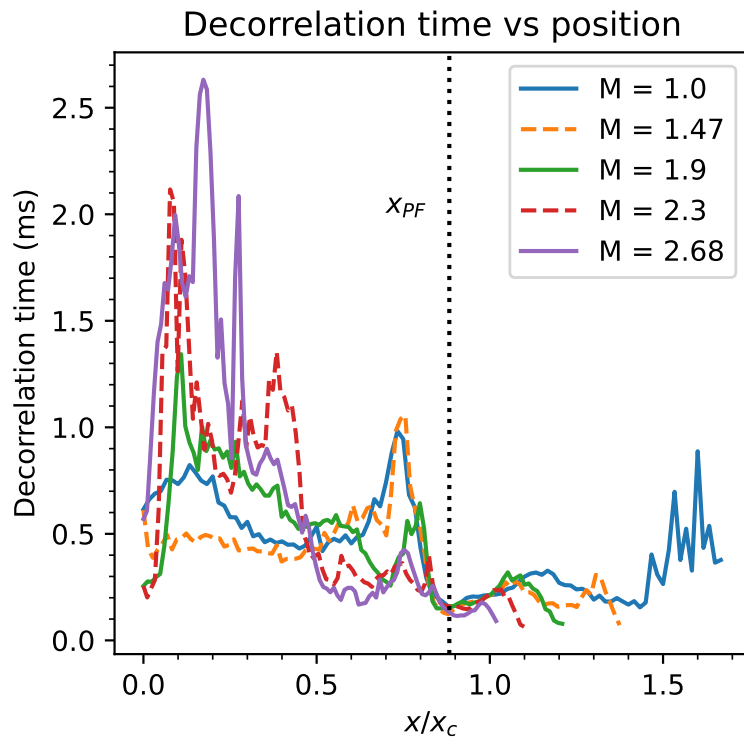


Figure 3.35: Decorrelation time from  $I_{\text{sat}}$  time series data for different mirror ratios. All of the mirror ratios have a minimum decorrelation time at  $x_{PF}$  and much longer times (slower rate) in the core.

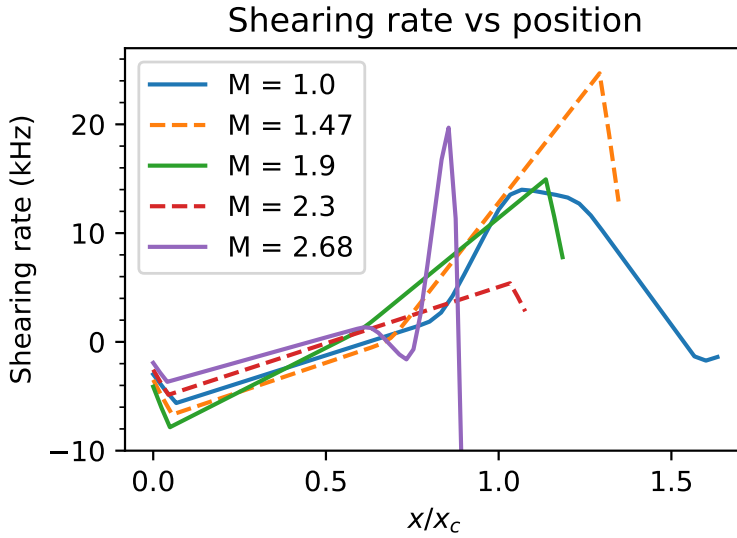


Figure 3.36: ExB shearing rate based on smoothed plasma potential profiles. This shearing rate is comparable to the decorrelation rate at  $x_{PF}$ , seen in fig. 3.35.

suggests that ExB shearing may set the limit on cross-field transport.

It is important to note that the electron thermal diffusion time along the field line is very long compared to the frequency of the drift wave ( $\omega \gtrsim k_{\parallel} \bar{v}_e^2 / v_{ei}$ ) [Gol95] so the electron temperature along the field line may not be constant on the drift wave timescale. This factor is not taken into account in this analysis but may have substantial impact on interpretations of the measured phase shift.

### 3.5.4 Differences between DR1 and DR2

Directly applying signals between these two dataruns is not quite appropriate because the profiles/plasmas changed appreciably. These changes could have been caused by differences in cathode temperature, emissivity, or other properties. The discharge power for DR2 was roughly 10% smaller than what was seen in DR2 seen in fig. 3.37. Since the discharge voltages were similar (DR1: 62.5 vs DR2: 60.5) we expect to see less dense plasmas in DR2.

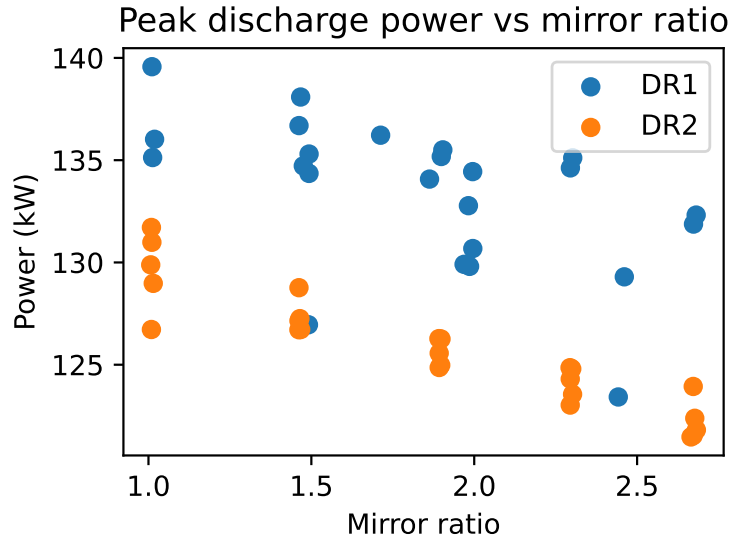


Figure 3.37: Discharge power vs mirror ratio. DR2 had roughly 5% lower discharge power than in DR2 for unknown reasons.

Changes in the  $I_{\text{sat}}$  profiles between the two dataruns (and between two separate measurements in DR1) can be seen in fig. 3.38. Interestingly, there is some difference in the profiles *within the same datarun* which could be caused by probe shadowing. Probe shadowing effects should be less important in mirrors because the probe closest to the cathode magnetically maps to a region further outside than the probes in the mirror cell. This difference in density can also be seen in the line-integrated density from the 56 GHz interferometer (port 23): fig. 3.39. These differences in density could also be caused by different hydrogen and helium pressures in the runs. Helium pressure was roughly the same for both dataruns ( $6 \times 10^{-6}$  to  $3 \times 10^{-6}$  for DR1,  $6 \times 10^{-6}$  to  $2 \times 10^{-5}$  for DR2), but the hydrogen pressure was an order of magnitude higher for the DR2, on the order  $7 \times 10^{-6}$  instead of  $1 \times 10^{-7}$  for DR1. These differences in pressures could have had an effect on plasma formation and transport, thus affecting profiles. Hydrogen fraction is known to have an effect on breakdown characteristics in the newer Lanthanum-hexaboride (LaB<sub>6</sub>) cathode.

Differences could also occur within dataruns. Calibrating the effective area of the  $I_{\text{sat}}$  probes can be done using the 56 GHz interferometer, but this calibration factor drifted over time and seen in fig.

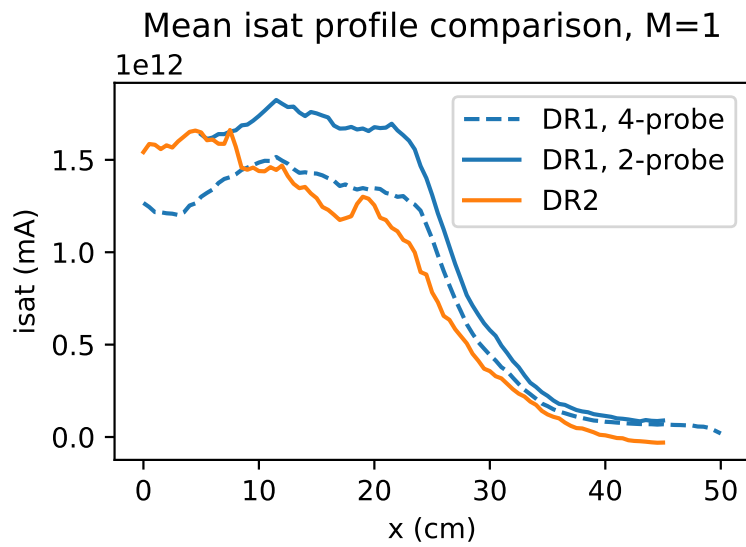


Figure 3.38:  $I_{\text{sat}}$  profiles ( $M=1$ ), DR1 vs DR2 in the mirror cell. DR2 has reduced  $I_{\text{sat}}$  across the entire profile. Identical machine settings in DR1 a few days apart are also different.

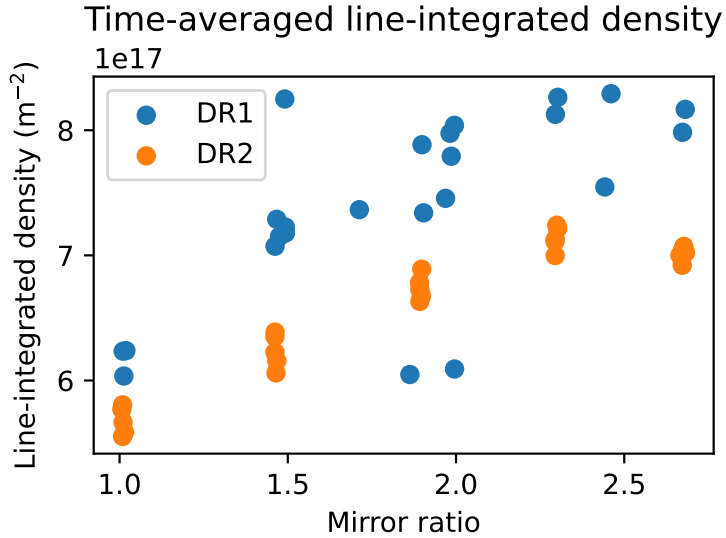


Figure 3.39: Line integrated density from the 56 GHz, DR1 vs DR2. On average, DR2 has a lower density than what's seen in DR1. The interferometer is located near the region of good curvature closest to the cathode.

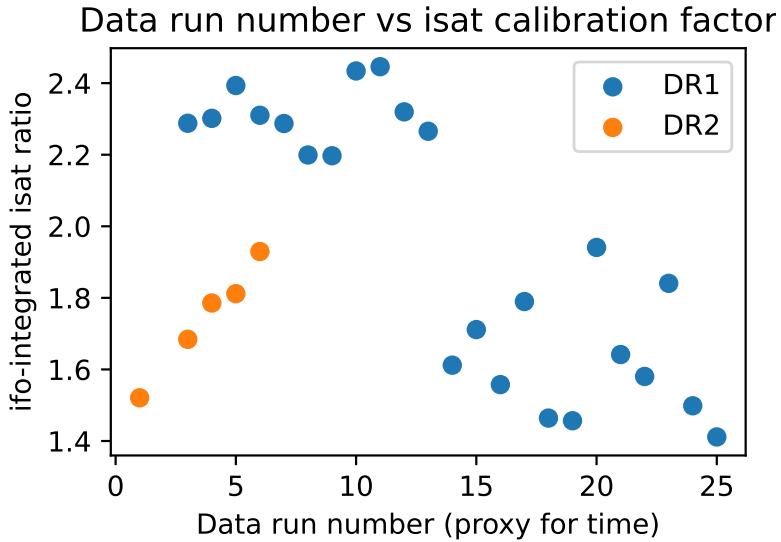


Figure 3.40:  $I_{\text{sat}}$  calibration factor over different dataruns from the same run sets. Datarun number is monotonically increasing, so in this case it's used as a proxy for time. A rather large variance is seen in this calibration factor, which suggests the  $I_{\text{sat}}$  probes having time-varying characteristics affecting the measurement.

3.40. This could be deposits being removed or added to the probe, affecting the effective area. This calls into question the reliability of absolute  $I_{\text{sat}}$  measurements, but we proceed regardless because there's no easy way to fix this issue.

### 3.6 Conclusions and future work

Turbulence and transport was studied in mirrors with varying lengths and ratios using the flexible magnetic geometry of the LAPD. Particle flux and fluctuation amplitudes decreased up to a factor of two when mirror ratio was increased. The primary drivers of turbulence were identified as the rotational interchange mode, caused by spontaneous rotation, and unstable drift-Alfvén waves driven by the density gradient. The decrease in density fluctuation amplitudes can be attributed to an increase in the gradient scale length caused by the dimensionally wider plasma at the mirror

midplane. Despite imposing a mirror configuration, no signs of mirror-driven instabilities were observed. The highly-collisional, GDT-like plasma produced suppressed any velocity space instabilities. The interchange growth rate was likely suppressed to an undetectable level by line-tying, in-cell electron production, and shear flow.

Future experiments in hotter regimes with the new LaB6 cathode [QGP23b] will need to be performed to evaluate the robustness of these results, particularly concerning the stabilization of curvature-induced interchange. Additionally, the source field should be matched to the mirror midplane field so that the plasma remains the same radius to isolate geometric effects. Simultaneous measurements using flux and/or vorticity probes and  $I_{\text{sat}}$  are needed to concretely determine if azimuthal flow shear is modified by the mirror field, and to quantify the effect of flows on rotational interchange and drift wave instability drive in general. Multiple simultaneous axial measurements of potential would enable better understanding of the axial wavenumber and identification of possible modes.

# CHAPTER 4

## Creating a randomized dataset for machine learning tasks

### 4.1 Goal and introduction

The goal of collecting this dataset was to maximize the diversity of data coming from the LAPD. Previous datasets – even one made of 29 million passively-collected shots over three years – did not contain sufficient diversity to do an interesting ML study. In particular, the data must be sufficiently diverse to allow an optimization study without the need to collect more data. In addition, many diagnostics were recorded so that the signals could be correlated on the same shot, either in the machine learning model itself or as a preprocessing step. This chapter describes the process of collecting this data, example signals, and biases within the dataset. All of the data from this campaign (several terabytes) is available upon request.

The LAPD has many experimental control parameters for various physics studies. While the device can accommodate various insertable components, this dataset focuses on the parameters fundamental to the operation of the main cathode. Specifically, half way between the cathode and anode are three gas puff valves: East, West, and top. The aperture, duration, and triggering of these valves has a large impact on plasma formation. A static gas fill system also exists but it is not used. The cathode-anode voltage (and consequently, discharge power) strongly influences plasma density and temperature downstream of the source. Additionally, the magnetic field configuration substantially shapes the plasma column. One crucial variable not considered in this dataset is the cathode temperature, as its adjustment and equilibration requires many hours, limiting dataset diversity. This combination of diagnostic coverage, high repetition rate, and extensive configurability

renders the LAPD particularly suitable for machine learning studies.

## 4.2 Configuration of the LAPD

Data collection was conducted in two campaigns separated by 14 months. The initial run set is designated as DR1 and the subsequent run set as DR2. These run sets are further broken down into *dataruns* which are series of discharges (“shots”) with identical operational machine parameters. A total of 67 dataruns were collected over both campaigns. These two datarun sets had significant intrinsic differences: DR1 had two turbomolecular pumps offline, leading to much higher background pressures. In addition, the cathode condition in terms of emissivity or asymmetries is unquantified, so there may be intrinsic differences in the plasma produced regardless of machine configuration.

The LAPD control parameters varied in this dataset were the source field, mirror field, midplane field, gas puff valve voltage, gas puff duration, and discharge voltage. The magnetic field regions are labeled in fig. 4.2 and effectively control the width of the plasma relative to the cathode in their respective regions. The gas puff voltage governs gas flow rate into the chamber, though this relationship is not yet quantified, and the gas puff duration defines the piezo valve activation period. For DR1, the discharge voltage is applied across the cathode and anode at the same time as the gas puff, but for DR2 applied 10 ms after gas puff initiation. This difference between runs was not known at experiment time. While discharge voltage correlates to discharge current (and thus power), the current depends on the machine configuration and downstream conditions and cannot be predetermined.

These machine parameters – with the exception of gas puff duration – were randomly sampled via Latin-hypercube sampling (LHS) for 44 of the dataruns. LHS is a pseudorandom sampler that guarantees that each machine setting is set at least once. An example of LHS vs random sampling can be seen in fig. 4.1. It is possible for random sampling to miss certain machine settings, or entire portions of configuration space altogether. This fact is particularly important when the number of samples is small, such as in this case with 44 samples. Data were then collected with these settings.

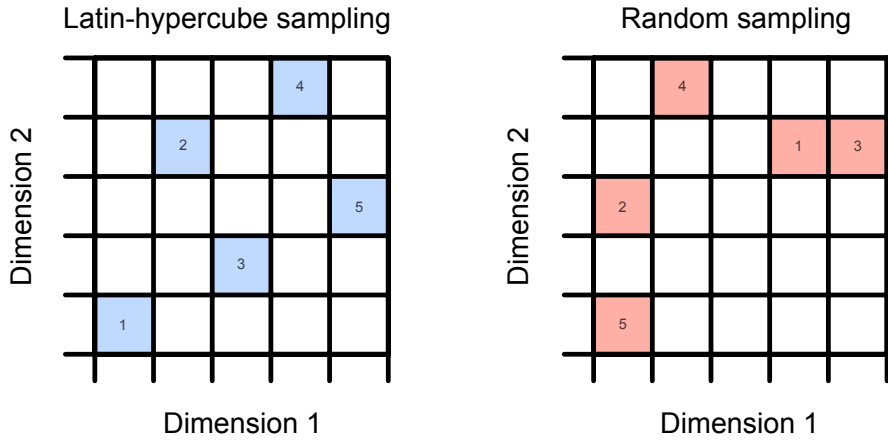


Figure 4.1: An example of Latin Hypercube Sampling compared to a potential random sample of five points. LHS hits all rows and columns, but random sampling may leave some sections of parameter unsampled space altogether.

Gas puff duration was reduced for the last seven runs to 20, 10, or 5 ms (see fig. 5.3 for timings relative to  $I_{\text{sat}}$  signals). The breakdown of each setting in the dataset is given in appendix 4.5, Table 4.1. The top gas puff valve was used for only the first nine dataruns of DR2 because of equipment issues. 23 of the dataruns in the dataset are not random: they were chosen to be similar to common machine configurations used in more conventional studies, usually using flat fields (or different cathode fields) around 1 kG. These data were taken while other diagnostics were being configured.

$I_{\text{sat}}$  and other probe-based measurements were acquired along  $y=0$  lines (51 dataruns total) or  $x-y$  grids (16 dataruns total) with spatial resolutions varying between 1.5 to 2 cm. The fixed axial locations of the probes were 895 cm and 831 in DR1 and 1150, 1022, 863, and 639 cm for DR2 (Fig. 5.1). Six shots were recorded at each position except for the first four dataruns in DR1 with five shots each.

### 4.3 Signals collected

DR1 and DR2 had considerable overlap in diagnostics recorded, with some minor difference. A summary of the diagnostics and their locations on the LAPD can be seen in fig. 4.2. Some of the raw diagnostics signals and machine state information (MSI) can be seen in fig. 4.3. Some dataruns may not contain all diagnostics, as some data were collected while other diagnostics were being set up. The diagnostics and machine state information (MSI) recorded for this dataset are the following:

- **DR1 probes:** three probes were inserted into the LAPD. One had Langmuir sweeps, another "flux probe" had  $I_{\text{sat}}$  and two floating potential ( $V_f$ ) tips, and the last "triple probe" had  $I_{\text{sat}}$ ,  $V_f$  and electron temperature ( $T_e$ ). These signals were digitized at 6.25 MHz (100 MHz, 16 sample average).
- **DR2 probes:** four probes were inserted, namely a flux probe, triple probe, Langmuir sweeps with  $I_{\text{sat}}$  on a separate tip, and another flux probe. These signals were digitized at 6.25 MHz (100 MHz, 16 sample average).
- **Diodes:** five diodes, axially distributed, were recorded as well. The one closest to the cathode had a He-II line filter. The diodes were uncalibrated, have a nonlinear response, and are sensitive beyond the visible spectrum. These diodes were a part of the MSI system and were recorded at 25 kHz. Each diode (besides the one with the He-II filter) had 8 layers of 1-stop (50% transmission) neutral density filter in front of the diode.
- **Interferometer:** signals from the 288 GHz heterodyne interferometer was recorded on an oscilloscope at 10 MHz, which was then downsampled to 100 kHz before analysis so that the processing computer could keep pace.
- **Thomson scattering:** a single point was measured on-axis at port 32, triggered at 8 ms into the plasma for DR1 or 12 ms for DR2. Periodically the collection optics were scanned to maximize the light collected. during both run set.

- **Spectrometer:** an ocean optics HR4000 spectrometer recorded spectra integrated over the duration of the shot. The spectrometer has a very narrow slit, leading to good spectral resolution but requiring many shots for a clean spectrum.
- **Monochromator (DR2 only):** three Helium neutral lines were recorded, namely 587, 667, and 707 nm, using an oscilloscope sampling at 1 MHz.
- **Diamagnetic loop:** the loop sits between ports 34 and 35 and consists of one large loop and two smaller concentric loops equaling the area of the large one. These signals were digitized using an oscilloscope at 500 kHz, but are strongly influenced by magnet power supply noise making analysis difficult.
- **Fast framing camera:** a Phantom v7.3 fast framing camera recorded plasma dynamics from the end of the machine, pointing towards the cathode. The images are monochrome, 14 bit, 14  $\mu$ s exposure,  $256 \times 256$  pixels, and 2,500 fps using a 105 mm lens. The camera is capable of 36,697 fps at that resolution, but a lower one was used to lessen file transfer times and storage requirements.
- **Discharge current and voltage:** as part of the MSI system, time evolution of the discharge current and voltage are recorded at 25 kHz.
- **Magnetic field profiles:** theoretical on-axis magnetic field values are calculated using the magnet power supplies. Both are recorded as part of the MSI. For the work here, we simply use the programmed field values for the cathode, mirror, and midplane regions. Occasionally the calculated field would be incorrect since the power supply currents for the cathode are set manually, which is the case in some dataruns here, but the profiles are unused in these studies so it isn't an issue.
- **Pressures:** total pressure and pressure breakdown by atomic mass unit are recorded by an ion gauge and RGA, respectively. The RGA takes around a couple minutes to complete a scan but the data should be reasonably accurate given the slow time-evolution of pressure.

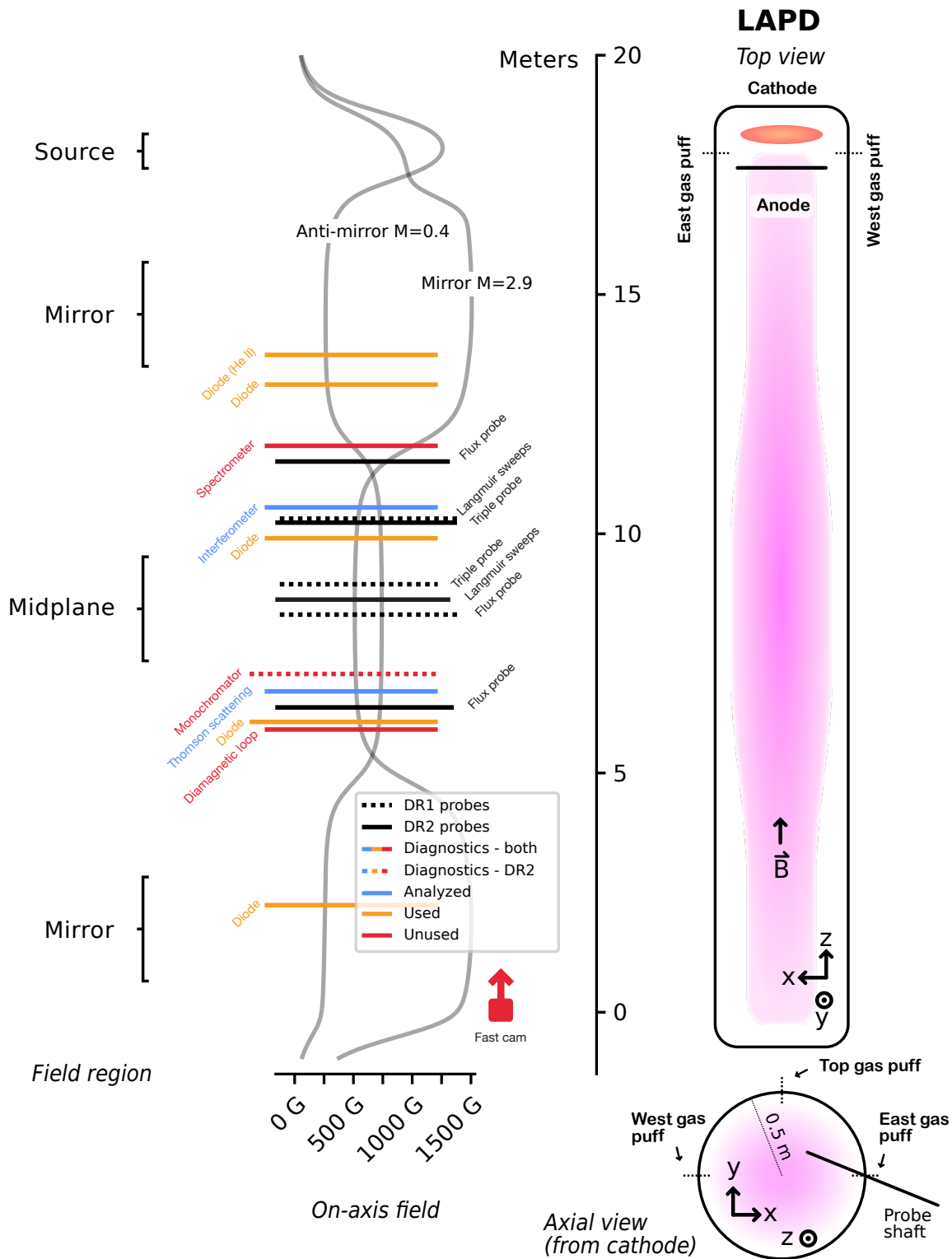


Figure 4.2: Diagnostics and example field configurations for DR1 and DR2

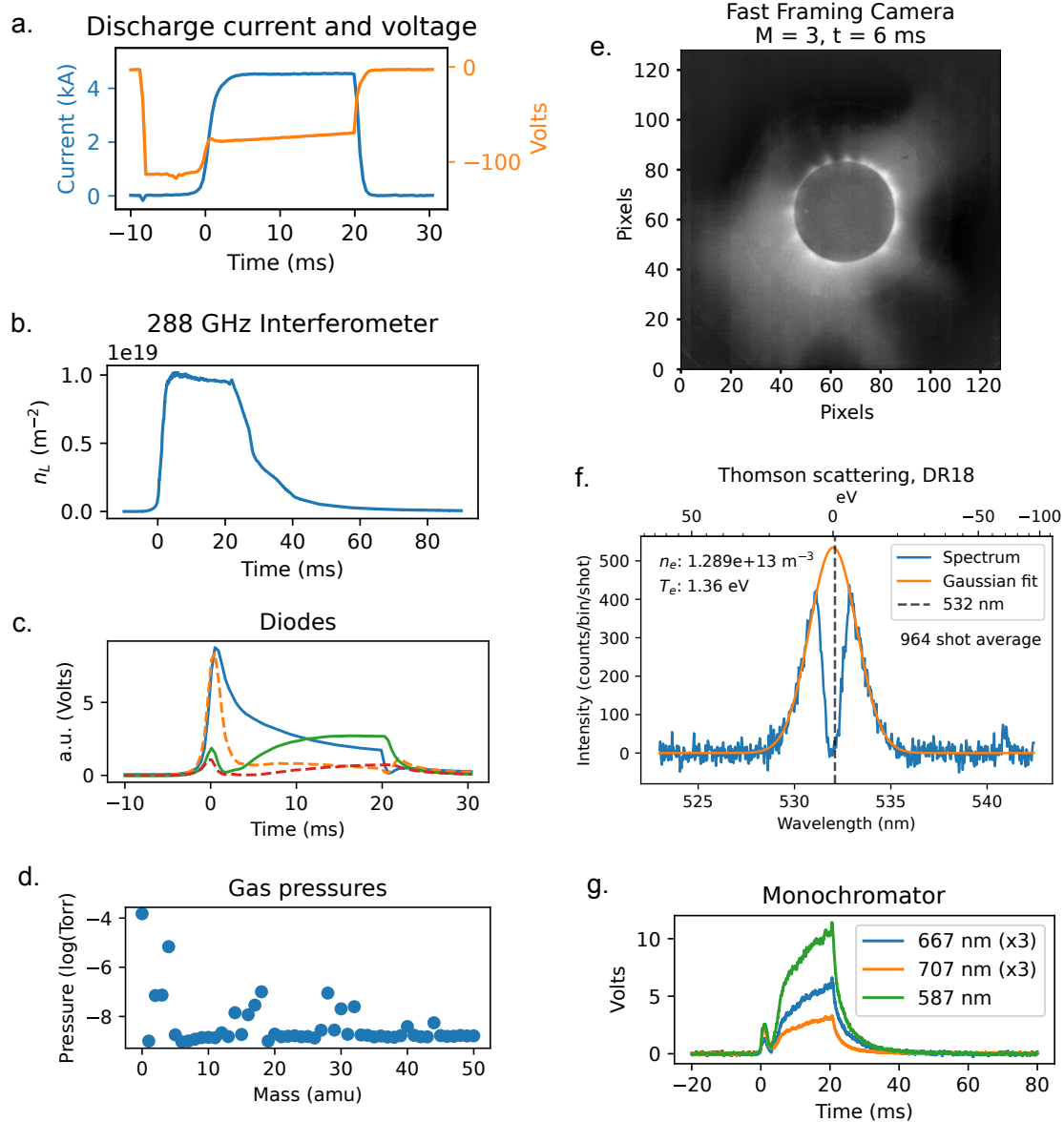


Figure 4.3: Example diagnostic signals and machine state information from a variety of discharges.

Of the probes, only  $I_{\text{sat}}$  was analyzed and used. The interferometer and Thomson scattering signals were also analyzed. The diode signals were unanalyzed but used in a downstream machine learning study. The spectrometer, monochromator, and diamagnetic loop remain unanalyzed and unused, but the raw signals could be useful for ML studies as will be shown with the diode signals (see chapter 6). The fast framing camera was useful for checking probe alignment and visualizing plasma structure, but it was otherwise not used or analyzed for the downstream ML studies.

## 4.4 Data cleaning

$I_{\text{sat}}$  measurements in DR1 that saturated either the isolation amplifier or digitizer are excluded from the dataset. Only 484 shots were removed out of  $\approx 132,000$ , so the impact on the aggregate dataset is minimal. This signal saturation was detected while data was being taken and was corrected quickly.

Interferometer skips were occasionally seen, likely caused by large  $\delta n/n$  structures combined with downsampling before conversion of the signal into a density measurement. Attempts were made to unwrap these skipping traces (see fig. 4.4) but without much success, so these shots were cut from the dataset.

The Thomson scattering (TS) diagnostic was available only for dataruns 8 and onwards in DR1. The TS image data did not have timestamps recorded, so a rough estimate was used based on filename and last saved time. Uncertainty in time is tolerable because conditions were identical to datarun shots for a few minutes before and after the dataruns. Fits were taken of the average over the entire datarun; each shot in a datarun has the same recorded TS temperature and density. Dataruns were removed if the error on the density, measured by the square root of the covariance of the fit amplitude, was greater than 50%. Fits above that error threshold were largely unusable. A couple of dataruns looked like pure noise even when averaged over several hundred shots, but were not caught by this broad criteria. 24 dataruns remained out of 30. In some runs there was high-pixel-frequency noise at 128 and 256 (every 4th and 2nd pixel, respectively). The fitting routine is typically insensitive to this cleaning process, but big differences can be seen in particularly

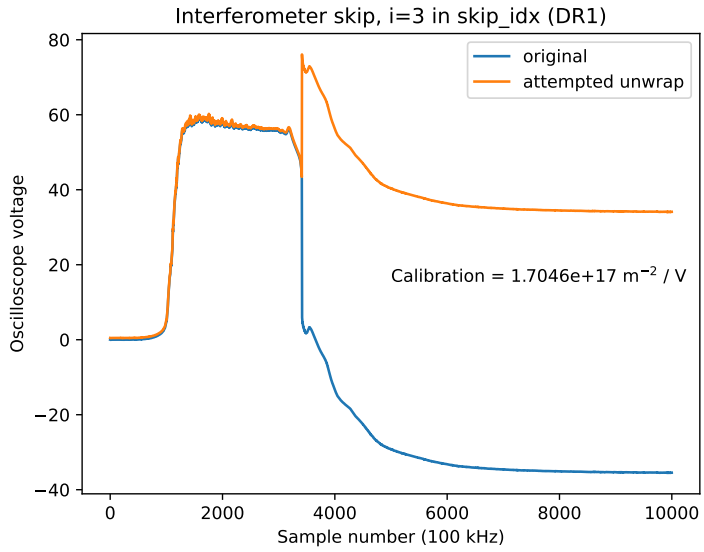


Figure 4.4: An example of the interferometer skip (blue) and the attempted unwrap (orange).

low-density plasmas where the photon counts are low. An example of this process can be seen in fig. 4.5.

## 4.5 Data bias

Data bias and imbalance in the training set can be exacerbated by the train-test split. For the nominal test set, 8 out of the 67 dataruns were hand picked for diversity and held out from the training set. Leaving out entire dataruns – not just shots – is important in order to estimate model performance on new, unseen discharges in new configurations. Four dataruns from each run set were left out: from DR1 08, 15, 23, and 33, were held out and from DR2, 02, 10, 19, and 31. As will be demonstrated in chapter 5, this test set appears to characterize the model performance on held out data fairly well.

The dataset predominantly contains gas puff durations of 38 ms. Only six runs in the training set have gas puff durations less than 38 ms: three have 5 ms and three have 10 ms, each having mirror ratios 1, 3, and 6 but otherwise identical configurations in an attempt to see mirror-related interchange instabilities in higher-temperature, lower-collisionality regimes. The 20 ms gas puff

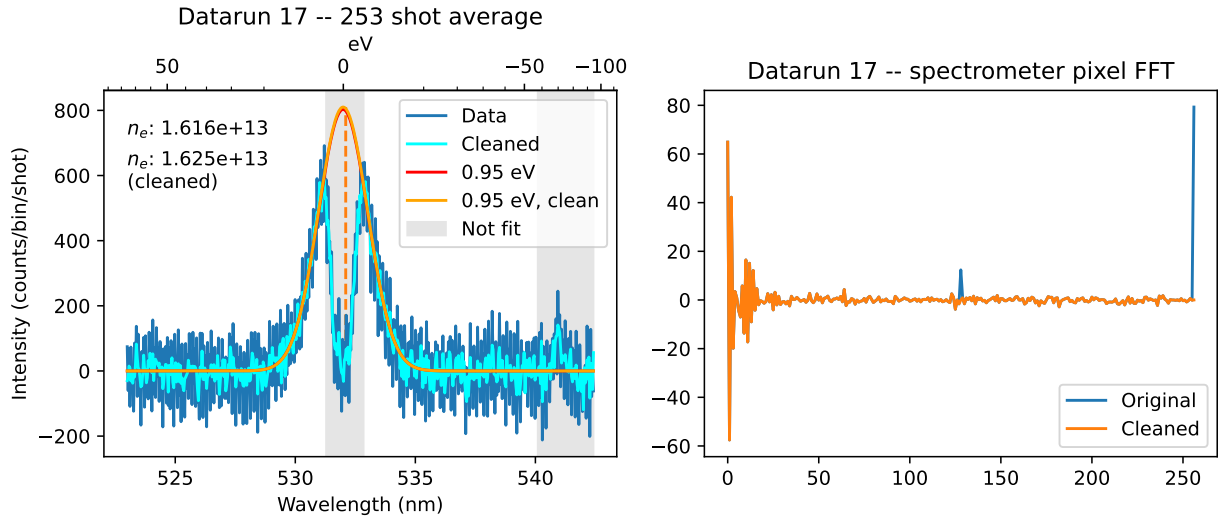


Figure 4.5: The Gaussian fit to the Thomson scattering spectrum before and after crude FFT filtering. The shaded gray region is excluded from the fitting process because they contain the region of the notch filter (the region about 532 nm) and a He-II (ion) line ( $\approx 541$  nm).

duration case is in the test set (DR2 31). This sampling bias towards the 38 ms gas puff duration suggests poor model performance is to be expected in shorter gas puff regimes. The top gas puff valve was operational for only the first nine runs of DR2.

Despite the best efforts to randomize the machine configuration, imbalance in the dataset will be present because of the relatively small amount of samples for the given actuator space. The distribution of  $I_{\text{sat}}$  signals, averaged from 10 to 20 ms, can be seen in Fig. 4.6. The  $I_{\text{sat}}$  distribution is clearly different for DR1 and DR2, with DR1 having a much flatter distribution. These distributions imply that if the model is constrained to sample from DR2 via the run set flag, then the model is expected to predict a lower  $I_{\text{sat}}$  value in general. When predicting from the model in general, performance will likely be worse for  $I_{\text{sat}}$  values  $\gtrsim 11 \text{ mA/mm}^2$ . The time-averaged  $I_{\text{sat}}$  distribution is dissimilar between DR1 and DR2: DR1 appears to have a more uniform distribution. Combining the two datasets results in many  $I_{\text{sat}}$  examples less than  $2 \text{ mA/mm}^2$  and a sharp decrease in number of examples above  $10 \text{ mA/mm}^2$ . Thus, we expect the model to perform better for smaller  $I_{\text{sat}}$  values

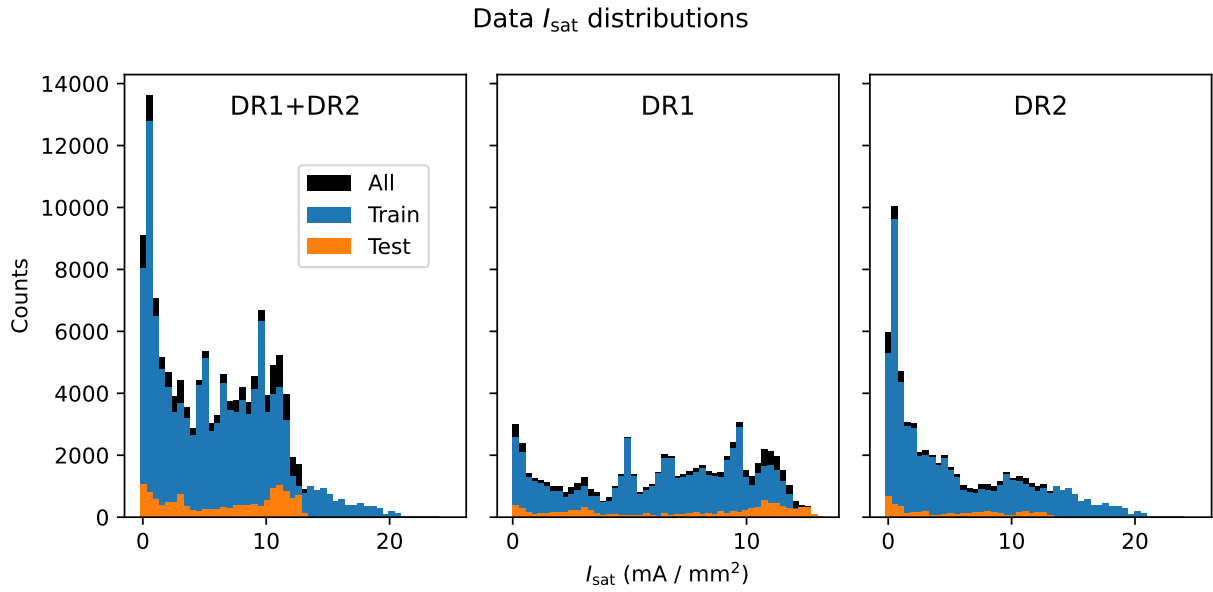


Figure 4.6: Distribution of  $I_{\text{sat}}$  signals when averaged from 10 to 20 ms. DR1 appears to have a more uniform distribution than DR2 does. Combining the two datasets results in many  $I_{\text{sat}}$  examples near 0 mA/mm<sup>2</sup> and a sharp decrease in number of examples above 10 mA/mm<sup>2</sup>. From these histograms we expect or model to be biased towards fitting lower  $I_{\text{sat}}$  values better, and to perform badly in cases with very high  $I_{\text{sat}}$  values.

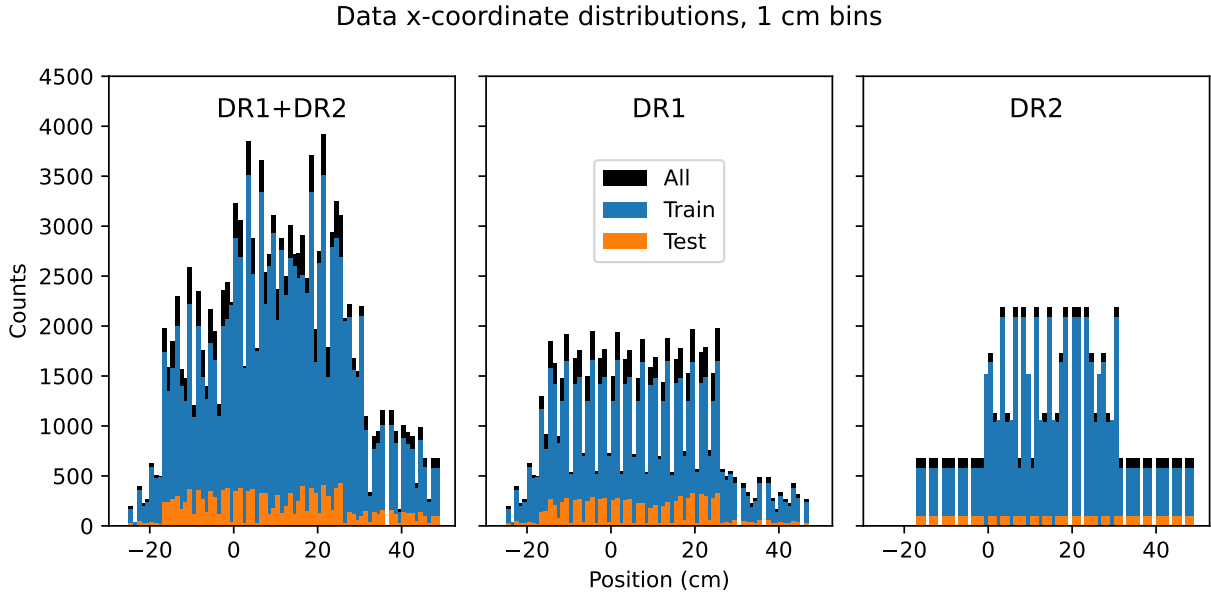


Figure 4.7: Distribution of the x-coordinate in the profiles. The increase in data points between roughly  $x \approx 0$  to  $30$  cm is from planes instead of lines. Based on this distribution, the performance of the model is expected to be biased towards this central area.

than larger ones.

The mix of different probe movements also leads to some imbalance in the dataset. The distribution of probe positions can be seen in fig. 4.7. Notably, samples appear to drop off beyond  $+25$  cm and  $-15$  cm. Measurements over an x-y plane, constituting  $\approx 64\%$  of all shots, are predominantly acquired overnight for maximal machine utilization. These longer dataruns lead to particular machine configurations being overrepresented in the dataset.

The distribution of the selected machine settings for all the dataruns is enumerated in Table 4.1. Despite the randomization of the settings of 44 dataruns, the distribution is often uneven. The remaining 23 non-random dataruns also contribute to the imbalance. For example, a source field of 1 kG and discharge voltage of 112 show up disproportionately in the dataset because data were collected at those settings while other equipment was being adjusted or calibrated.

Table 4.1: Data breakdown by class and dataset (percent)

B source (G)				B mirror (G)				B midplane (G)			
	Train	Test	All		Train	Test	All		Train	Test	All
500	4.77	0	4.29	250	4.30	8.41	4.72	250	8.25	21.01	9.55
750	3.34	12.61	4.29	500	30.49	8.41	28.23	500	43.80	8.41	40.19
1000	43.13	78.99	46.78	750	6.68	16.81	7.72	750	6.62	52.19	11.27
1250	12.59	0	11.30	1000	28.85	57.97	31.82	1000	26.36	5.78	24.26
1500	19.23	0	17.27	1250	3.34	4.20	3.43	1250	9.24	0	8.30
1750	1.91	0	1.71	1500	26.34	4.20	24.08	1500	5.73	12.61	6.43
2000	15.03	8.41	14.35								

Gas puff voltage (V)				Discharge voltage (V)				Axial probe position (cm)				
	70	12.11	16.81	70	12.22	8.41	11.83	639	12.48	8.41	12.06	
	75	6.68	0	6.00	80	5.25	0	4.72	828	17.07	36.28	19.03
	80	11.46	8.41	11.15	90	2.86	8.41	3.43	859	12.48	8.41	12.06
	82	41.49	57.97	43.17	100	3.34	8.41	3.86	895	33.01	30.10	32.71
	85	14.13	0	12.69	110	8.77	0	7.87	1017	12.48	8.41	12.06
	90	14.13	16.81	14.40	112	20.62	0	18.52	1145	12.48	8.41	12.06
					120	3.82	8.41	4.29				
					130	0.95	0	0.86				
					140	2.86	8.41	3.43				
					150	39.30	57.97	41.20				

Gas puff duration (ms)				Vertical probe position (cm)			
	38	94.27	91.59	38	≈ 0	36.26	46.08
	< 38	5.73	8.41	6.00	≠ 0	63.74	53.92

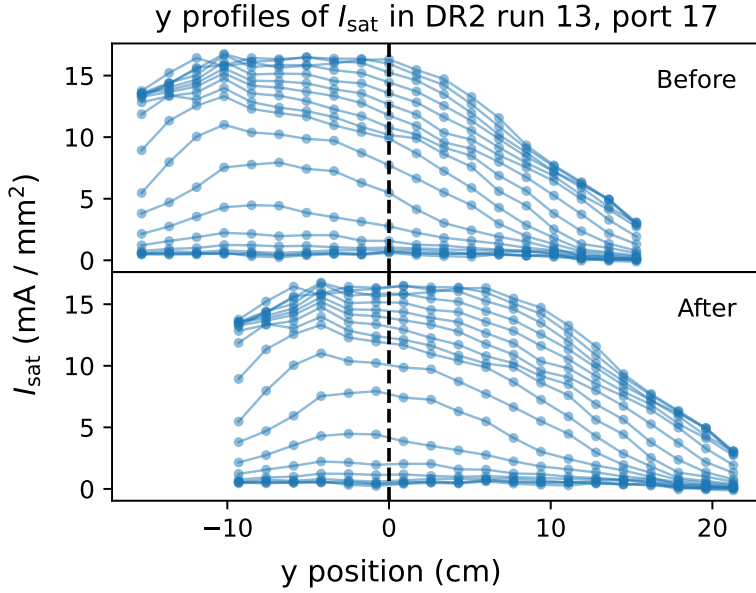


Figure 4.8: An example of the y-axis profile before and after shifting the y-coordinate. The “before” plot (top) is obviously asymmetrical about  $y=0$ . The shift needed to center was eyeballed from the plot. Each line represents a different x position, from closest to the core (upper lines) to the edge (lower lines).

## 4.6 Azimuthal asymmetry of probe data

Examining the data, it appears that the y coordinate is not centered properly, possibly because the telescope used to align the probes is set incorrectly. Using profiles from planar data (see the “before” plot in fig. 4.8), the y-coordinate was adjusted. The probes in DR1 were adjusted upwards by +2 cm. For DR2, the y-coordinate was adjusted separately for each probe. Port 17 was adjusted 6 cm up, port 21 was adjusted 4 cm up, port 26 was adjusted 4.5 cm up, and port 33 was adjusted 3.35 cm up. This degree of error is consistent with the centering scope crosshairs having some angle error, creating a larger absolute y-axis error closer to the cathode. An example of this y-axis error and the profile after shifting the coordinates can be seen in fig. 4.8. It is likely that this y-axis offset applies to other probes in the plasma, not just probes with  $I_{\text{sat}}$  tips.

## 4.7 Applying and improving the dataset

The two chapters following this detail machine learning studies utilizing this dataset, though only using a subset of the diagnostics available. Much room remains for ML-based analysis of the dataset, such as including additional diagnostics, in-situ diagnostic calibration (e.g.,  $I_{\text{sat}}$  or Thomson scattering). Even though the diversity of the dataset is relatively high, many imbalances in machine inputs remain. More data with additional (pseudo-)random samples from broader parameter ranges would be very beneficial in improving downstream ML tasks. Pushing the boundaries of the machine parameters could also lead to discovery and exploitation of new operational modes of the LAPD which could prove beneficial.

## CHAPTER 5

# Optimizing mirror configurations in the LAPD using machine learning

This study demonstrates the efficacy of machine learning (ML)-based trend inference using data from the Large Plasma Device (LAPD). Neural network (NN) ensembles with uncertainty quantification are trained to predict time-averaged ion saturation current ( $I_{\text{sat}}$  — proportional to density and the square root of electron temperature) at any position within the dataset domain. Model-inferred trends, such as the effects of introducing mirrors or changing the discharge voltage, are consistent with current understanding. In addition, axial variation is optimized via comprehensive search over  $I_{\text{sat}}$  predictions. Experimental validation of these optimized machine parameters demonstrate qualitative agreement, with quantitative differences attributable to Langmuir probe variation and cathode conditions. This investigation demonstrates, using ML techniques, a new way of extracting insight from experiments and novel optimization of plasmas. The code and data used in this study are made freely available.

The primary goals of this work are to provide an example of a solid, validated machine learning study and demonstrate how ML can be useful in understanding operating plasma devices.

### 5.1 Introduction

Understanding and controlling plasma behavior in fusion devices is necessary for developing efficient fusion reactors for energy production. Because of the complex, high-dimensional parameter space, traditional experimental approaches are often time-consuming and require careful planning.

This work explores how machine learning (ML) techniques can accelerate this understanding by studying the effect of machine parameters in a basic magnetized plasma device. Trend inference is this process of relationship discovery. While ML methods, particularly neural networks (NNs), have become increasingly prevalent in fusion research for control and stabilization, their application to systematic trend discovery remains largely unexplored.

Many studies have used ML for profile prediction on a variety of tokamaks, particularly for real-time prediction and control. For example, NNs were used to predict electron density, temperature, and other quantities in DIII-D [ACK21], and reservoir NNs have demonstrated the ability to quickly adapt to new scenarios or devices [JAC22]. Temporal evolution of parameters has been successfully modeled using recurrent neural networks (RNNs)[CCA24] for multiple devices, including the EAST[WYP22] and KSTAR tokamaks[SNK21, SNK22]. These predictions enabled training of a reinforcement learning-based controller[SNK21, SNK22]. In addition, a decision tree-based controller was trained to maximize  $\beta_N$  while avoiding tearing instabilities[FEE20] on DIII-D. Electron temperature profiles have also been predicted using dense NNs on the J-TEXT tokamak [DLD21].

A parallel focus has been on instability prediction and mitigation in tokamaks, particularly of disruptions. Notable achievements in disruption prediction include RNN-based disruption prediction [KST19] and random forest approaches[RME19], with a comprehensive review available by Vega et al [VMD22]. Recent work has extended to active control, such as the mitigation of tearing instabilities in DIII-D using reinforcement learning [SKJ24].

While ML has proven effective for prediction and control tasks, inferring trends using data-driven methods has been relatively uncommon. Notable exceptions include finding scaling laws on the JET tokamak[MPL20] via classical ML techniques and the development of the Maris density limit[MRP24] which outperforms other common scalings (including the Greenwald density limit) in predictive capability.

The use of machine learning and Bayesian inference in fusion research has been recently reviewed by Pavone et al.[PMK23]

Outside of magnetized plasmas, the laser plasma community has embraced ML techniques for various applications, enumerated in a review by Dopp et al.[DEH23]. Data-driven plasma science in general has been reviewed by Anirudh et al.[AAA23] Notably, a similar quasi-random method (Sobol sequences) was used to collect a spectroscopy dataset on a plasma processing device over diverse machine settings [DFH23]. This process is similar to what is performed in our work here, but a generative variational autoencoder was instead trained to be used as an empirical surrogate model.

This work advances data-driven methods in plasma physics by taking these methods one step further: instead of learning a model for particular task (e.g., disruption prediction or profile prediction), we infer learned trends directly from the model itself.

The goal of this study is to develop a data-driven model that can provide insight into the effect of machine parameters on plasmas produced in Large Plasma Device (LAPD) in lieu of a theoretical model. In contrast with tokamaks and other fusion devices, the LAPD is particularly well-suited for ML data collection because of its flexibility and high repetition rate. We demonstrate the capability to infer trends in a particular diagnostic signal, the time-averaged ion saturation current ( $I_{\text{sat}}$ ), for any mirror (or anti-mirror) field geometry in a variety of machine configurations. Langmuir probes are commonly used to measure density, temperature, and potential in virtually all plasma devices in low-temperature (less than 10s of an eV) regimes. The  $I_{\text{sat}}$  signal in particular is almost always used in the LAPD for calculating local plasma density.

This study performs two firsts in magnetized plasma research: using NNs to directly infer trends and collecting data efficiently with partially-randomized machine parameters. We also demonstrate optimizing LAPD plasmas given any cost function by minimizing axial variation in  $I_{\text{sat}}$ . This global optimization is only possible using ML techniques. This work demonstrates the usefulness of a pure ML approach to modeling device operation and shows how this model can be exploited. We encourage existing ML projects and experiments to consider this approach if possible. Acquiring sufficiently diverse datasets may require assuming some risk because diverse data, such as discharges from randomly sampled machine settings, may not be amenable to conventional

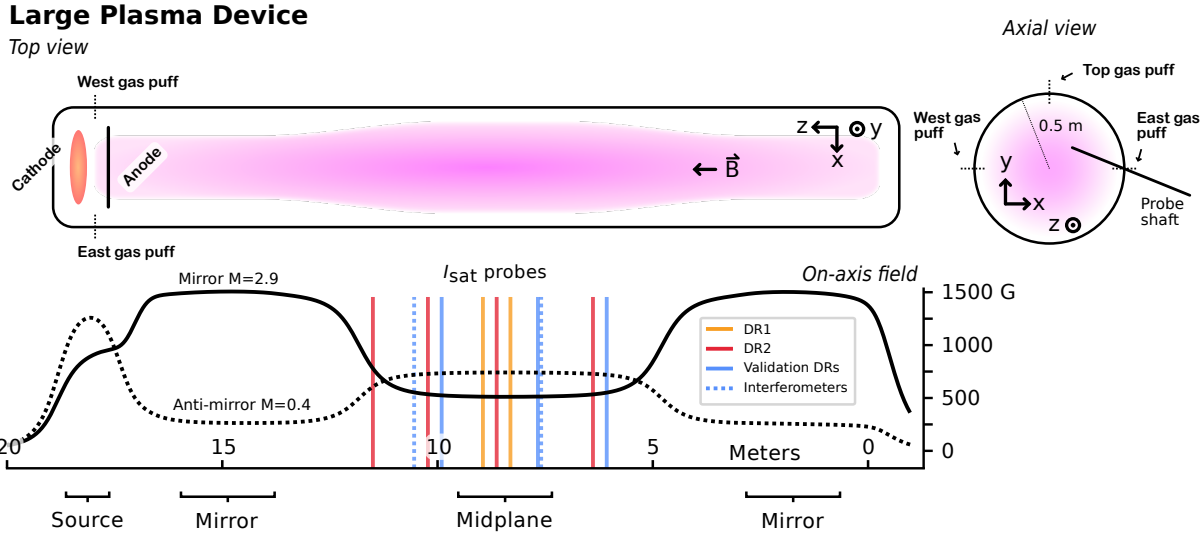


Figure 5.1: A cartoon of the Large Plasma Device, the coordinate system used, examples of a mirror and anti-mirror magnetic field configuration, and probe locations used in this study. The source, mirror, and midplane regions are labeled; the three fields were programmed independently.

analysis techniques.

All the processed data used for training the models in this study are freely available[Tra25] (see section 5.11). Other devices have also made data publicly available. Namely, data for H-mode confinement scaling has been available since 2008[RWB08], and more recently some MAST[JKC24] and all LHD[lhd] data are now publicly available.

## 5.2 Processing of $I_{\text{sat}}$ signals

The ion saturation current, denoted as  $I_{\text{sat}}$ , is obtained by applying a sufficiently negatively bias to a Langmuir probe to ensure the exclusive collection of ions. This collected current is proportional to  $S n_e \sqrt{T_e}$ , where  $n_e$  and  $T_e$  are the electron density and temperature, and  $S$  is the effective probe collection area. To account for differences in probe tip geometry, the  $I_{\text{sat}}$  values are normalized to area. Under typical conditions, an  $I_{\text{sat}}$  value of 1 mA/mm<sup>2</sup> corresponds to  $n_e \approx 1-2 \times 10^{12} \text{ cm}^{-3}$  for

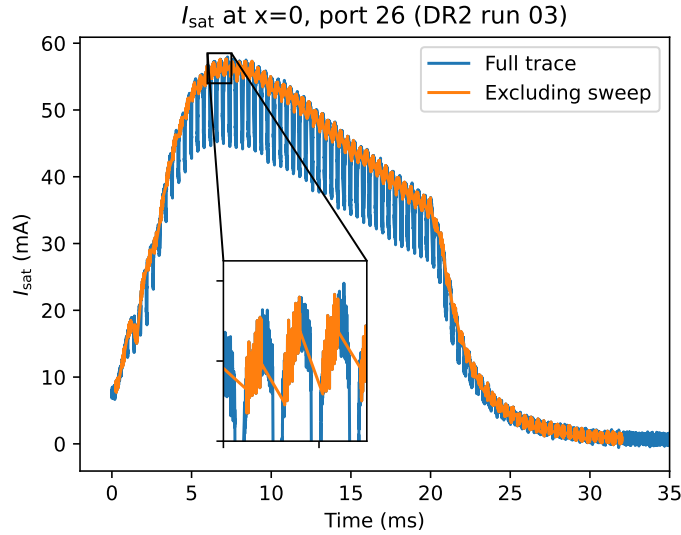


Figure 5.2:  $I_{\text{sat}}$  traces from the swept probe (port 26) from DR2 datarun 03, shot 1 of 6. The orange curve is excluding times when a sweep is active on an opposing tip.

a  $T_e$  from 4 to 1 eV.

$I_{\text{sat}}$  measurements were averaged over 10 to 20 ms to exclude plasma ramp-up and fluctuations. Example  $I_{\text{sat}}$  probe data can be seen in fig. 5.3 along side gas puff timings. For the probe tip that was on the same shaft as the swept probe (in DR2), the signal was instead averaged over when the bias voltage on the swept tip was held constant at the lowest value. A 40  $\mu\text{s}$  (250 sample) buffer was used after the sweep was turned off to minimize the impact of transient conditions. A comparison of the full trace and the trace with the swept portion excluded can be seen in fig. 5.2. Notably, the measured  $I_{\text{sat}}$  value does not attain a steady state before the discharge shuts off.

Profile evolution is not studied to minimize computational requirements.  $I_{\text{sat}}$  characteristics vary significantly between axial ( $z$ ) position machine parameters. For  $I_{\text{sat}}$  measurements on the same probe as a Langmuir sweep (DR2 port 26,  $z=863$  cm), the averaging process excludes the sweep period with an additional 40  $\mu\text{s}$  buffer.

While  $I_{\text{sat}}$  exhibits a small degree of shot-to-shot variation, the present model only learns the expected value, leaving distributional modeling to future generative approaches. An example of

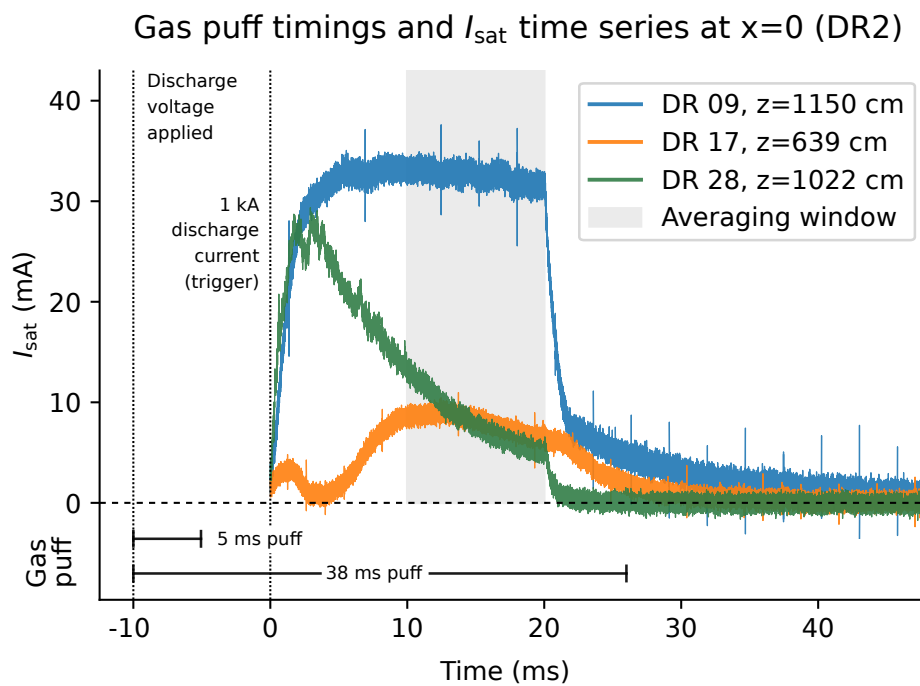


Figure 5.3: Gas puff timings and example  $I_{\text{sat}}$  time series at three different z-axis locations from three different dataruns. Note that some discharges do not achieve steady state in  $I_{\text{sat}}$ .

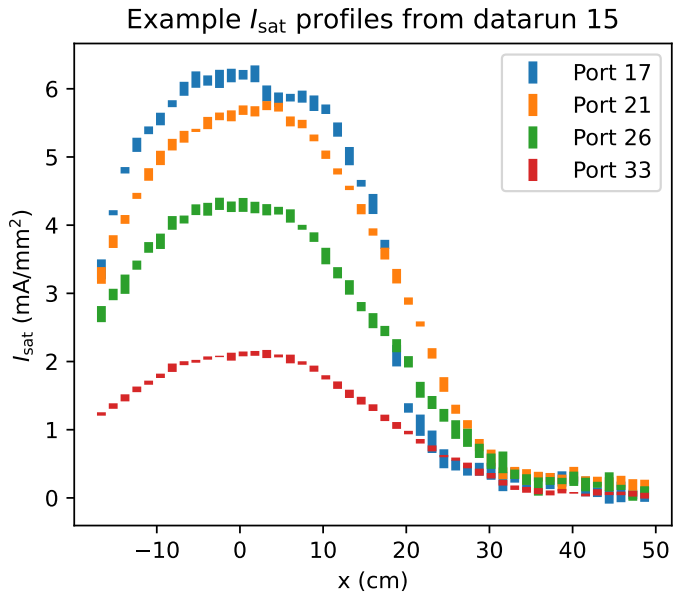


Figure 5.4: Examples of  $I_{\text{sat}}$  profiles from DR2 run 15. The bars represent the minimum and maximum of the six  $I_{\text{sat}}$  measurements taken at that position.

these  $I_{\text{sat}}$  profiles and the six-shot variance can be seen in fig. 5.4.

## 5.3 Model development and training

### 5.3.1 Model inputs

Neural network inputs comprise 12 variables: source field, mirror field, midplane field, gas puff voltage, discharge voltage, gas puff duration, probe coordinates ( $x, y, z$ ), probe rotation, run set identifier, and top gas puff flag. These variables can be interpreted as six control parameters, four probe coordinates, and two flags. These inputs are mean-centered and normalized to the peak-to-peak value with no outliers in the dataset. The baseline models trained in section 5.3.4 did not contain the run set identifier or top gas puff flag.

### 5.3.2 Training details

For initial experiments in training the model, a mean-squared error (MSE) loss is used:

$$\mathcal{L}_{\text{MSE}} = \frac{1}{m} \sum_{i=1}^m (f(x_i) - y_i)^2 \quad (5.1)$$

where  $x_i$  represents the input vector for the  $i$ th example,  $y_i$  the target measurement,  $m$  the batch size, and  $f$  the NN. During training, overfitting was assessed via the validation set MSE with a traditional 80-20 train-validation random split. Unless stated otherwise, a dense neural network, 4 hidden layers deep and 256 units wide (201,218 parameters for  $\beta$ -NLL loss, 200,962 parameters for MSE loss), was trained with AdamW using a learning rate of  $3 \times 10^{-4}$ . Leaky ReLU activations (the nonlinearities in the NN) and adaptive gradient clipping[SWP20] (cutting gradients norms above the 90th percentile of recent norms) were used to mitigate vanishing gradients and mitigate exploding gradients, respectively. The models were evaluated after training concluded at 500 epochs.

### 5.3.3 Validating the training pipeline

ML training processes are relatively simple but bugs, particularly in the data pipeline, can be insidious and can affect final model performance even though training looks fine. Here we validate the data pipeline (which should be performed in every ML study) to verify that the model is training and expected and that there is no accidental data leakage between the train and test sets. Andrej Karpathy’s advice for training neural networks [Kar19] was used as a template for verifying the training procedure used in this project. The data fed into the model immediately before the forward pass (and subsequent backpropagation) was stored and verified: the data are correctly randomly shuffled in each batch. Each epoch contains the same random shot order. To validate the data pipeline, a simple dense model (4 layers, 512 wide with one output; 794113 parameters, tanh activations) was trained. The model is also overfit on a single batch (128 examples) of training data to make sure that training progresses as expected. A deep double descent is observed as expected [NKB19, SKR23]. Training on a batch of 8 examples reaches  $\approx 0$  training loss after 50 steps. Plots of the train and validation losses can be seen in Fig. 5.5.

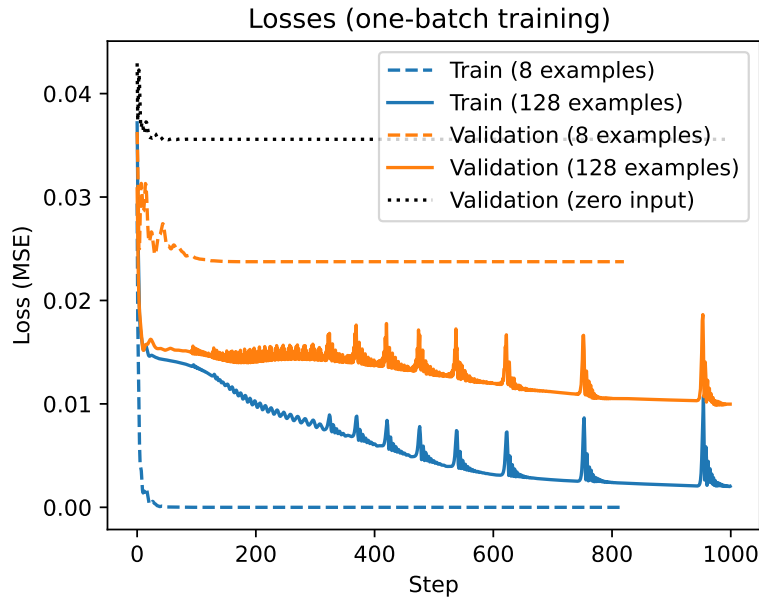


Figure 5.5: Training and validation losses when overfitting the model. A deep double descent in the validation losses is observed when fitting a single batch of 128 examples. The 8-example batch hits near-zero loss after 50 steps. This process verifies our training process is functioning as expected. The spikes are from exploding gradients which can be mitigated by clipping the gradients. A model trained on blank data is also shown as the black dotted line.

Multiple models were trained with varying depths and widths to verify that training loss decreases with increased model capacity. Doubling the layer width from 512 to 1024 moderately decreases the training loss; doubling the depth of the network from 4 to 8 layers has a larger impact. Increasing the width further to 2048 and depth to 12 layers has a dramatic impact on training loss, so this model and dataset are behaving nominally. The model pipeline is training and performing as expected, so we proceed.

#### 5.3.4 Baselines for mean-squared error

A model was first trained with zeroed-out inputs as a baseline and to validate the data pipeline. This model effectively has only a single, learnable bias parameter at the input. This process yields a

validation loss (simply MSE in this case) of 0.036.

A linear model obviously cannot fit the dataset (see the nonlinear shape of the profiles in fig. 5.4). However, a simple (and mostly linear) model can provide a performance baseline to help spot bugs when training more complex models. Since the x- and y- profiles have an approximate tanh shape, a feature is added at the linear model input stage for the x and y coordinates:  $x_{\text{tanh}} = c \cdot \tanh((|x + s| \cdot a + b))$  where  $s, a, b, c$  are trainable parameters (independent for each coordinate;  $c$  is superfluous). This function was chosen to give the linear model the capability of expressing tanh-like curves. The performance of the linear model on DR2 data, with and without the tanh features, can be seen in fig. 5.6. This baseline linear-like model reaches a training and validation loss of around 0.011, with the RMSE =  $\sqrt{\text{loss}} \sim 0.1$ . The linear-only model is marginally worse with losses at around 0.014.

This feature engineering-like approach can continue. For example, the width of the profile is largely controlled by magnetic field configuration of the device, particularly by  $\sqrt{B_{\text{midplane}}/B_{\text{source}}}$ . This behavior can be added to this model, either as a new feature or as a custom relationship in the model. Note that, as seen in fig. 5.6, the width of the profile also depends on the axial coordinate. Combined with other coordinates and actuators, like discharge voltage and gas pressure, the number of possible features or function space grows combinatorially, making this custom fitting process difficult and tedious to design and test by hand. The obvious solution would be to use symbolic regression or fitting to a function library which may be ideal methods if simple profile prediction were the final goal. However, we are ultimately interested inferring trends in a much more complex input space where neural networks are more flexible and accurate. If NNs do face generalization issues, symbolic regression or a SINDy-like approach can be used instead, albeit with limited applications. Symbolic methods are appealing because the fits are simple. However, even though a simple equation may fit the data well, it does not necessarily provide insight or relate to the underlying physics; using a freeform fitting function like a neural network is more appropriate in this use case.

A summary of these baselines is seen at the top of Table 5.1.

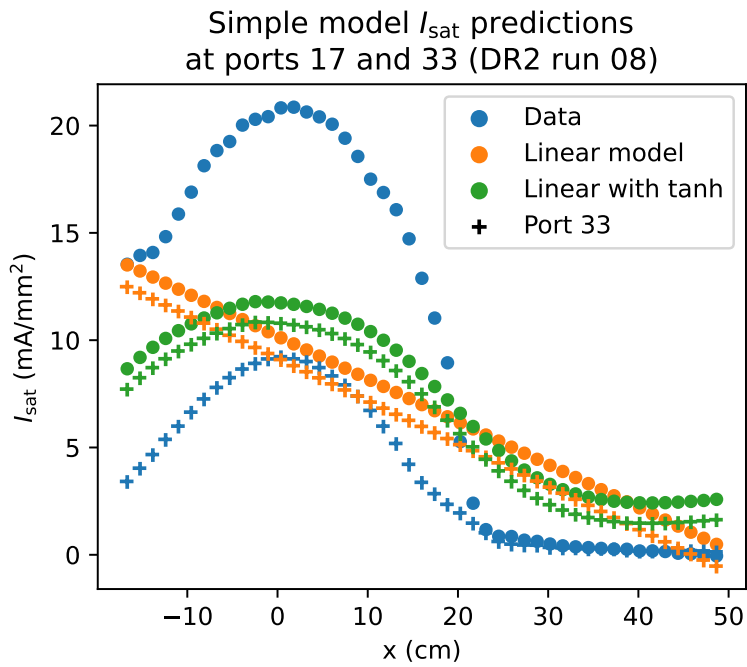


Figure 5.6:  $I_{\text{sat}}$  profiles and predictions for ports 17 and 33 based on inputs from DR2 run 08 using a liner and linear-with-tanh models. DR2 run 08 is in the training set. The “data” points are averaged over six shots. Run 08 was chosen for its representative performance; ports 17 and 33 were chosen to demonstrate the maximal axial variation (across 511 cm). These models fail to describe the data accurately.

Table 5.1: Summary of test set losses for different training data and ensembles

Model	MSE $\times 10^{-3}$
Zeroed-input	36 (validation)
Linear model	14 (validation)
Linear with tanh features	11 (validation)
9 dataruns	7.0
19 dataruns	6.9
29 dataruns	4.2
39 dataruns	4.1
49 dataruns	3.4
DR1 only	6.4
DR2 only	5.4
Full set, large model	2.8
Full set average	$3.6 \pm 0.56$
Full set ensemble	$2.9 \pm 1.1$
“Run set” flag average	$2.1 \pm 0.15$
“Run set” flag ensemble	$1.9 \pm 0.64$
“Top gas puff” flag	1.8

### 5.3.5 Effects of training set and model sizes

To study the effects of reduced diversity, the number of unique dataruns in the training set was systematically reduced while evaluating on a fixed test set. The test set loss monotonically increased with this decrease in datarun count. Part of this decrease may be caused by a simple reduction in training set size. In addition, models were individually trained and evaluated on DR1 only or DR2 only. When evaluated on the left-out run set, the test set losses were high, near or above the zero-input baseline of  $3.6 \times 10^{-2}$ . This result suggests that both run sets contain significant information missing in the other, and training on both provides beneficial information on the structure of the  $I_{\text{sat}}$  measurement despite different probe calibrations and cathode state.

A larger model, consisting of a 12-deep 2048-wide dense network, was trained on the full training dataset, evaluated at 30 epochs. This larger model yielded a test MSE of  $2.8 \times 10^{-3}$ , indicating that these NNs are behaving as expected. Longer training or larger models may yield better test set results, but will likely not come close to the training and validation losses which are on the order of  $10^{-5}$ . Combined models with differing initializations (an ensemble), were trained to measure the MSE variance over model parameters which was about 16%. When the  $I_{\text{sat}}$  predictions were averaged, the test set MSE was  $2.9 \pm 1.1 \times 10^{-3}$ , achieving the best performance for that model size. These test set losses are also seen in Table 5.1.

### 5.3.6 Improving performance with machine state flags

Data from DR1 and DR2 were collected 14 months apart leading to differing machine states. In DR1, only one turbo pump was operating leading to much higher neutral pressures than in the DR2 run set. A new parameter (mean-centered and scaled) was added to the inputs to distinguish between these two run sets. All the predictions in this study use the DR2 run set flag (a value of 1.0) because turning off the turbopumps is not a commonly desired mode of operating the LAPD. The inclusion of this parameter also provides the model the ability to distinguish between the probe calibration differences between DR1 and DR2. An ensemble prediction with this run set flag brings the test set

MSE down to  $1.9 \times 10^{-3}$ .

A flag indicating when the top gas puff valve was enabled in DR2 was also added to all training data, allowing the model to further distinguish between different fueling cases. The addition of this flag incrementally improved test set MSE to  $1.8 \times 10^{-3}$ . The effect on MSE on the inclusion of these new parameters is compared to the performance of other models in Table 5.1.

### 5.3.7 Learning rate scheduling

Modifying the learning rate over time (scheduling) is known to improve model learning. The following schedules were compared: constant learning rate ( $\gamma = 3 \times 10^{-4}$ ),  $\gamma \propto \text{epoch}^{-1}$ ,  $\gamma \propto \exp(-\text{epoch})$ , and  $\gamma \propto \text{epoch}^{-1/2}$ . The epoch is the training step divided by the number of batches in one epoch, so “epoch” in this case takes on a floating-point value.  $\gamma \propto \text{epoch}^{-1}$  appears to give the best test set loss by a test MSE difference of  $1 \times 10^{-4}$ , and any schedule beats a constant learning rate by a difference of  $2 - 4 \times 10^{-4}$ .

## 5.4 Uncertainty quantification

### 5.4.1 $\beta$ -NLL loss

Instead of predicting a single point, the model can predict a mean  $\mu$  and variance  $\sigma^2$  using the negative-log likelihood (NLL) loss [NW94, LPB17] by assuming a Gaussian likelihood. An adaptive scaling factor  $\text{StopGrad}(\sigma_i^{2\beta})$  is introduced that can be interpreted as an interpolation between an MSE loss and Gaussian NLL loss, yielding the  $\beta$ -NLL loss:

$$\mathcal{L}_{\beta-\text{NLL}} = \frac{1}{2} \left( \log \sigma_i^2(\mathbf{x}_n) + \frac{(\mu_i(\mathbf{x}_n) - y_n)^2}{\sigma_i^2(\mathbf{x}_n)} \right) \text{StopGrad}(\sigma_i^{2\beta}) \quad (5.2)$$

for example  $n$  and model  $i$ , with an implicit expectation over training examples.  $\beta = 0$  yields the original Gaussian NLL loss function and  $\beta = 1$  yields the MSE loss function. This factor improves

MSE performance by scaling via an effective learning rate for each example (which necessitates the StopGrad operation) [STA22], and improves both aleatoric and epistemic uncertainty quantification [VS22].  $\beta = 0.5$  was used by default in this study. This  $\beta$ -NLL loss function also improved training stability.

This NLL-like loss assumes the prediction – the likelihood of  $y$  given input  $\mathbf{x}$ :  $p(y|\mathbf{x})$  – follows a Gaussian distribution. Treating each prediction as an independent random variable (considering each model in the ensemble is sampled from some weight distribution  $\theta \sim p(\theta|\mathbf{x}, y)$ ) and finding the mean of the random variables yields a normal distribution with mean  $\mu_*(\mathbf{x}) = \langle \mu_i(\mathbf{x}) \rangle$  and variance  $\sigma_*^2 = \langle \sigma_i^2(\mathbf{x}) + \mu_i^2(\mathbf{x}) \rangle - \mu_*^2(\mathbf{x})$  where  $\langle \rangle$  indicates an average over the ensemble.

The loss function for one of the NNs in an ensemble is seen in fig. 5.7. The MSE decreases monotonically for the training and validation set, but does not for the test set. The loss function can no longer be interpreted as a log-likelihood because of the effective per-example learning rate set by the  $\beta$  term in the loss (eq. 5.2). Note that early stopping (at around 8 epochs) would improve the test set loss, but the MSE would still be several factors higher than after 500 epochs. Early stopping was not explored in this study.

The ensemble predictive uncertainty can be broken down into the aleatoric and epistemic components [VS22]: the aleatoric uncertainty is  $\langle \sigma_i^2(\mathbf{x}) \rangle$  and the epistemic uncertainty is  $\langle \mu_i^2(\mathbf{x}) \rangle - \mu_*^2(\mathbf{x}) = \text{Var}[\mu_i(\mathbf{x})]$ . The intuition behind these uncertainties is that the random fluctuations in the recorded data are captured in the variance of a single network,  $\sigma_i^2$ . If the choice of model parameters were significant, we would expect the predicted mean for a single model,  $\mu_i$ , to fluctuate as captured by  $\text{Var}[\mu_i(\mathbf{x})]$ .

### 5.4.2 Cross-validation MSE

For cross-validation, multiple train-test set pairs were created. Test set 0 comprises deliberately chosen dataruns to encompass a diverse set of machine settings and probe movements. The other six datasets were compiled with randomly chosen dataruns (without replacement) while keeping

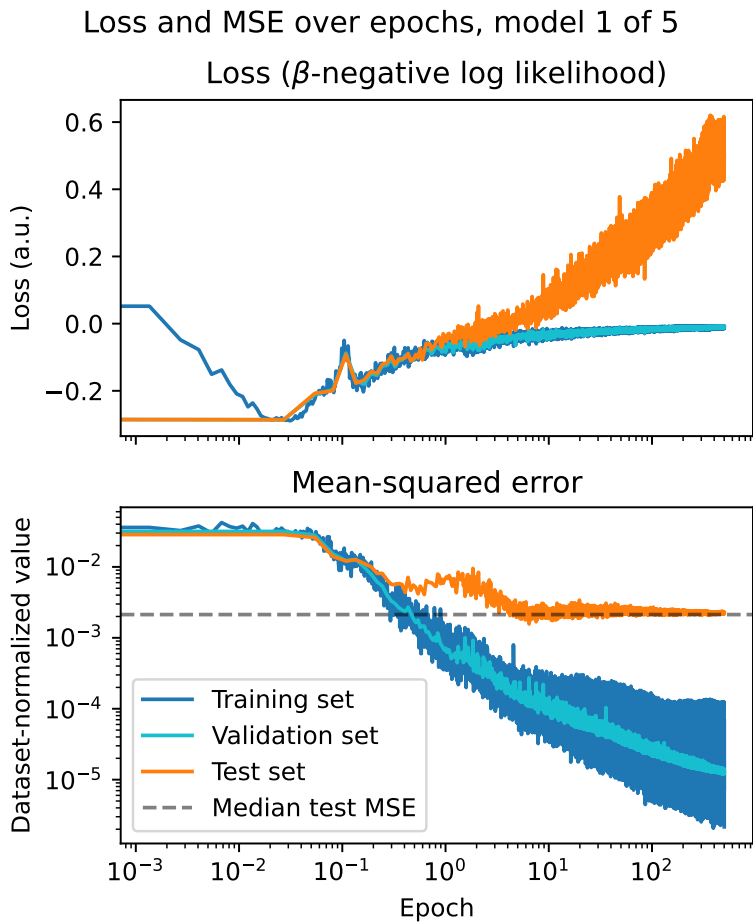


Figure 5.7: The loss and MSE for the training, validation, and test sets over the entire training duration of 500 epochs. The inclusion of the  $\beta$  term in the loss function – interpreted as a per-example learning rate – makes the loss function no longer interpretable in simple terms. The mean-squared error benefits from longer training for all sets.

the number of dataruns from DR1 and DR2 equal. Seven model ensembles (5 NNs per ensemble – 35 NNs total) were trained to evaluate the effect of test set choice on model MSE. The test set MSE performance can be seen in fig. 5.8, and the training MSE performance in fig. 5.9. The median ensemble test set MSE for these seven sets was  $2.13 \times 10^{-3}$  with a mean of  $3.6 \times 10^{-3}$ . The handpicked dataset had an ensemble test set MSE of  $1.85 \times 10^{-3}$ , indicating that the choice of dataruns was adequately representative. This median MSE will be used to estimate model prediction error in addition to uncertainty quantification. This cross-validation also provides an error estimate if the models were to be trained on *all* dataruns. Ensembles always out-performed the average error of single-model predictions.

All validation set MSEs fall between 1 and  $6 \times 10^{-5}$ , with the average training MSE falling within that range as well. These MSEs indicate that the model is able to fit the training data to a high degree of accuracy regardless of which dataruns are held out. The loss and MSE curves over training epochs can be seen in the appendix in fig. 5.7.

### 5.4.3 Model calibration via weight decay

The predicted uncertainty may not provide an accurate range of  $I_{\text{sat}}$  values when compared to the measured value. Calibrating the model means changing the predicted uncertainty range so that the measured values fall within that range according to some distribution, such as a Gaussian in this case. One of the ways assessing this calibration is by the z-score of predictions, where  $z_n = (x_n - \mu_n) / \sigma_n(x_n)$  for example  $x_n$ , predicted mean  $\mu_n$ , and standard deviation  $\sigma_n$ . Perfect model calibration would lead to identical z-score distribution  $\mathcal{N}(\mu = 0, \sigma = 1)$  for the training and test sets. When evaluated on the training set, the distribution should be a Gaussian with a standard deviation of 1. The z-score distributions for the train and test sets with a model weight decay of 0 can be seen in fig. 5.10.

Increased weight decay can lead to better model calibration [GPS17]. Weight decay penalizes large parameter values by adding the L2 norm of model weights to the loss. Model ensembles were

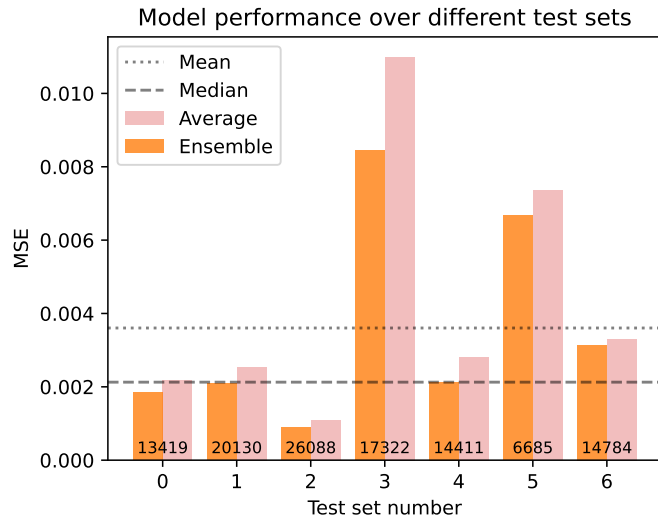


Figure 5.8: Model performance as measured by MSE over test sets with different dataruns. Test set 0 is the hand-picked dataset, and the rest were randomly compiled without replacement (though separate for DR1 and DR2). The number at the bottom of the bar chart is the number of shots in the testing set. The median test set performance is very close to the hand picked (set 0) performance. Ensembles always out-perform the average single-model prediction.

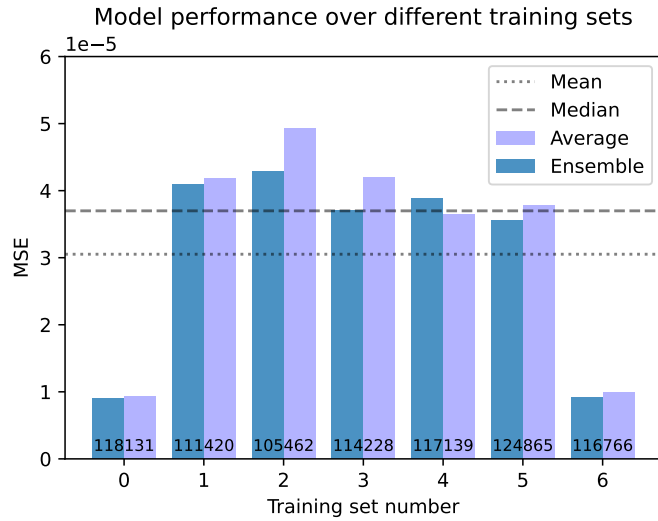


Figure 5.9: See caption for fig. 5.8. Note that the training loss is dramatically less than the testing loss, but otherwise there is no discernible trend.

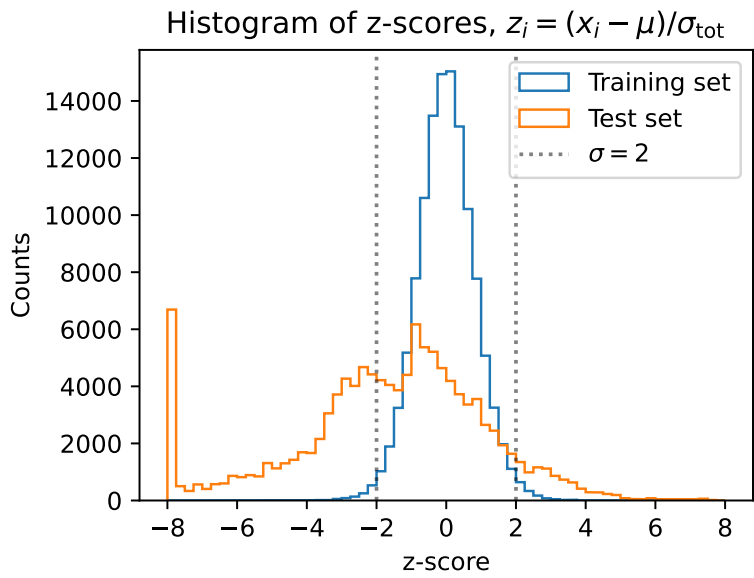


Figure 5.10: Z-scores for the training and testing set for the model with a weight decay coefficient  $\lambda$  of zero. The magnitude of counts for the test set is scaled up by a factor of 8.8 (the train-to-test example ratio). The histograms are clipped between  $z$  of -8 and 8 with a bin width of 0.25; the spike at the negative side of the test set histogram is from the long tail.

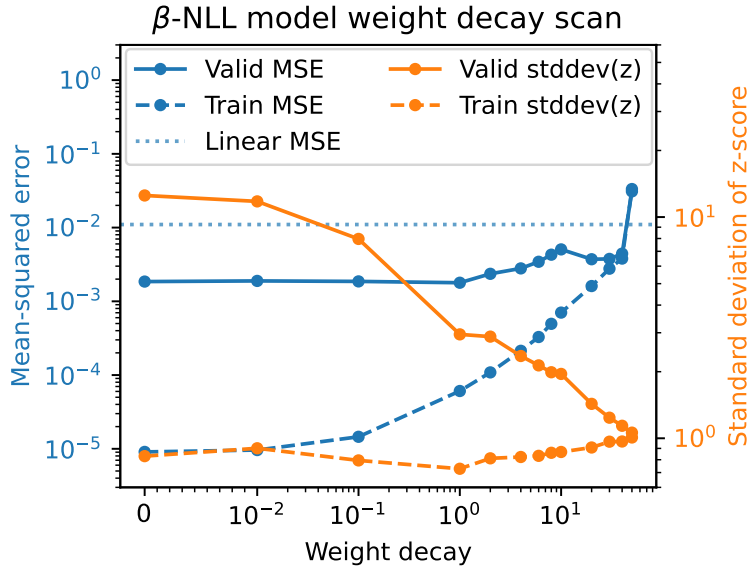


Figure 5.11: Model performance and calibration for different weight decays. Highly biased models are better calibrated, but come at great expense of mean prediction error. At the weight decay value of 50, the model has worse error than a linear model. Note the linear scale below  $10^{-2}$ .

trained with weight decay coefficients between 0 and 50 to determine the best calibrated model determined by the distribution of z-scores of the training and test sets. The results of this weight decay scan are seen in Fig. 5.11. Increasing the weight decay increases the test MSE and decreases its z-score standard deviation. This large standard deviation is caused by outliers. Excluding z-scores magnitudes above 10, or 4.4% of the test set, yields a standard deviation of 2.53. This long tail indicates that the distribution of predictions on the test set is not Gaussian. Nonetheless, the trend remains that increasing weight decay leads to smaller test set z-score standard deviations. However, the test set MSE increases after a weight decay of 1. This increase in test MSE implies that the model is making less accurate predictions but is better calibrated. Highly biased models are better calibrated, but come at great expense of mean prediction error. At the weight decay value of 50, the model has worse error than a linear model. Despite the attempts using weight decay, the model never becomes well-calibrated: the predicted uncertainty is always too low by a factor of 2 to 5.

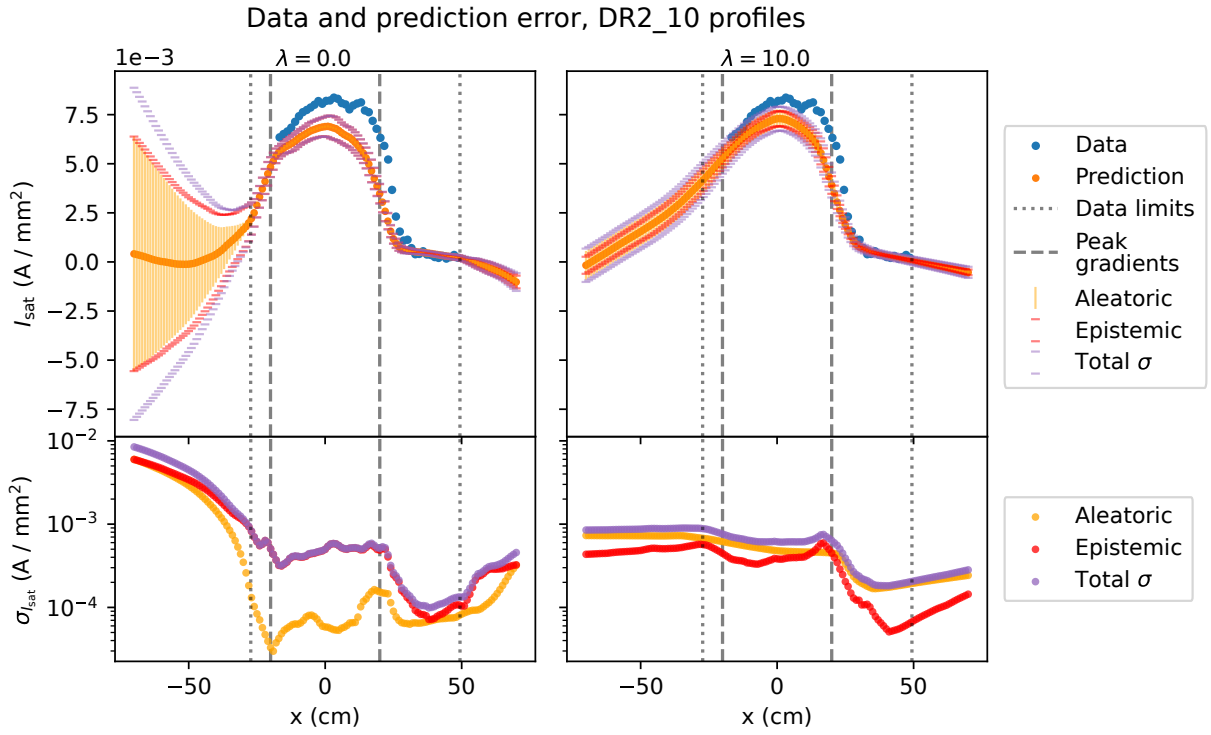


Figure 5.12: Model extrapolation performance (top plots) with uncertainty (bottom plots) for a model ensemble trained on a  $\beta$ -NLL loss function. DR2 run 10 was chosen as an illustrative example. The *relative* uncertainty appears to be more useful when zero weight decay ( $\lambda = 0$ , left) is used: the uncertainty increases when the model is predicting outside its training data along the x-axis.

Despite the better calibration, the uncertainty predicted by a model with a large weight decay is decidedly worse: the uncertainty is similar across an entire profile, and when projected beyond the training data, the total uncertainty remains largely constant as seen in Fig. 5.12. The zero weight decay model exhibits relatively increasing uncertainty beyond the bounds of the training data. Although not well-calibrated, this uncertainty can provide a hint of where the model lacks confidence relative to other predictions, even though the uncertainty is much less than it should be.

## 5.5 Evaluating model performance

Model performance is evaluated in three ways by comparing against intuition from geometry, an absolute measurement, and extrapolated machine conditions.

### 5.5.1 Checking geometrical intuition

Assuming magnetic flux conservation, we know that modifying the mirror geometry can control the effective width of the plasma. One way to check that the model is learning appropriate trends is to check with this intuition. If the magnetic field at the source is not equal to the field at the probe, the probe will see the plasma expanded (or contracted) by roughly a factor of  $\sqrt{B_{\text{probe}}/B_{\text{source}}}$ . The cathode is about 35 cm in diameter, so a magnetic field ratio of 3 would give produce a plasma approximately 60 cm in diameter. All the probes used in this study are in or very close to the zero-curvature midplane region of a mirror.

To check this intuition, the model is given the following inputs:  $B_{\text{source}}=500$  G,  $B_{\text{mirror}}=1500$  G,  $B_{\text{midplane}}=500$  G, discharge voltage=110 V, gas puff voltage=70 V, gas puff duration=38 ms, run set flag=DR2 and top gas puff=off. The discharge voltage and gas puffing parameters were arbitrarily chosen. The x coordinate is scanned from 0 to 30 cm, and the z coordinate from 640 to 1140 cm. This discharge is then modified by separately changing  $B_{\text{source}}$  to 1500 G and  $B_{\text{midplane}}$  to 750 G ( $M=1.5$ ). The x profiles at the midplane ( $z=790$  cm) of the reference  $M=3$  prediction, source field change, and midplane field change, all scaled to cathode radius, can be seen in Fig. 5.13. Changing the source field to 1500 G increases the  $I_{\text{sat}}$  towards the edge of the plasma, as expected. When the midplane field is increased, the  $I_{\text{sat}}$  values decrease at the edge and increase at the core ( $x=0$  cm), implying a thinner plasma column and is consistent with previously measured behavior. When only the mirror field is modified (not shown), the strongest effect on  $I_{\text{sat}}$  is on or near  $x=0$  cm, and the plasma column width does not appear to appreciably change.

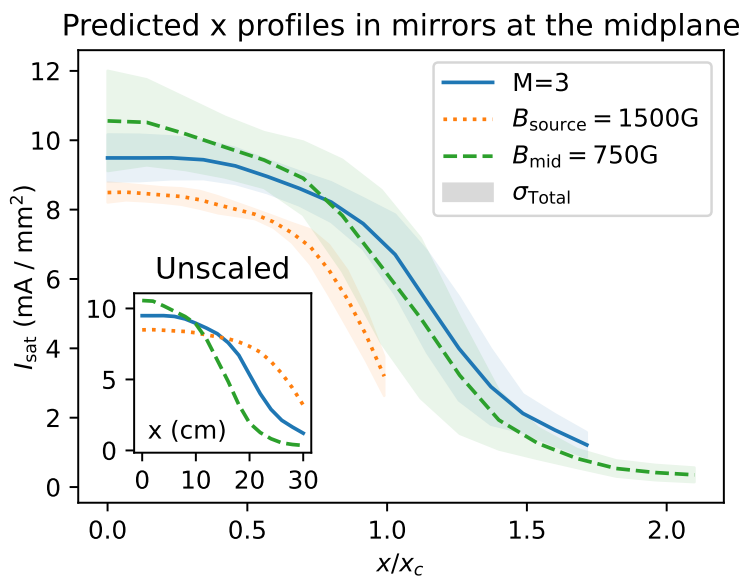


Figure 5.13: Plot of various mirror configurations scaled to the cathode radius  $x_c = 17.5$  cm at the midplane ( $z=790$  cm). When scaled according to the expected magnetic expansion, the profiles generally agree. The smaller the plasma diameter (and thus smaller volume), the higher the peak in  $I_{\text{sat}}$  at the core, as expected.

### 5.5.2 Directly comparing prediction to measurement

$I_{\text{sat}}$  measurements were taken with the following LAPD machine settings:  $B_{\text{source}}=1250 \text{ G}$ ,  $B_{\text{mirror}}=500 \text{ G}$ ,  $B_{\text{midplane}}=1500 \text{ G}$ , discharge voltage=90 V, gas puff voltage=90 V, gas puff duration=38 ms, run set flag=DR2 and top gas puff=off. These settings were from a previous discharge optimization attempt. The probes utilized were the permanently-mounted 45° probe drives. These probes were known to have identical effective areas relative to each other from the previous experiment and from analyzing the discharge rampup.

Because of data acquisition issues, only a single useful shot was collected at a nominal -45° angle (relative to the x-axis) 10 cm past the center ( $x=0 \text{ cm}$ ,  $y=0 \text{ cm}$ ) of the plasma on three probes at z-positions of 990, 767, and 607 cm (ports 22, 29, and 34, respectively). The probe drives were slightly uncentered, leading to the real coordinates of the probes to be around  $x = 9.75 \text{ cm}$  and  $y = -8.4 \text{ cm}$ . Note that the model can predict anywhere in LAPD bounded by the training data, so off-axis measurements are not an issue. The resulting predictions using these coordinates and machine conditions can be seen in Fig. 5.14. The model reproduces the axial trend well, but slightly underestimates  $I_{\text{sat}}$  on an absolute basis. However, given the lack of absolute  $I_{\text{sat}}$  calibration and variable machine state, the agreement of the absolute  $I_{\text{sat}}$  values may be coincidental. Nevertheless, the trend exhibited by this validation study match the predicted trend and increase our trust in model predictions.

An additional validation datarun was performed. For this run, the discharge voltage was increased to 160 V, and the source field changed to 822 G. The training data contains discharge voltages up to 150 V, so this case tests the extrapolation capabilities of the model. The comparison of model predictions and the measured data can be seen in Fig. 5.14. As stated earlier, the absolute uncertainty provided of the model is not calibrated. However, note that the level of uncertainty provided by the model, as well as the large spread in model predictions, are much greater than seen in the interpolation regime (Fig. 5.14) and eclipses the cross-validated test set root mean squared error (RMSE). We conclude that this model has good interpolation capabilities, but extrapolation –

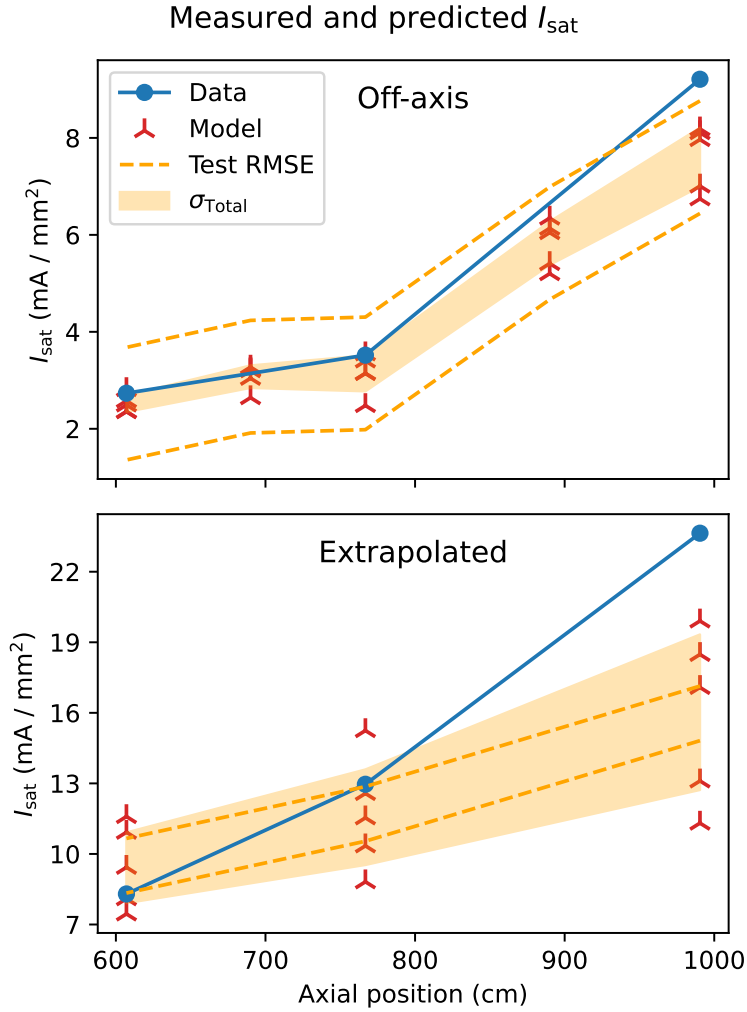


Figure 5.14: Top: data collected at off-axis positions around  $x = 9.75$  cm and  $y = -8.4$  cm are compared with predictions from the machine learning model at the same points in addition to two interpolating predictions. The model predicts the trend well, but underestimates  $I_{\text{sat}}$  in general. The shaded orange region is the total model uncertainty ( $\sigma = \sqrt{\text{Var}}$ ). Bottom: Measured vs predicted  $I_{\text{sat}}$  values for an odd machine configuration with  $B_{\text{source}}=822$  G and discharge voltage=160 V. The training data only covers discharge voltages up to 150 V. The machine was also in an odd discharge state, so it's no surprise that the predicted uncertainty bounds are very large (even greater than the test set RMSE value) and that accuracy suffers.

as with any model – remains difficult.

### 5.5.3 Comparison with Thomson scattering

The z-axis interpolation for dataruns in the training and test sets can be evaluated using the Thomson scattering (TS) diagnostic. The TS measurement is taken 8 ms into the discharge for DR1 12 ms into the discharge for DR2, but in this study the measured and predicted  $I_{\text{sat}}$  are instead averaged over 10 to 20 ms. The Thomson scattering measurement is compared in with DR1 and DR2 in figs. 5.16a and 5.16b, respectively. The linear slope fits do not take model error into account In DR1,  $I_{\text{sat}}$  predictions disagree with the  $I_{\text{sat}}$  derived from TS. Measurements from probes, when nearby the TS beam, can also have very different values from the TS-derived measurement. The TS density measurement may suffer from misalignment, and has not been calibrated since January 2022, roughly a year (DR1) or two (DR2) before these data were taken. The density measurement is photon counting and requires absolute calibration. This disagreement likely comes from this error in density because fitting the temperature is robust to absolute calibration errors. In addition, the  $I_{\text{sat}}$  is time-varying; the average may differ substantially from single points in time earlier in the discharge.

All these issues considered, the model predictions has rough agreement with TS on average in DR1, which is encouraging because the TS beam at port 32 (671 cm) is substantially further from the closest probe at port 27 (831). We should expect rough agreement or a slight underestimate on average based on the skewed test-set z-score seen in fig. 5.10). DR2 has a probe past the TS beam at port 33 (639 cm), but the  $I_{\text{sat}}$  measurement rarely agrees with Thomson. Because of this density error and measurement time discrepancy, we conclude that the TS diagnostic may not be a good way to verify the predictions of the model. Note that, when calibrated, TS agrees with  $I_{\text{sat}}$  measurements quite closely as seen in the LAPD Thomson scattering paper [GKG22].

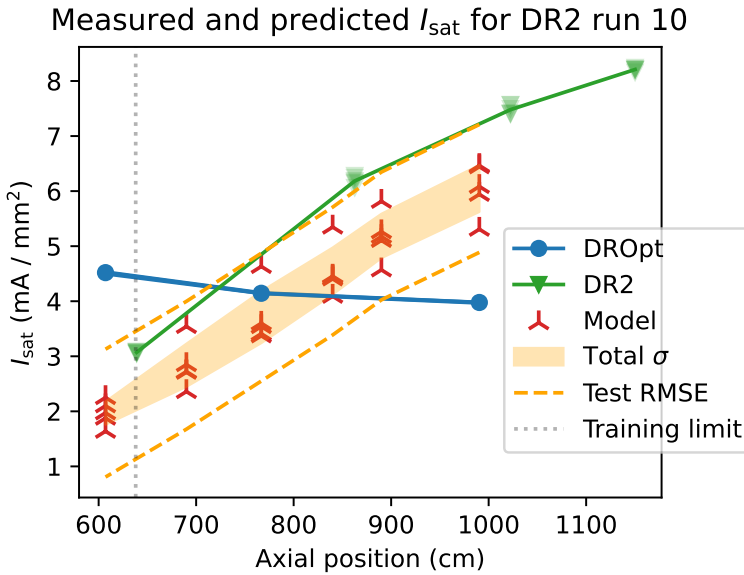
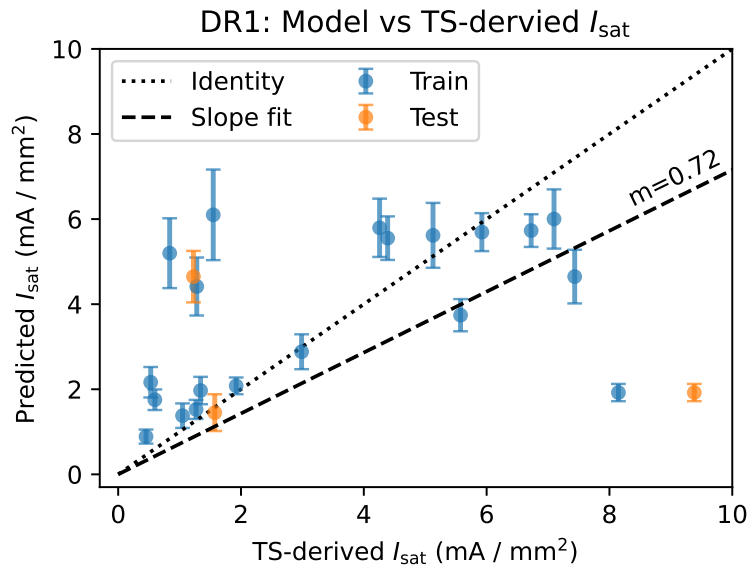


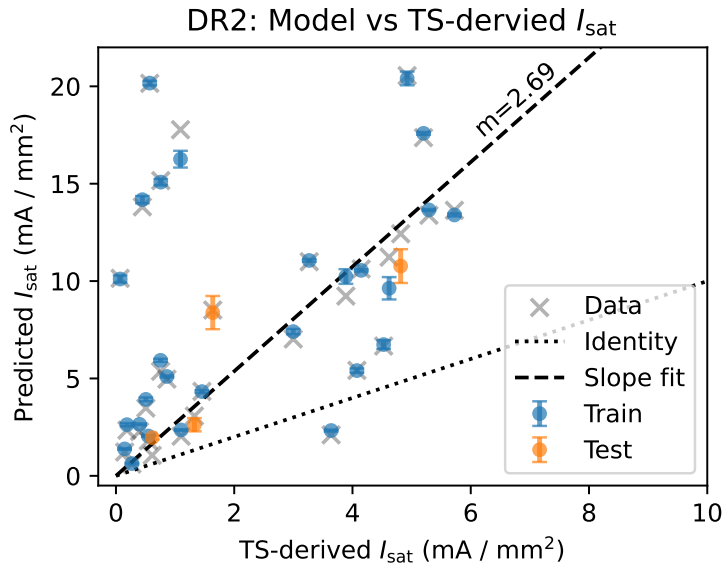
Figure 5.15: Comparison of original DR2 profiles with the profiles from the optimization dataset (DROpt) for the same machine configuration. The  $I_{\text{sat}}$  values in the DROpt dataset are not calibrated in this plot, indicating significant variation in probe calibration in this DROpt dataset.

## 5.6 Effect of $I_{\text{sat}}$ calibration

The Langmuir probes did not seem to be behaving correctly when the optimization validation data were taken. The probes showed an *increasing*  $I_{\text{sat}}$  profile when moving further from the cathode in the lowest gas puff condition, which is in direct disagreement with previous measurements and intuition. An example of this discrepancy can be seen in Fig. 5.15, where a run from the original testing set (specifically DR2 run 10) is duplicated. The probes for the validation run can be either corrected for by assuming the 5 ms gas puff run has a flat axial profile, or normalizing the probes to the DR2 run 10 axial profile. Calibrating the probes using the DR2 run 10 reference was the best way to go because it corrects for both probe discrepancies as well as changes in the condition (or emissivity) of the main cathode.



(a) Thomson scattering (TS) 8 ms into the discharge compared to the model predictions (10 to 20 ms averaged). Broadly speaking, the TS measurement roughly agrees with the model estimate on average.



(b) Thomson scattering (TS) 12 ms into the discharge compared to the model predictions (10 to 20 ms averaged) and  $I_{\text{sat}}$  measurements one port away. The TS underestimates  $I_{\text{sat}}$  in general.

Figure 5.16

## 5.7 Inferring trends

A systematic study of the impact of discharge voltages on  $I_{\text{sat}}$  profiles has not been conducted using conventional techniques. Collecting both z- and x-axis profiles over a wide range of discharge voltages would take a considerable amount of time, mostly from the requirement to dismount and reattach the probes and probe drives along the length of the LAPD. This study has now been performed using the learned model, circumventing these time-consuming challenges. Model input parameters were chosen to be common, reasonable values: 1 kG flat field, 80 V gas puff, 38 ms gas puff duration, run set=DR2, and top gas puff off. The 38 ms puff is used in these predictions because it is the most common gas puff duration in the training set – the model is biased in favor of this gas puff setting. The results of changing the discharge voltage only can be seen in fig 5.17. Notably, the  $I_{\text{sat}}$  increases across both axes. Steeper axial gradients are seen with lower discharge voltages, but peaked x-profiles are seen at higher discharge voltages. The area closer to the source region (+z direction) appears to have a steep drop but flatter profiles down the length of the machine.

Unfortunately the discharge current was not included as an output in the training set. Otherwise the effect of changes in discharge power, rather than simply voltage, could be computed. The discharge current – and thus discharge power – is set by cathode condition, cathode heater settings, and the downstream machine configuration, and thus cannot be set to a desired value easily before the discharge. Discharge voltage, however, can remain fixed.

Of particular interest for some LAPD users is achieving the most uniform axial profile possible. We explore this problem in the context of mirrors. The gas puff duration is known to be a large actuator for controlling density and temperature and so is explored as a way of shaping the axial profile. We predict discharges with a flat 1 kG field with the probe in the center. The discharge voltage was set at 110 (a reasonable, middle value) with the run set flag=DR2 and top gas puffing=off. The inferred effect of gas puff duration on the axial gradient and axial gradient scale length can be seen in Fig. 5.18. Care was taken to handle the aleatoric (independent) uncertainty separately from the axially-dependent epistemic uncertainty. As seen in the figure, the mean axial gradient

Discharge voltage: effect on x and z profiles

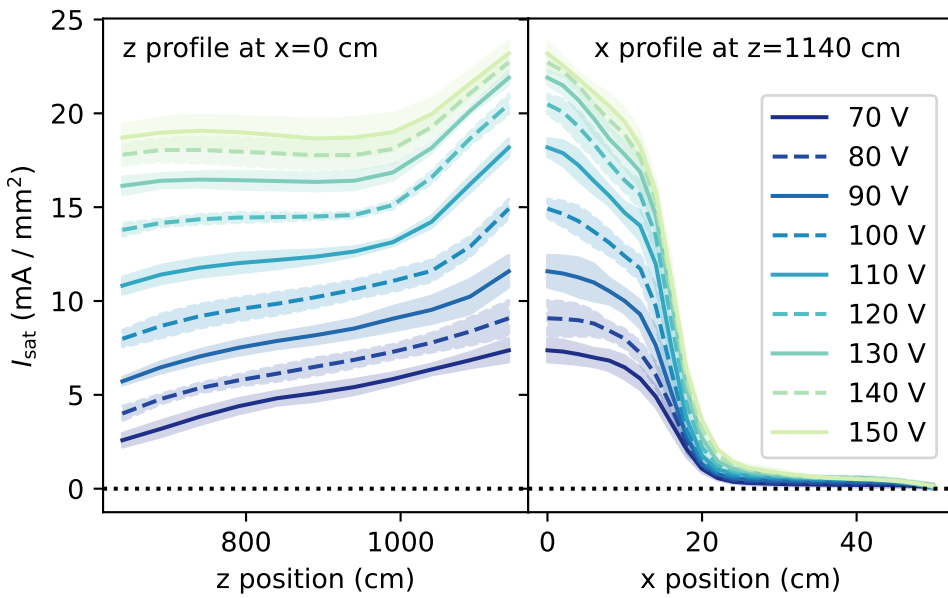


Figure 5.17: The z profile at  $x=0$  cm and x profile at  $z=1140$  cm for different discharge voltages. The  $I_{\text{sat}}$  decreases with increasing voltage, and the error (filled regions) stays roughly the same, but in general increase slightly towards the cathode and at higher discharge voltages.

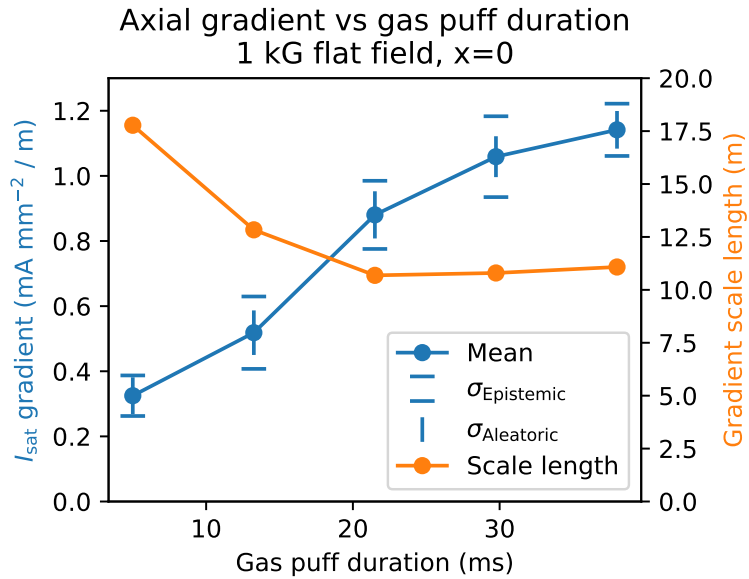


Figure 5.18: ML prediction: mean axial gradients decrease with decreased gas puff duration. Five durations are plotted between 5 and 38 ms (which are the bounds of the training data), evenly spaced. The gradient scale length also increases, indicating that the gradient change was not just from a decrease in the bulk  $I_{\text{sat}}$ .

decreases when the gas puff duration is shortened. The gradient scale length also increases, so the mean gradient is not decreasing simply because the bulk  $I_{\text{sat}}$  is decreasing. This result suggests that the gas puff duration may be a useful actuator to consider when planning future experiments.

The applicability of these results are somewhat muted because the gas puff duration was not chosen randomly in the training discharges. Given this lack of data diversity, the accuracy and applicability of this study must be interpreted cautiously. When a model is trained on *all* data available (using the cross-validated test set MSE as a guide for error), which includes the 20 ms gas puff case, the predicted gradient scale length decreases uniformly across the duration scan by 1 meter. The fact that the trend remains intact when an additional, randomized intermediate gas puff case is added gives confidence in the predictions of the model despite the lack of data diversity.

## 5.8 Optimizing profiles

One particular issue seen in LAPD plasmas is sharp axial density and temperature gradients. Some experiments require flat gradients, such as Alfvén wave propagation studies. We explore optimizing the axial  $I_{\text{sat}}$  variation as an approximation to this problem. In addition, in this case the optimization problem is used as a tool to evaluate the quality of the learned model. This is a very demanding task because the trends inferred by the model along all inputs must simultaneously be accurate. Constraints on this optimization further increase the difficulty of the problem. Success in optimization provides strong evidence that the model has inferred relevant trends in predicting  $I_{\text{sat}}$ . We quantify the uniformity of the axial profile by taking the standard deviation of  $I_{\text{sat}}$  of 11 points along the z-axis ( $x, y = 0$ ). The required LAPD state for attaining the most uniform axial profile can be found by finding the minimum of this standard deviation with respect to the LAPD control parameters and flags:

$$\text{Inputs} = \arg \min_{\substack{\text{Inputs} \neq z}} \text{sd}(I_{\text{sat}}|_{x=0}) \quad (5.3)$$

The largest axial variation can likewise be found by finding the maximum. The model inputs used for this optimization can be found in Table 5.2.

For this optimization we use an ensemble of five  $\beta$ -NLL-loss models with weight decay  $\lambda = 0$ . The  $\lambda = 0$  model is used because it appears to give the most useful uncertainty estimate (seen in Fig. 5.12). The optimal machine actuator states are found by feeding a grid of inputs into the neural network. This variance estimate is not well-calibrated: the error of the predictions on the test set falls far outside the predicted uncertainty. However, this uncertainty can be used in a relative way: when the model is predicting far outside its training range, the predicted variance is much larger. The ranges of inputs into this model are seen in Table. 5.2. These inputs yield 127,234,800 different machine states (times five models) which takes 151 seconds to process on an RTX 3090 ( $\approx 4.2$  million forward passes per second) when implemented in a naive way. The number of forward passes can be reduced by a factor of 51 if the x value is set to 0 cm. Note that gradient-based methods can be used for search because the network is differentiable everywhere but this network

Table 5.2: Machine inputs and actuators for model inference

Input or actuator	Range	Step	Count
Source field	500 G to 2000 G	250 G	7
Mirror field	250 G to 1500 G	250 G	6
Midplane field	250 G to 1500 G	250 G	6
Gas puff voltage	70 V to 90 V	5 V	5
Discharge voltage	70 V to 150 V	10 V	9
Gas puff duration	5 ms to 38 ms	8.25 ms	5
Probe x positions	-50 cm to 50 cm	2 cm	51
Probe y positions	0 cm	—	—
Probe z positions	640 cm to 1140 cm	50 cm	11
Probe angle	0 rad	—	—
Run set flag	off and on	1	2
Top gas puff flag	off and on	1	2

and parameter space is sufficiently small that a comprehensive search is computationally tractable.

Like any optimization method, the results may be pathologically optimal. In this scenario, the unconstrained minimal axial variation is found when the  $I_{\text{sat}}$  is only around  $1 \text{ mA/mm}^2$ , which is quite small and corresponds to  $1\text{-}2 \times 10^{12} \text{ cm}^{-3}$  depending on Te. The inputs corresponding to this optimum are given in the second column of Table 5.3. This density range is below what is required or useful for many studies in the LAPD.

Since many physics studies require higher densities, we constrain the mean axial  $I_{\text{sat}}$  value to be greater than  $7.5 \text{ mA/mm}^2$  (roughly  $0.5\text{-}2 \times 10^{13} \text{ cm}^{-3}$ ). The “run set flag” is set to “on” for cases to be validated (bolded in Table 5.3) because we wish to keep the turbopumps on to represent typical LAPD operating conditions. In addition the “top gas puff flag” was set to ‘off’ to minimize the complexity of operating the fueling system on followup dataruns and experiments. Turning the top gas puff valve on is predicted to decrease the average  $I_{\text{sat}}$  by  $-2 \text{ mA/mm}^2$  for strongly varying profiles, but otherwise the shapes are very similar. The inputs corresponding to the maximum and minimum axial variation under these constraints can be seen in columns 3 and 4 of Table 5.3. For contrast we also consider what machine settings would lead to the greatest axial variation. The results of both of these optimizations can be seen in Fig. 5.19. The optimizations yield profiles that have the largest  $I_{\text{sat}}$  values closest to the cathode, which is expected.

The prediction for an intermediate axial variation case is also seen in Fig. 5.19. The intermediate case was chosen as somewhere around half way between the strongest and weakest case with a round index number (15000, in this case). The parameters for intermediate case are also enumerated in Table 5.3.

The predicted configurations with the run set flag on and top gas puff flag off (bolded in Table 5.3) were then applied on the LAPD. The data collected, compared with the predictions can be seen in Fig. 5.19.

For the optimized axial profiles, the absolute value of the  $I_{\text{sat}}$  predictions compared to measurement do not agree. All of the predicted profiles have overlapping predictions (within the predicted

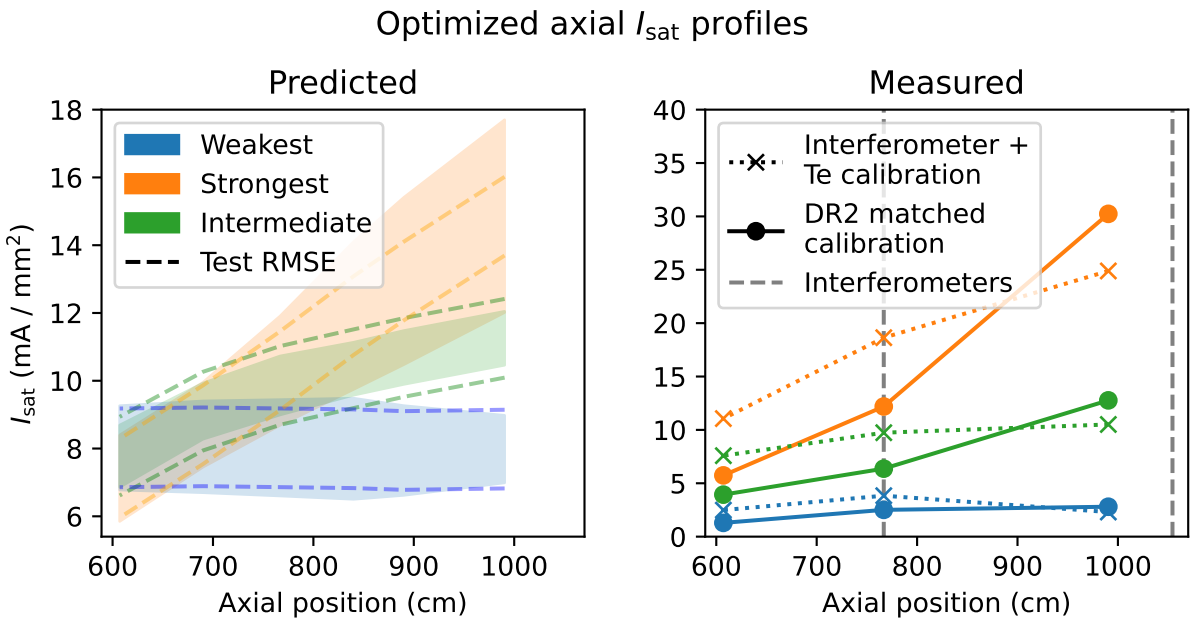


Figure 5.19: Axial profiles, predicted and measured, for the optimized weakest (blue), intermediate (green), and strongest (orange) cases. a. The shaded region covers the mean prediction  $\pm$  one standard deviation, and the dashed lines are  $\pm$  the median cross-validation RMSE values. b. The measured  $I_{\text{sat}}$  values are calibrated to DR2 run 10 (solid lines), or using triple probe Te measurements on the probe and linearly extrapolating the interferometer measurements (dotted lines). The absolute values disagree between the predicted and measured values, but axial trends are consistent with the optimization.

Table 5.3: Machine inputs and actuators for optimized axial profiles

Input or actuator	Weakest	<b>Weakest</b>	<b>Strongest</b>	Intermediate
$I_{\text{sat}}$ constraint (mA/mm <sup>2</sup> )	$I_{\text{sat}} = \text{any}$	$I_{\text{sat}} > 7.5$	$I_{\text{sat}} > 7.5$	$I_{\text{sat}} > 7.5$
Source field	750 G	1000 G	500 G	2000 G
Mirror field	1000 G	750 G	500 G	1250 G
Midplane field	250 G	250 G	1500 G	750 G
Gas puff voltage	70 V	75 V	90 V	90 V
Discharge voltage	130 V	150 V	150 V	120 V
Gas puff duration	5 ms	5 ms	38 ms	38 ms
Run set flag	on	on	on	on
Top gas puff flag	on	off	off	off

error) at the region furthest from the cathode, but the measured values do not show that behavior. Although the mean  $I_{\text{sat}}$  value was constrained to be greater than 7.5 mA/mm<sup>2</sup>, the measured mean was 2 mA/mm<sup>2</sup> for the weakest case.

The important result is that the optimized LAPD settings, when implemented on the machine, do yield profiles with strong, intermediate, and weak axial variation. Although the minimum- $I_{\text{sat}}$  constraint was violated for the case of weakest axial variation case, this optimization would nonetheless be very useful for creating axial profiles of the desired shape.

There are three contributing factors to the mismatch of the ML-predicted values and the real measured values. First, the condition of the machine, such as the cathode emissivity or temperature or the downstream neutral pressure, are unquantified and cannot be compensated for in data preprocessing or in the model itself. Second, the calibration of the Langmuir probes could differ substantially between runs. The probes in the training data run sets (DR1 and DR2) were well-calibrated to each other within the run set, but were not absolutely calibrated. The probes used for verifying the optimization were not calibrated. A rough calibration was performed by linearly extrapolating interferometer measurements and using triple probes (dotted lines on the right panel

in Fig. 5.19). A configuration identical to DR2 run 10 was also measured to simultaneously correct cathode condition and probe calibration (solid lines on the right panel in Fig. 5.19). Langmuir probe calibration is discussed further in Appendix 5.6. Third, the original dataset may not have sufficient diversity to make accurate predictions on such a constrained optimization problem.

If this optimization were performed using the dataset instead of the model, the constrained search would encompass just 10084 shots out of the 131550 shots total in the training dataset, or around 7.7%. Including the on-axis constraint reduces the number of shots down to 303 (270 in the training set), or 0.23% of all shots in the dataset. We conclude that this optimization of an arbitrary objective function, as done here, would be intractable using traditional, non-machine learning techniques because orders of magnitude more dataruns would need to be collected.

Optimization requires correctly learning the trends of all inputs and how they interact. In addition, as seen from the shot statistics, the model was trained on very few shots in the constrained input and output space. These two factors – the need for the model to learn all trends and the constrained search space – combine to make an incredibly difficult task that functions as a benchmark for the model. These factors considered, it is not surprising that the model incorrectly predicts the absolute value. The uncertainty predicted by the model, though not well-calibrated, was nonetheless very large compared to the median test set RMSE. The model did predict the trends correctly, however; the optimized, measured profiles were strong, intermediate, or weak.

We did not check to see if the predicted optima were actually true optima: an approximation of the local derivative using a finite-difference technique would require much more run time on the LAPD than was available.

## 5.9 Discussion

### 5.9.1 Key achievements

To my knowledge, this work is one of the first instances machine learning has been used to infer specific trends and optimize profiles in magnetized plasmas. Three examples of trend inference were shown in this study: influence of magnetic geometry on plasma width, changes in the axial and radial profiles with changing discharge voltage, and the relationship of gas puff duration with axial gradient scale length. In addition, the axial profile was optimized by minimizing (or maximizing) the axial standard deviation. There is no other way of simultaneously uncovering many trends or finding optima without using an ML model trained on a diverse dataset. Traditionally, such studies would require extensive scans over grids to map the parameter space, but here it was accomplished with a relatively small amount of data.

The trends inferred in this work, such as changing discharge voltages, gas puff durations, or mirror fields, would traditionally require a grid scan (varying one parameter at a time) in LAPD settings space. Here instead we are able to extract any trend covered by the training set with only a minimal amount of machine configurations sampled. Both data collection runs lacked absolute  $I_{\text{sat}}$  calibration and had potential differences in cathode condition. Despite these issues the model learned trends that were exploited via optimization.

In addition, this work demonstrates uncertainty quantification broken down into epistemic and aleatoric components by using ensembles and a negative-log likelihood loss. This uncertainty estimate is useful in gauging relative certainty between different predictions of the model which increases confidence in the predictions of the model. In general, the total uncertainty predicted by the model increases when predictions are made outside the bounds of the training data.

Fundamentally, this model can predict  $I_{\text{sat}}$  with uncertainty at any point in space covered by the training data. No other model currently exists that can perform this prediction. Traditionally, this capability would be possible only with a detailed theoretical study.

## 5.9.2 Current limitations

This study would be dramatically improved by collecting more, diverse data. Only 44 of the 67 dataruns in this dataset had randomly sampled LAPD machine settings which is very small compared to the over 60,000 possible combinations. In addition, there are many other settings or parameters that were not changed in this study, such as gas puff timings, gas puff valve asymmetries, wall/limiter biasing, cathode heater settings, operation of the north cathode, and so on. The bounds of the inputs were also conservative; all settings in this study could be pushed higher or lower with a small amount of risk to LAPD operations. In addition, the placement of the probes could be further varied and placed outside the mirror cell, which would provide a more complete picture of LAPD plasmas, particularly axial effects.

Probe calibrations differed between the two training run sets (DR1 and DR2) – and a flag was introduced to distinguish between them – but despite this deficiency combining the two run sets was shown to be advantageous for model performance. The condition of the cathode (e.g., electron emissivity and uniformity) also has a large impact on the measured  $I_{\text{sat}}$ . The improved model performance with the flag suggests that inconsistencies between dataruns could be compensated for using latent variables if a generative modeling approach is to be taken. At the very least, this model provides a way to benchmark these differences in machine state.

Concerning the model, hyperparameter tuning could be performed. In this study a few extra percent in MSE performance is not meaningful considering the limited dataset. Instead, we focused on the trends and insights that can be extracted from this model rather than simple predictive accuracy. There may also be regimes in hyperparameter space where the uncertainty is better calibrated (perhaps using early stopping). Uncertainty estimation is important, even if the absolute uncertainty is not well-calibrated because it can provide a useful relative estimate as shown in this study.

Trends such as the dependence of axial gradient on the gas puff duration (fig. 5.18) or the effect discharge voltage on x-z profiles (fig. 5.17), although intuitive, remain unverified. Verification of

these trends would increase confidence of model predictions when setting LAPD parameters in future experiments.

### 5.9.3 Future directions

The neural network architecture used here can readily scale to additional inputs and outputs; including time-series signals is the obvious next step. Integration of multiple diagnostics – perhaps starting with individual models before combining them – could enable inference of plasma parameters throughout the device volume. For example, combining triple probe electron temperature measurements with existing  $I_{\text{sat}}$  data would allow density predictions anywhere in the plasma. This capability could enable in-situ diagnostic cross-calibration (e.g., the Thomson scattering density measurement) and prediction of higher-order distribution moments like particle flux. The model could be further enhanced by incorporating physics constraints such as boundary conditions (e.g., zero  $I_{\text{sat}}$  at the machine wall) or symmetries.

The problem presented here – learning time-averaged  $I_{\text{sat}}$  trends – is fairly simple and required a relatively simple model. As demonstrated in this work, ML provides a way to explore regions of parameter space quickly and efficiently. Most physics studies on plasma devices (and fusion devices) are dedicated to a single particular problem, use grid scans, and are not useful to other experiments or campaigns. This work shows a way of using data and trends uncovered from other experimental studies. This work also demonstrates that random exploration can be a useful tool: the increased diversity of the aggregated data will generally benefit an ML model whether the experimenter discovers something new or not.

## 5.10 Conclusion

We demonstrate the first randomized experiments in a magnetized plasma experiment to train a neural network model. This learned model was then used to infer trends when changing field configuration, discharge voltage, or gas puff duration. This model was also used to optimize axial

variation of  $I_{\text{sat}}$  as measured by the standard deviation, which was validated in later experiments despite poor absolute error.

We strongly advocate that all ML-based analyses in plasma and fusion research should be validated and used to gain insight by inferring trends, as demonstrated here. This validation step is crucial for ensuring that ML models capture physically meaningful relationships and the insights provided may provide direction for future research. We hope this is the first step towards automating plasma science.

## 5.11 The open dataset and repository

All the code to perform the ML portion of this study is available at <https://doi.org/10.5281/zenodo.1500783>. The training datasets are also available in that repository in the datasets directory. Additional data are available upon request. The repository also contains additional training details and the notebooks for generating the plots in this document. The plots used in this study were made in jupyter notebooks, which are also uploaded. The final training code can be found in `train_dense_beta_NLL.py`. Trained models are found in the `code/training_runs` directory. The history of many training runs can be found on Weights and Biases: <https://wandb.ai/phil/profile-predict> and the accompanying notes on these trained models are found in the associated pdf on github. The code and dataset are licensed under Creative Commons Attribution Share Alike 4.0 International.

# CHAPTER 6

## Reconstructing missing diagnostics using energy-based models

nergy-based models (EBMs) provide a powerful and flexible way of learning relationships in data by constructing an energy surface. We extend EBMs to laboratory plasma physics, a domain characterized by highly nonlinear phenomena studied using incomplete diagnostic information. These diagnostics can be unreliable or difficult to analyze. In addition, the possible configuration space of a plasma device is sufficiently large that it cannot be efficiently searched using conventional analysis techniques. EBMs provide a way to address these issues. At the Large Plasma Device (LAPD), a CNN- and attention-based EBM is trained over a set of randomly generated machine conditions and the corresponding diagnostic time series. We demonstrate diagnostic reconstruction using this EBM and also show that including additional diagnostics improves reconstruction error and generation quality. This model can also be used to infer trends by conditionally sampling along a grid. Symmetries in the data can be found by directly evaluating the energy surface, potentially leading to a new line of inquiry using learned models. In addition, this multimodal EBM is able to unconditionally reproduce all distributional modes, suggesting future potential in anomaly detection on the LAPD. Fundamentally, this work demonstrates the flexibility and efficacy of EBM-based generative modeling of laboratory plasma data, and demonstrates practical use of EBMs in the physical sciences.

### 6.1 Introduction

Nuclear fusion is an upcoming potential energy source that could offset carbon emissions and provide cleaner energy. Developing a fusion reactor is challenging: the environment is hostile to

measurement (diagnostics can malfunction or break) and the physics of plasmas is highly nonlinear and dynamical. We seek to use machine learning – particularly generative models – to alleviate some of the challenges facing fusion-related plasma science and to accelerate the advent of fusion power.

The use of generative models in plasma physics is not without precedent, but remains relatively uncommon. Variational autoencoders [KW22] have been used to generate new, realistic output from stellarator transport simulations for inferring trends and uncovering physics [Len22] and to discover relationships between inputs and outputs [Vos24]. These VAEs have also been used in the COMPASS to identify a rare instability characterized by fluctuations in magnetic probes [P20] by pertaining on unlabeled data and combining the model with a classifier over a smaller, labeled dataset.

On the Joint European Torus experiment, a generative topographic map was used to create a 2d representation of a 7d input space (information from 1d profiles) [PFC19]. This mapping clearly shows a disruptive-nondisruptive boundary and the relative stability of locations in this 2d representation can be evaluated by visualizing cluster distances. Discharge trajectories can be visualized in this reduced 2d space. Likewise on the HBT-EP tokamak, a VAE was trained on coil currents, equilibrium properties, and MHD information to learn a 2d latent representation [WLH21]. This model was run in real time to identify threshold crossing events which then triggered preprogrammed countermeasures.

Generative-adversarial networks (GANs) [GPM14] have also been used to generate synthetic training data (time series of plasma current) for use in training a disruption predictor [DPS23]. GANs have also be used to generate posterior distributions of surface temperature and emissivity given the measured radiance for the thermal surface-pointed cameras on the WEST tokamak [JAM24].

Diagnostic reconstruction is useful in the event a diagnostic goes offline, but it can also be used to supplement existing diagnostics. One such example is the upsampling of the Thomson scattering signal on DIII-D based on information from other diagnostics using a neural network-based solution

[JKS24]. In addition, Bayesian and ML work in fusion has been recently reviewed[PMK23].

Outside of magnetized plasmas, random experiments were performed in an inductively coupled plasma (ICP) similar to the process used to collect for this work. These data were used to train a VAE as a surrogate collisional radiative model [DFH23] to construct an interpolatable latent representation.

Concerning EBMs, they have yet to be applied to plasma physics problems. One notable application in the physical sciences has been in the high-energy physics community. EBMs were used for modeling event patterns in the Large Hadron Collider (LHC) for anomaly detection and to augment a classifier [CC24] with success.

Energy-based models interpret a probability distribution through the lens of the Boltzmann distribution [Hop82, AHS85, LCH06]. In the EBM formulation, the unnormalized probability density is parameterized by an energy function, that is  $\tilde{p}(x) = \exp(-\beta E_\theta(x))$ . EBMs have been historically difficult to train, but recent work has demonstrated high-quality sampling using MCMC techniques in high-dimensional spaces [DLM19, DM20, DLT21, DLM20, DLS21, NHH20, NHZ19, DBO20]. These MCMC techniques are fundamentally based in contrastive divergence

Training via contrastive divergence can be improved by implementing a term typically left out which approximates the KL-divergence [DLT21].

Training and generation of energy-based models can be performed using MCMC techniques, attaining GAN-like performance while generating all modes of a distribution [DM20].

Energy-based models can be composed by combining the energy functions in various ways which has been demonstrated in image generation tasks [DLM20, DLS21].

Original tutorial on EBMs .

The nature of MCMC-based sampling of EBMs, detailing the convergence and expansion/contraction of learned models (which was a paradigm particularly helpful for training EBMs in this work) [NHH20, NHZ19].

Classifiers have been interpreted in the context of EBMs to gain benefits of generative modeling

while still achieving good accuracy.

Model based planning with EBMs [DLM19]

EBMs for text generation [DBO20]

Contrastive divergence as proposed by Hinton [Hin02]

Overview of EBMs, how they are trained, and their place among generative models [Car24].

Another helpful review of generative modeling that helped in the selection by detailing advantages and disadvantages of various methods [BLL21].

One of the earlier MCMC-based EBM papers [GLZ18].

.Hopfield nets:. Deep Boltzman Machines used contrastive divergence [SH09]. Persistent contrastive divergence: [Tie08].

## 6.2 Problem statement

### 6.3 Data preparation

130 thousand shots were taken on the Large Plasma Device for 67 different dataruns (varying machine conditions and probe configurations). Focus was placed on mirror configurations.

An additional dataset of 29 million shots was collected over the span of 3 years

The original sampling rates for the machine state information and auxiliary diagnostics is 25 kHz. The sampling rate for the  $I_{\text{sat}}$  probe was 6.25 MHz. All time-series data were downsampled to a common sampling rate of 2.5 kHz. The time series are now 76 points long, and the MSI were truncated to be identical in duration and start time to the  $I_{\text{sat}}$  time series.

Downsampling for the dataset, train/test split

$$\mathcal{L} = \text{loss function} \quad (6.1)$$

---

**Algorithm 1** EBM training

---

**Require:** Training samples  $x_i^+$ , training data distribution  $p_D$ , energy function  $E_\theta$ , replay buffer  $\mathcal{B}$ , step size  $\epsilon$ , MCMC steps  $L$ , KL MCMC steps  $K$ , energy regularization strength  $\alpha$ , stop gradient operator  $\Omega(\cdot)$ , replay fraction  $f_{\mathcal{B}}$ , batch size  $M$

$\mathcal{B} \leftarrow \mathcal{U}(-1, 1)$  ▷ Fill buffer from uniform distribution

**while** not converged **do**

$$x_i^+ \sim p_D$$

$$\tilde{x}_i^0 \sim \mathcal{B} \text{ sample } Mf_{\mathcal{B}} \text{ negative examples, } \mathcal{U}(-1, 1) \text{ otherwise}$$

$$X \sim \mathcal{B} \text{ nearest-neighbor samples such that } X \cap \tilde{x}_i^0 = \emptyset$$

**for** sample step  $\ell = 1$  to  $L$  **do** ▷ Run Langevin dynamics

$$\tilde{x}_i^\ell \leftarrow \tilde{x}_i^{\ell-1} - \frac{\epsilon^2}{2} \nabla_x E_\theta(\tilde{x}_i^{\ell-1}) + \epsilon \mathcal{N}(0, 1)$$

**end for**

$$\tilde{x}_i^L = \Omega(\tilde{x}_i^L)$$

$$\hat{x}_i^0 = \tilde{x}_i^\ell \text{ where } \ell = L - K \quad \text{▷ Run Langevin dynamics for KL loss}$$

**for** KL sample step  $k = 1$  to  $K$  **do**

$$\hat{x}_i^k \leftarrow \hat{x}_i^{k-1} - \frac{\epsilon^2}{2} \nabla_x E_\theta(\hat{x}_i^{k-1}) + \epsilon \mathcal{N}(0, 1)$$

**end for**

$$\mathcal{L}_{\text{CD}} = \frac{1}{M} \sum_i E_\theta(\tilde{x}_i^+) - E_\theta(\tilde{x}_i^L)$$

$$\mathcal{L}_{\text{KL}} = \frac{1}{M} \sum_i E_{\Omega(\theta)}(E_\theta(\hat{x}_i^K) - \text{NN}(X, \hat{x}_i^K)) \quad \text{▷ Has gradients through MCMC}$$

$$\mathcal{L}_{\text{reg}} = \frac{1}{M} \sum_i E_\theta(\tilde{x}_i^+)^2 + E_\theta(\tilde{x}_i^L)^2$$

$$\mathcal{L} = \mathcal{L}_{\text{CD}} + \mathcal{L}_{\text{KL}} + \alpha \mathcal{L}_{\text{reg}}$$

Apply  $\nabla_\theta \mathcal{L}$  to  $\theta$  via the Adam optimizer

$\mathcal{B} \leftarrow \mathcal{B} \cup \mathcal{U}(-1, 1)$  and remove samples to maintain buffer size

**end while**

---

---

**Algorithm 2** EBM sampling

---

**Require:** Energy function  $E_\theta$ , auxiliary energy function  $F$ , step size  $\varepsilon$ , MCMC sampling steps  $L$

$\tilde{x}_i^0 \sim \mathcal{U}(-1, 1)$  ▷ Initialize on uniform distribution

**for** sample step  $\ell = 1$  to  $L$  **do** ▷ Run Langevin dynamics

$$\tilde{x}_i^\ell \leftarrow \tilde{x}_i^{\ell-1} - \frac{\varepsilon^2}{2} \nabla_x \left( E_\theta(\tilde{x}_i^{\ell-1}) + F(\tilde{x}_i^{\ell-1}) \right) + \varepsilon \mathcal{N}(0, 1)$$

**end for**

---

Return  $\tilde{x}_i^L$

---

Energy-based models are trained using contrastive divergence. A derivation will not be performed here (see ref. TODO: [REF](#)).

**Sampler configuration** The sampler is fundamental to how the model is trained and is critical. The negative samples are fundamental to how this model works. Step size and the number of steps needs to be tuned to converge well. The optimizer is important too.

The 30 MCMC steps were used per training batch with a step size of 1e-2 for AdamW (1e-1 for SGD)

**Replay buffer configuration** A replay buffer is used to provide a warm start for the sampler chains. Every batch iteration, 5% of the samples from the buffer are replaced with random noise (a replay fraction of 0.95). This replay fraction leads to a mean of  $1/0.05=20$  batch iterations for each chain, with half the chains experiencing  $\ln(2)/0.05 \approx 14$  batches. The replay buffer requires 4 to 5 epochs to converge to an exponential distribution in the number of steps experienced by each chain in the buffer. This diversity of chain lengths likely encourages quick convergence of the chain but good long-term samples (on average, each chain experience 600 MCMC updates/steps). The distribution of the batches among the replay buffer can be seen in fig. 6.1.

This also means that bad samples have a  $\approx 50\%$  chance of lasting 194 batches if one goes awry.

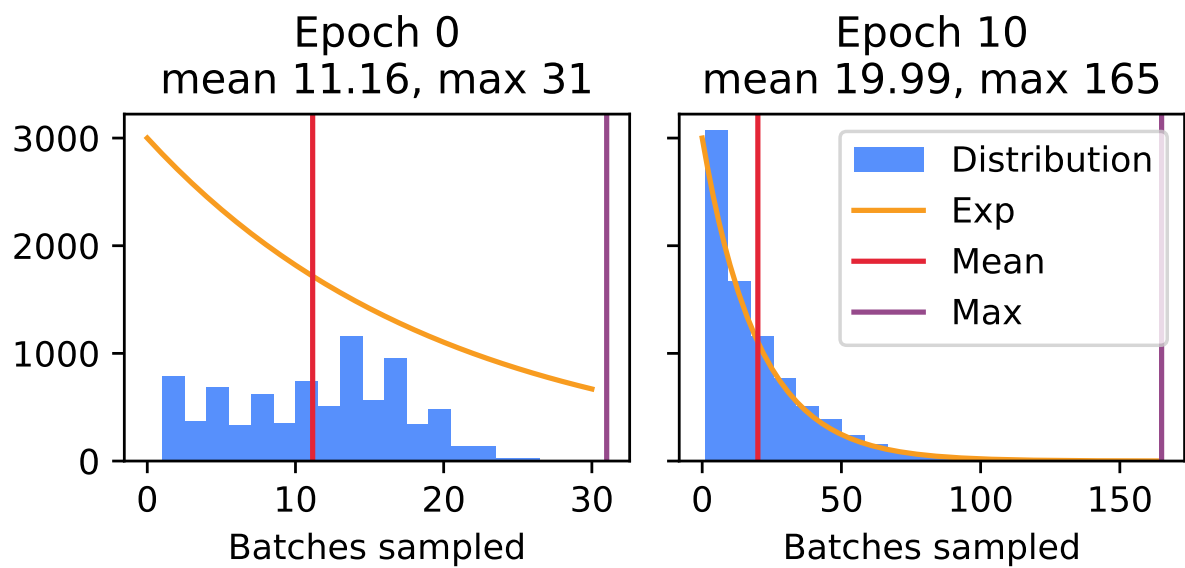


Figure 6.1: Distribution of batches in replay buffer. When training is starting (epoch 0, left), the number of batches each sample experiences is low and somewhat uniform. After 10 training epochs (right), the number of batches experienced by a sample converged to an exponential distribution.

### **6.3.1 Architecture**

The model is intrinsically multi-modal: time-series data from diagnostics is mixed in with machine settings, state, and probe position. Training on multi-modal data is difficult because it's difficult to weight the particular components of the input that are important. Not all inputs are necessarily correlated, and the less correlated (read: number of inputs not correlated with it) the harder it is to train. The “position” (x, y, and z) feature is like this because only the  $I_{\text{sat}}$  time series is related to it.

Pretraining an autoencoder was attempted to improve training stability but that did not help at all. The most important factor for training stability was the step size.

Convolutional NNs were used for the time series input, and transformer-like multi-head attention blocks were used for the settings, state, and probe position. The time series convolutions were merged in another convolutional pass, and the two branches were combined using multi-head attention. Fully-connected networks were found to be difficult to train (which has been observed in other studies [CC24]) and are only used when projecting representations to higher or lower dimensions.

### **6.3.2 Training tips**

Training with conditional samples did not work.

## **6.4 Unconditional sampling**

90 steps takes 3 seconds

## **6.5 Conditional sampling of interferometer signals**

The interferometer can be sampled. On samples based on test-set data, the output can go negative which is unphysical. A constraint can be added to eliminate these negative portions of the time

## Energy model architecture

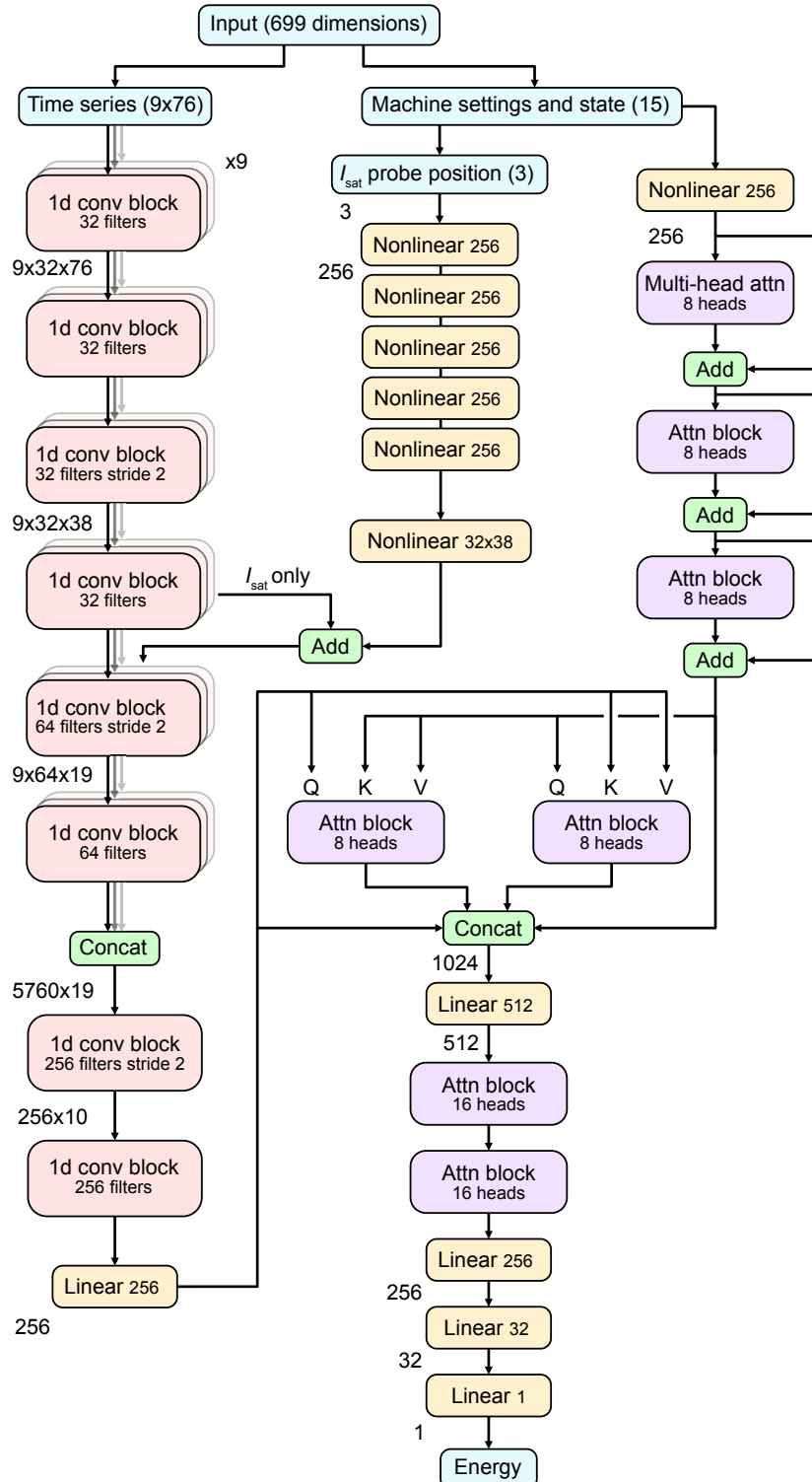
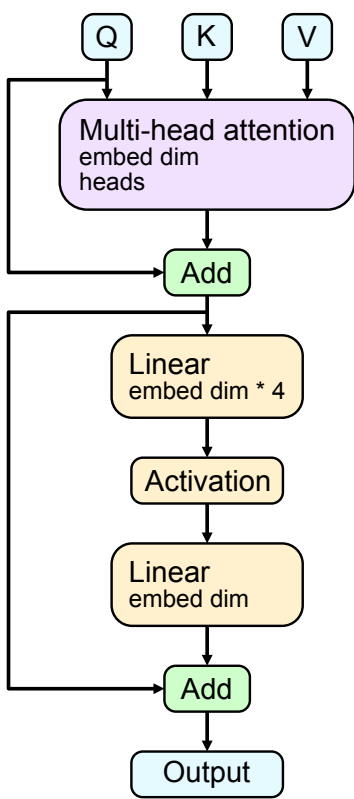


Figure 6.2: EBM arch  
125

## Attention block



## 1d convolutional block

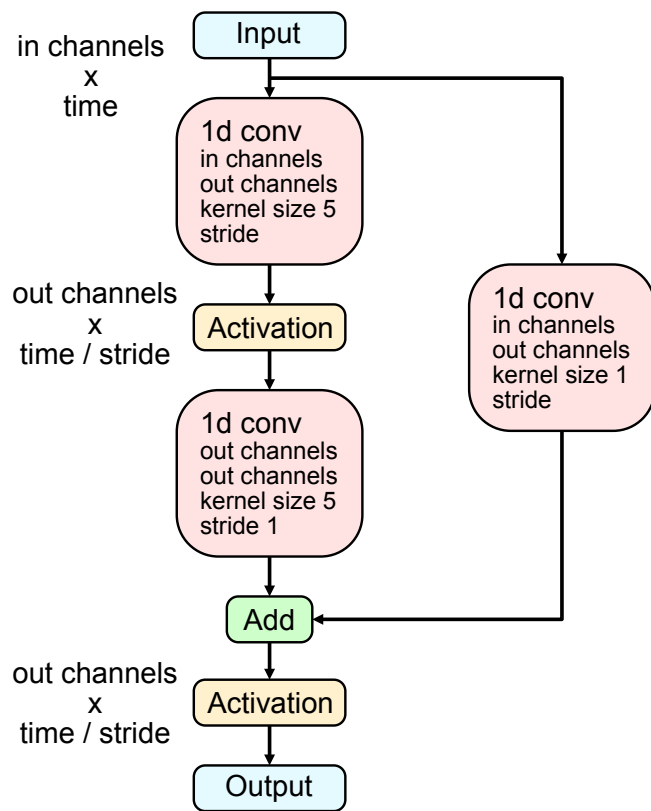


Figure 6.3: Blocks used in the EBM arch

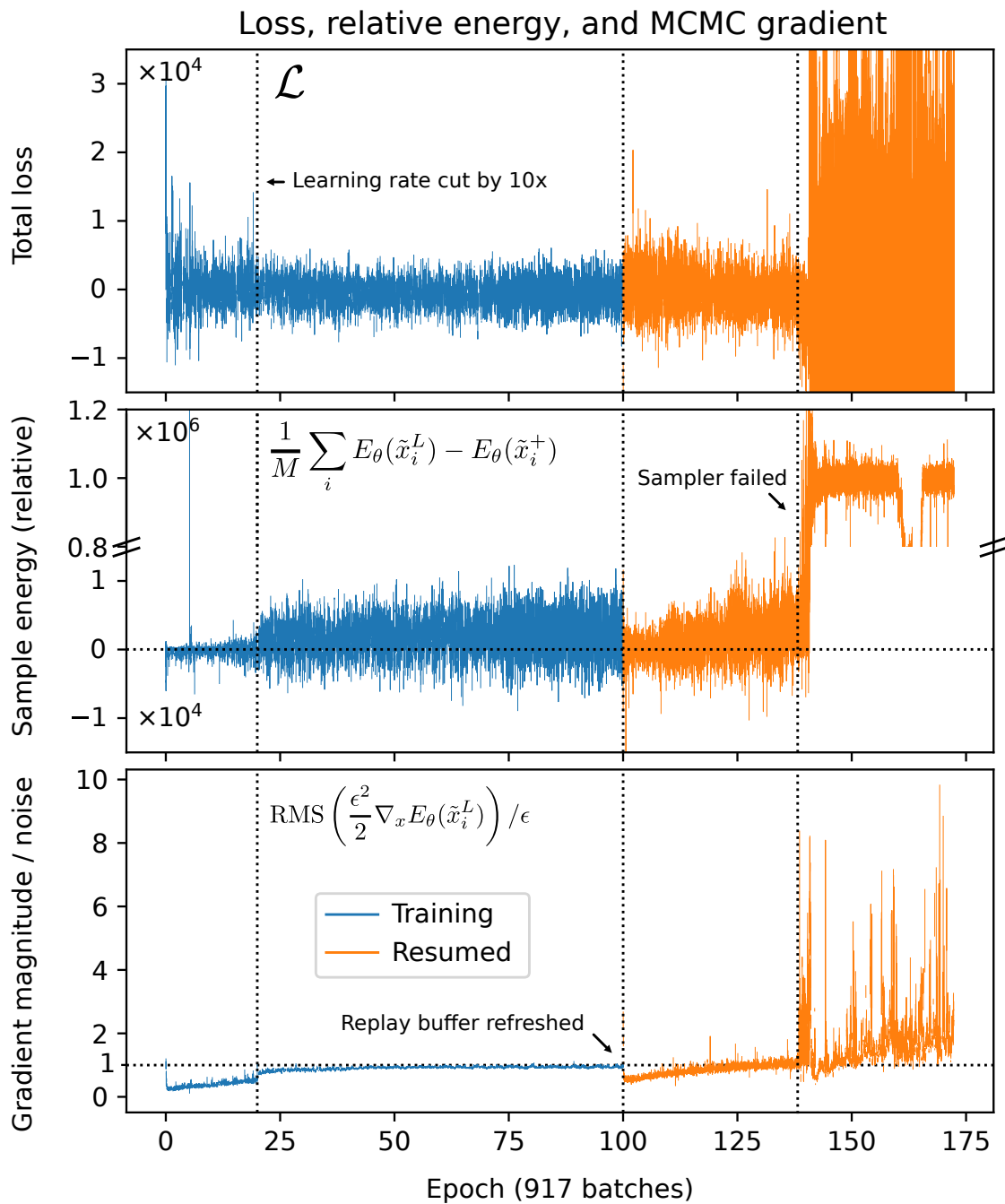


Figure 6.4: Training curves

Distribution of inputs: training data vs unconditional samples

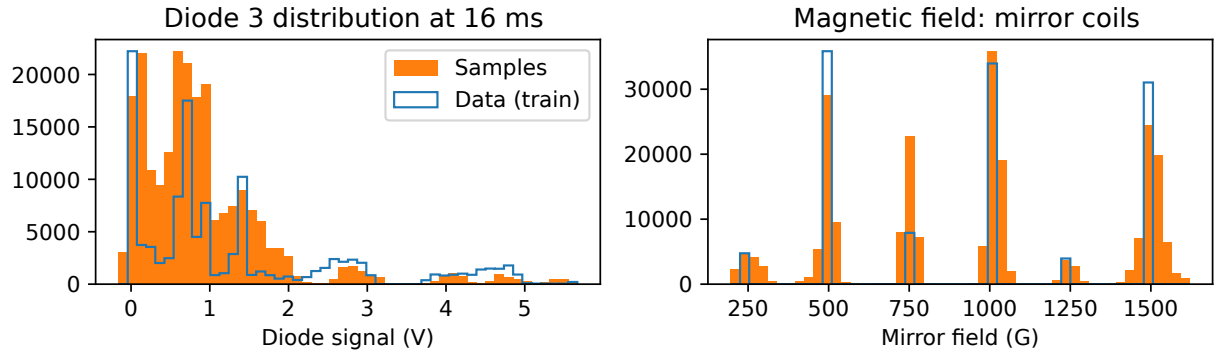


Figure 6.5: Unconditional samples of diode 3 at 16 ms and the mirror coil magnetic field inputs, chosen as representative examples. The EBM learns all modes of the distributions, though the probability mass is not well-aligned.

Distributions: training data vs unconditional samples

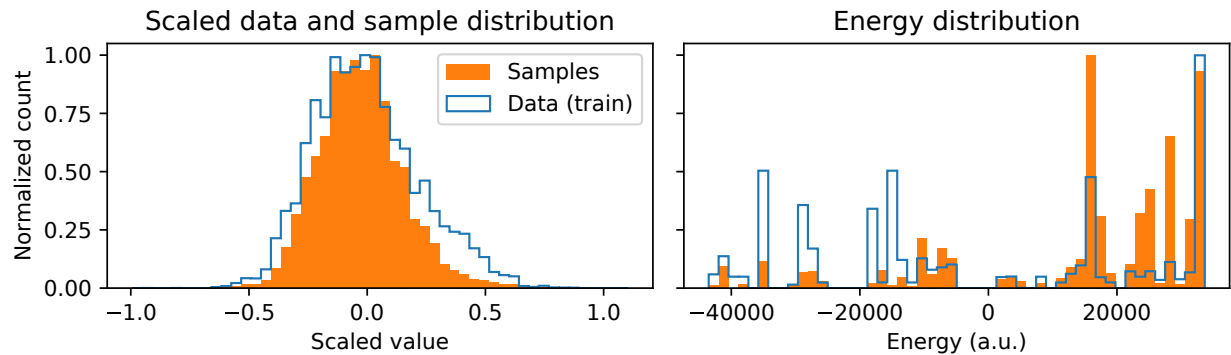


Figure 6.6: Left: all scaled inputs from the training set vs samples inputs. The distributions are similar, but the EBM does not appear to learn more extreme values. Right: corresponding energy distribution. The EBM learns all the modes, but the probability mass is not properly distributed.

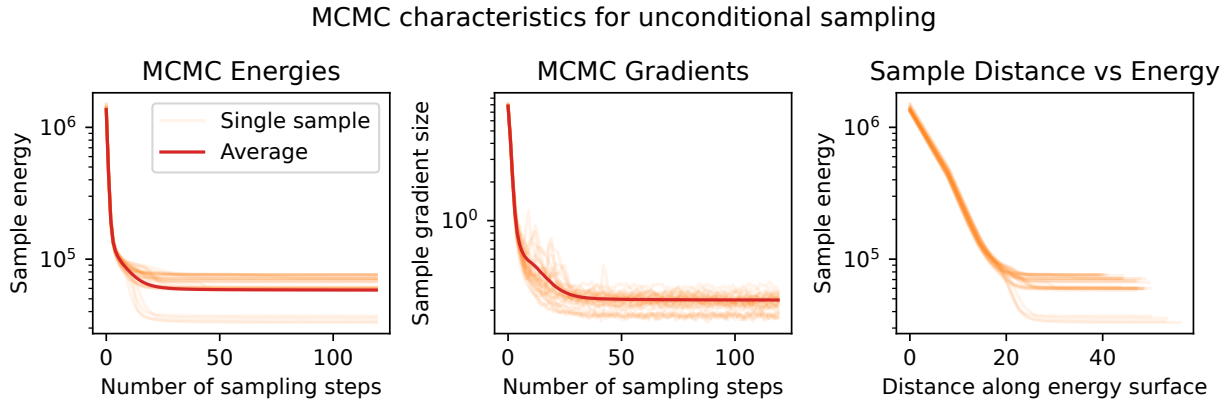


Figure 6.7: MCMC energies, gradients, and integrated trajectory length for unconditional samples. Left: the model converges after approximately 50 sampling steps. Middle: the gradients approach an asymptote; long-term samples are realistic. Right: integrated trajectory length show that individual MCMC trajectories vary in total distance traveled along the energy surface.

series, but that actually harms test-set MSE performance. The constraint used was a quadratic increase in energy when the values go negative, multiplied by 20000 or so to match the relevant energy scale. When using 30 sample steps, the test set MSE went from 2.3e18 to 2.75e18, compared to the 4.40e17 on the training set.

Some interferometer signals looked pretty good, and some were awful: it was kind of all over the place. This was with zero gradients for non-interferometer features.

The  $I_{\text{sat}}$  time trace index used to provide the data did not make too much of a difference. The MSE varied from 2.09e18 to 2.41e18 but the the time series of the predicted interferometer signals did not appreciably change.

The interferometer signals look way better when the other diagnostic signals are sampled as well. Sampling all time-series outputs (all except discharge voltage), the MSE is around 2.37e18. The MSE on the test set also improves to 2.25e18 when signals are all constrained to be positive.

Conditional sampling is far worse when the gradients are limited. Freezing a much smaller subset (e.g., only inputs) leads to much better samples. This results suggests that, if freezing

Comparison of different conditional sampling methods for the interferometer (DR2\_02)

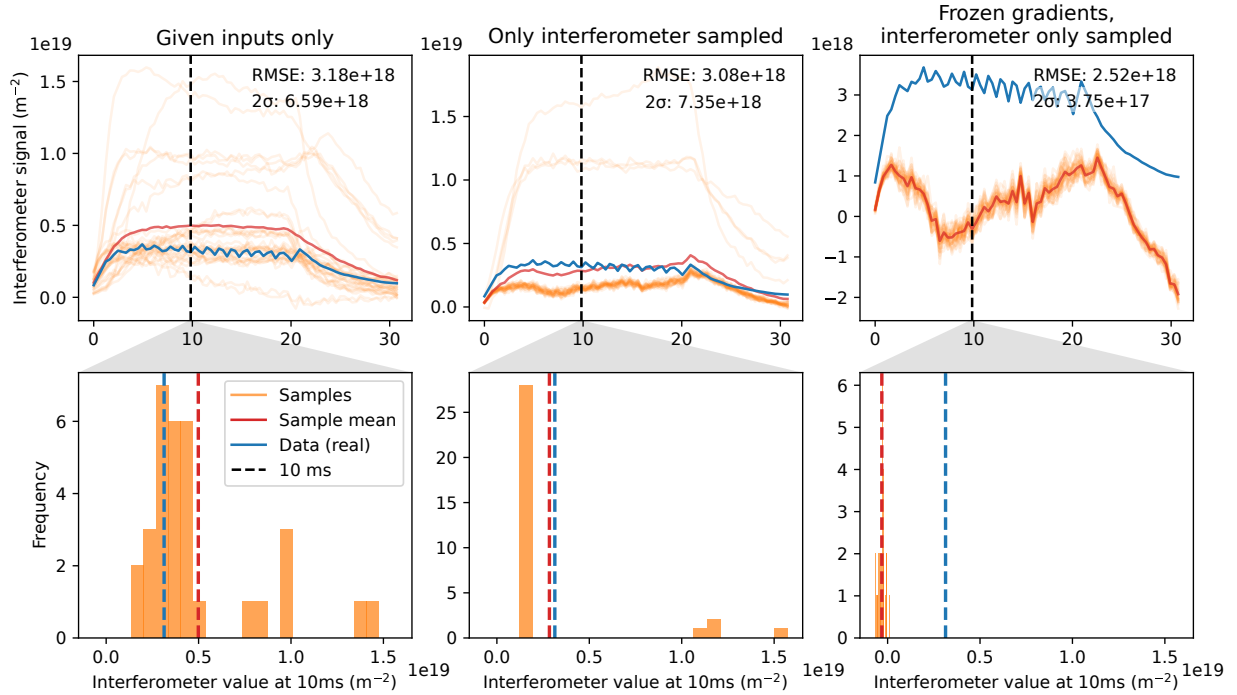


Figure 6.8: Reconstructing the interferometer signal for a test-set datarun. Given only the inputs (left), the interferometer signal reconstruction uncertainty is quite large with many possible modes. When given other diagnostics signals, the RMSE improves by  $1 \times 10^{17} \text{ m}^{-2}$ , but the uncertainty increases. If the model is sampled by instead initializing all inputs on real data and freezing the gradients (right), the model produces unphysical results and is poorly calibrated. The datarun chosen (DR2\_02) is representative of performance across the test set.

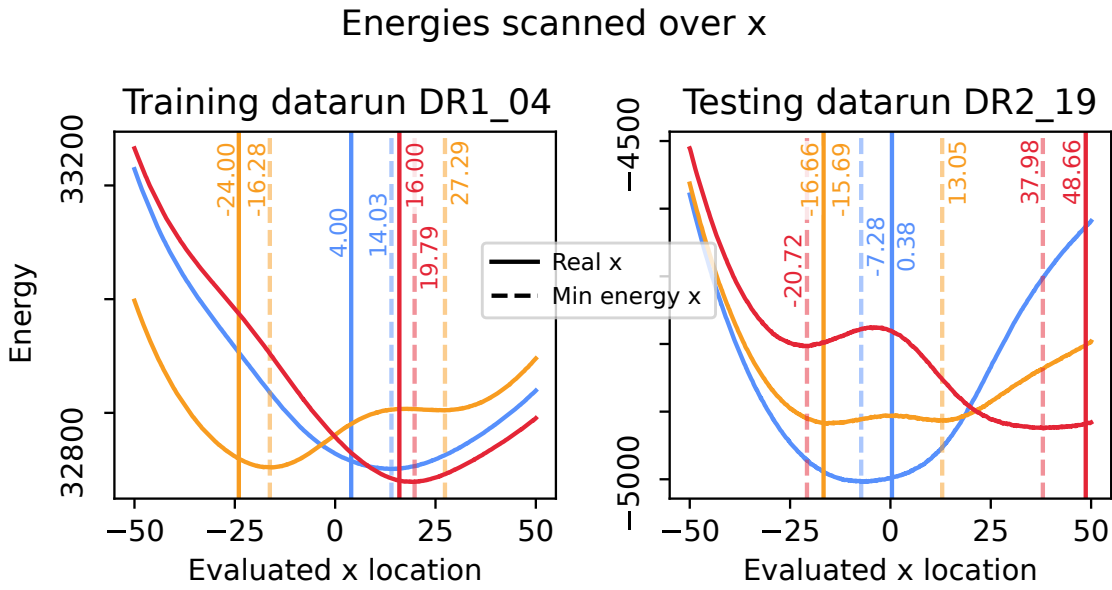


Figure 6.9

gradients is to be performed at inference time, then training with energy-gradient dropout may be necessary.

Imposing a quadratic energy function centered on the data works pretty well. Quadratic leads to good sample diversity (interpreted as a Gaussian). An absolute value energy function instead leads to much sharper samples, as expected. The minimal width (interpreted as a standard deviation) appears to be  $\epsilon^2$ , which makes sense .

## 6.6 Symmetries and trends in the energy function

### 6.6.1 Positional symmetry

## 6.7 Future work

The energy surface gradients in MCMC could be broken down on a per-input basis so that each input has its own step size. Adaptive step sizes could also be used. Despite scaling the step size to

the lowest standard deviation, the distribution of inputs are multimodal, so the standard deviation along one input may be much greater than the standard deviations of the modes in that input. For example, the flags (off or on) have a standard deviation of zero for each mode, but have a nonzero standard deviation when scaled according to the mean and peak-to-peak values. Data augmentation may be useful here to artificially spread the size of these delta-function inputs.

High-dimensional, multimodal inputs on EBMs have been relatively unexplored. Multimodal inputs introduce new challenges to the sampler. The importance of each input on the gradient is no longer identical – some parameters are more important (e.g., field strength) than, say, a single time step of the diode signal.

This work could be extended with more randomly-sampled data from the Large Plasma Device

Curriculum learning could be an interesting way to improve model stability and distribution similarity (between the training data and sampled data).

This model can be composed with another EBM trained on an auxiliary dataset to improve model performance across different LAPD modes of operation.

# **CHAPTER 7**

## **Conclusions**

### **7.1 Future Directions**

## **APPENDIX A**

### **Evidence for the interchange instability in the LAPD**

## **APPENDIX B**

### **Acquiring a 29 million shot dataset for machine learning**

The goal here is to show that diagnostics can be reconstructed from other diagnostics and machine state information (MSI) using energy-based models (EBMs). This is the first time that EBMs have been used and possibly the first time diagnostics reconstruction has been attempted using neural networks in a magnetized plasma context. The bulk of this work was performed in 2021 and 2022.

#### **B.1 Brief introduction to energy-based models (EBMs)**

#### **B.2 Building a 15 million shot dataset**

The LAPD has a set of permanent diagnostics and machine state information (MSI) that is produced but was not recorded for every shot. I built out a diagnostics pipeline that would record the following for every single shot, continuously:

1. Discharge current (time series)
2. Discharge voltage (time series)
3. 56 GHz interferometer (time series)
4. Five axially spaced photodiodes, one having a He-II filter (time series)
5. RGA and total gas pressures (single point for each mass)
6. Magnetic field profile

These data were recorded so that the shots could be synchronized with the data acquisition system used for probe measurements. A plot of a couple of shots can be seen in fig. ??.

These diagnostics and MSI have some particular characteristics. The discharge current may not be accurate based on how the value is measured. The interferometer skips when the plasma density gets too high and the signal cannot be recovered. However, the interferometer signal is still included because these fringe skips (and timing thereof) contain information about the plasma density evolution, though the numerical value may be difficult to acquire. The diodes are not absolutely calibrated, have a nonlinear response, and are not restricted to the visible spectrum. The RGA takes a minute or two to sweep, so partial pressures are not necessarily exact for the particular shot it is recorded. The magnetic field profile is calculated, not measured, so some field measurements may be incorrect if the state of a magnet power supply is recorded incorrectly, or if the source field currents were not manually updated. Despite all these issues, we proceed.

TODO: Plot of example data

This system recorded shots continuously, capturing a wide variety of LAPD machine conditions and experiments. Some particular challenges with this dataset was that other important information was not recorded in an orderly way. The north LaB6 source current and voltage time traces were not recorded even though the north source parameters could have a significant impact on the behavior of the plasma. The locations of large antennas or obstructions were also not recorded conveniently: retrieving this information would require manually opening and reading many experimental datarun files, but that only corresponds to probe data. In general this information was not recorded between dataruns.

In addition, the data may be highly biased towards a particular set of cases. The LAPD was often left as-is without changing parameters for considerable lengths of time, either between dataruns or campaigns, or in general for a particular experiment week. Thus, the data collected may not contain sufficient diversity to learn trends well, particularly with important machine state information not recorded.

The general cathode (and thus plasma condition) was also left unquantified. Variation emissivity across the cathode could lead to considerable changes across the plasma column, and the discharge characteristics could drift over time. This unquantified drift in plasma conditions further makes this dataset a difficult training target, given that the same machine configuration could lead to multiple types of plasma.

TODO: show plot of long-term trends of the discharge current and density changing.

### **B.3 Training the model**

### **B.4 Unconditional sampling**

### **B.5 Reconstructing missing diagnostics via conditional sampling**

### **B.6 Inferring trends and outlook**

## APPENDIX C

### 0D mirror optimization

1. **problem:** Main things that need to be done: find references and double check the equations
2. **problem:** Power to central cell isn't accounted for in plug temperature calulations — fudge factor is used
  
1. **TODO:** Check that DT alpha orbit is contained
2. **TODO:** Add HHFW heating to increase Einj above Ebeam
3. **TODO:** Add neutron dpa
4. **TODO:** Implement assumption calculations for FLR effects and the paraxial approximation
5. **TODO:** Add FLR stabilization estimate (Eq 38 in "Magneto-hydrodynamically stable[...]", Ryutov 2011)
6. **TODO:** Add neutral beam shine through as a condition for plasma density
7. **TODO:** Compare to baseline in section 7 of Egedal et al 2022 [EEF22]
8. **TODO:** Implement beta-enhanced mirror ratio limits from diamagnetic-bubble paper. Beta-enhanced mirror ratio flag?
9. **TODO:** Add "tail wagging" stabilization power cost
10. **TODO:** Calculate stability thresholds and growth rates

## C.1 List of assumptions / conditions

There are many issues and assumptions with this analysis (in no particular order):

1. Powers and particles are not strictly balanced in tandem mirrors
2. Thermal barriers are ignored which may be very important for a practical reactor
3. A fudge factor is used for electron temperatures when plug electrons are heating the central cell
4. Macrostability is not considered
5. Microstability is not considered
6. Plug confinement time is not self-consistent with plug temperatures
7. Effects of field ripple are not calculated
8. T-T and T-He3 reaction rates are not considered
9. Radial transport is assumed to be only classical
10. Cat-DD assumes instant burnup of products which is unreasonable, particularly at the high ion energies needed in mirror reactors
11. Impurities are assumed to be zero
12. Heating and magnet costs are not justified
13. All fusion power exits the plasma immediately (charged particles are collected by the direct-energy converter, neutrons absorbed by the blanket)
14. When using the temperature model from Egedal 2022 [EEF22], we assume that the auxiliary power is much less than the beam power ( $P_{aux}/P_{NBI} \ll 1$ ) or else the model may be inaccurate.

Auxiliary power (say, to compensate for classical diffusion losses or additional ECH) can be included in this model but it would require iterative solving.

15. Burnup fraction is sufficiently small that fusion reactions are not a significant loss of fuel (ironically).
16. The DECs collect all ion losses at a fixed efficiency

## C.2 User specified parameters

### C.2.1 Simple mirror endplug

1. Mirror field, plug (T):  $B_{p,m}$
2. Plug (i.e., midplane) cell field (T):  $B_p$
3. Magnet bore/throat radius (m):  $r_b$
4. Plug length (m):  $L_p$
5. Neutral beam energy (keV):  $E_{\text{inj}}$  or  $E_b$
6. Beta limit (critical stability):  $\beta_{\text{limit}}$  (set to 0.8 [KLZ21])
7. Effective species mass (amu):  $\mu$
8. Effective atomic number (account for He and other impurities):  $Z_{\text{eff}}$

The  $\beta_{\text{limit}}$  (discussed in Kotelnikov 2021 [KLZ21]) assumes a stationary plasma (no rotation, no flow out the ends), ignores finite-Larmor-radius (FLR) effects (which stabilize  $m > a^2/L\rho_i$  modes), and uses the paraxial approximation ( $L_m \gg a$ ). It also assumes  $\beta \ll 1$  but this paper shows that these results match up with GDT experiments. The  $\beta_{\text{limit}}$  depends on the radial pressure profile falloff; the faster the falloff, the lower the  $\beta_{\text{limit}}$ .  $L$  is the length from midplane to throat, and  $L_m$  is

the length of the mirror (highest field to lowest, I think). Profile calculations will not be included in a 0D optimization. The relevant assumptions for FLR effects and the paraxial approximation should be calculated and shown in the output to make sure they are not dramatically violated.

### C.2.2 Tandem mirror

Central cell parameters defined below. Simple mirror endplugs are used on either end.

1. Central cell field (T):  $B_{cc}$
2. Central cell to plug density ratio:  $n_{cc}/n_p$
3. Central cell ion to plug electron temperature ratio:  $T_{cc,i}/T_{p,e}$  (assumes Maxwellian)
4. Central cell to plug electron temperature ratio:  $T_{cc,e}/T_{p,e}$
5. Central cell length (m):  $L_{cc}$
6. Electron temperature fudge factor:  $T_{ep, \text{fudge}}$  if electron are heating the central cell. Default value is 0.5

### C.2.3 Engineering parameters

1. Vessel wall radius (with respect to plasma radius):  $a_{\text{wall}} = a_{\text{wall, ratio}} \cdot a_{\text{plasma}}$
2. Blanket thickness:  $d_{\text{blanket}}$
3. Vacuum vessel thickness:  $d_{vv}$
4. Direct Converter Efficiency (used in the mirror exhaust):  $\eta_{DEC}$
5. Thermal to electric conversion efficiency:  $\eta_{TE}$
6. ECH heating efficiency:  $\eta_{ECH}$

7. NBI heating efficiency:  $\eta_{NBI}$

8. RF heating efficiency:  $\eta_{RF}$

Optimizing the blanket and vacuum vessel thickness would probably require some neutronics calculations which would probably depend on the fuel mix, so we're just going to leave those constant in our optimization.

## C.3 Fusion

DT fusion helium energy (keV):  $E_\alpha = 3500$

### C.3.1 Reactivity

DD and DT fusion cross-section parameterizations can be found in Bosch 1992. [BH92]. What we care most about is the fusion reaction rate per unit volume (eq. 10 in the paper):

$$\frac{dR}{dV} = \frac{n_i n_j}{1 + \delta_{ij}} \langle \sigma v \rangle \quad (\text{C.1})$$

This parameterization accepts ion temperature in keV and gives reactivity in  $\text{cm}^3/\text{s}$ :

$$\langle \sigma v \rangle = C1 \cdot \theta \sqrt{\xi / (m_r c^2 T^3)} e^{-3\xi} \quad (\text{C.2})$$

$$\theta = T / \left[ 1 - \frac{T(C2 + T(C4 + TC6))}{1 + T(C3 + T(C5 + TC7))} \right] \quad (\text{C.3})$$

$$\xi = (B_G^2 / 4\theta)^{1/3} \quad (\text{C.4})$$

$$B_G = \pi \alpha Z_1 Z_2 \sqrt{2m_r c^2} \quad (\text{C.5})$$

where  $m_r$  is the reduced mass and  $\alpha$  is the fine structure constant. The coefficients ( $C1$ ,  $C2$ , and so on) are in the paper cited above. This parameterization is valid for  $T_i$  between 0.2 to 100 keV.

**problem:** We will definitely exceed this in our optimization – the extent of the deviation should be quantified. The cross section explodes for DD after roughly 500 keV Max error is 0.25% for DT

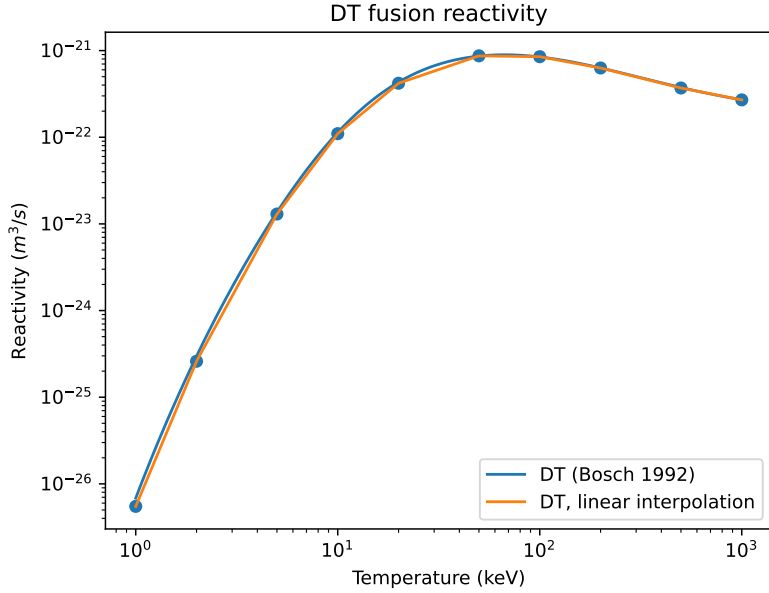


Figure C.1: DT reactivities

and 0.35% and 0.3% for  $DD \Rightarrow p\ T$  and  $DD \Rightarrow n\ He3$ , respectively. phil: We will want to use the cross-section (the parameterization of which goes up to 550 keV for DT in [BH92]) and integrate over ion distribution. Integration over non-Maxwellian ion distributions should be doable if FBIS [EEF22] can give the full distribution. phil: For now I'm just linearly interpolating (in log-log space) between the points provided in the NRL. Comparison plots of the different methods for DD and DT can be seen in figures C.1 and C.2.

### C.3.2 Fusion power

DT fusion reaction rate (#/s):

$$R_{x,DT} = V n_D n_T \langle \sigma v \rangle_{DT} \quad (C.6)$$

If  $n_D = n_T = n/2$ , then this becomes  $V \frac{n^2}{4} \langle \sigma v \rangle_{DT}$

DD fusion reaction rate (#/s):

$$R_{x,DD} = V \frac{n_{\text{plug, D}}^2}{2} \langle \sigma v \rangle_{DD} \quad (C.7)$$

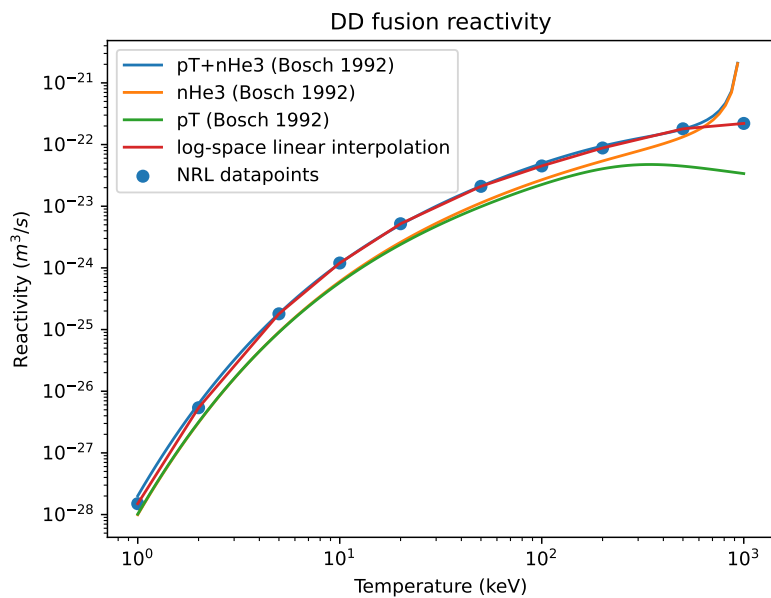


Figure C.2: DD reactivities

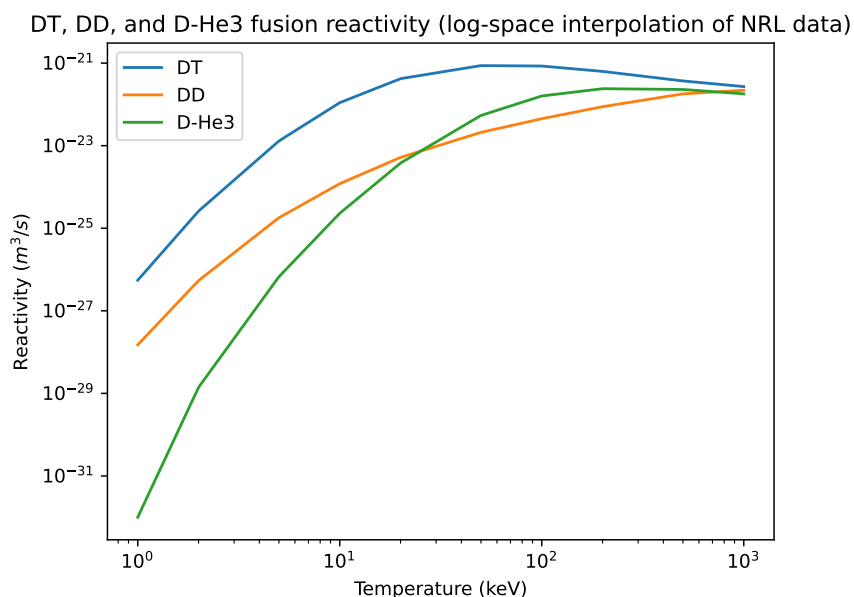


Figure C.3: DT, DD, and D-He3 reactivity comparison

The  $\frac{1}{2}$  factor is to avoid double counting DD reactions.

Fusion power (MW):

$$P_{DT,n} = 14.1 |e| R_{x,DT} \quad (C.8)$$

$$P_{DT,+} = 3.5 |e| R_{x,DT} \quad (C.9)$$

$$P_{DD,n} = 2.45 |e| R_{x,DD} \cdot \frac{1}{2} \quad (C.10)$$

$$P_{DD,+} = (4.02 + 0.82) |e| R_{x,DD} \cdot \frac{1}{2} \quad (C.11)$$

$$(C.12)$$

It's useful to split the power into charged and neutrons because energy is extract from them in different ways. Neutrons provide thermal power, charged particles heat the plasma and/or are directly captured by the DECs. The  $\frac{1}{2}$  coefficient on the DD reactions assumes a 50-50 split on the DD branching ratio which actually varies with energy and may be significant above around 100 keV. If we assume the tritium produced from a DD reaction is burned instantly, then the additional power produced ("catalyed DD") is:

$$P_{cat\ DD,n} = 14.1 |e| R_{x,DD} \cdot \frac{1}{2} \quad (C.13)$$

$$P_{cat\ DD,+} = (3.5 + 18.3) |e| R_{x,DD} \cdot \frac{1}{2} \quad (C.14)$$

$$(C.15)$$

We assume the tritium is burned instantly because the DT reaction rate is much higher than DD and D-He3 fusion up to around 200 keV, after which it's only slightly higher up to around 1 MeV. A more accurate estimate of fusion power would require estimates of D-He3, TT, and T-He reaction rates and density evolution of each species. A plot of reactivities can be found in Fig. C.3. phil:  
I do not know how to do this steady-state calculation in a simple 0d way – perhaps this sort of calculation is left for a more detailed reactor model.

## C.4 General formulae

Electron cyclotron frequency (GHz):

$$f_{\text{ECH}} = \frac{eB}{2\pi m_e c} = 28B \quad (\text{C.16})$$

Ion cyclotron frequency (MHz):

$$f_{ci} = \frac{ZeB}{2\pi m_i c} \quad (\text{C.17})$$

$$f_{ci,D} = 7.63B \quad (\text{C.18})$$

$$f_{ci,T} = 5.09B \quad (\text{C.19})$$

Here,  $Z$  is the charge state of the ion.

Electron plasma frequency (Hz):

$$f_{pe} = \frac{1}{2\pi} \sqrt{\frac{4\pi n_e e^2}{m_e}} = 8.98 \cdot 10^3 \sqrt{n_{\text{plug}}} \quad (\text{C.20})$$

Ion plasma frequency (Hz):

$$f_{pi} = \frac{1}{2\pi} \sqrt{\frac{4\pi n_i Z^2 e^2}{\mu m_p}} \quad (\text{C.21})$$

$$f_{pi,D} = 2100 \sqrt{\frac{n_{\text{plug}}}{2}} \quad (\text{C.22})$$

$$f_{pi,T} = 2100 \sqrt{\frac{n_{\text{plug}}}{3}} \quad (\text{C.23})$$

Here,  $\mu$  is the mass of the ion in proton mass units (e.g.  $\mu_{\text{Deuterium}} = 2$  and  $\mu_{\text{Tritium}} = 3$ ).

Lorentz factor ( $\gamma$ ):

$$\gamma = \sqrt{1 + \frac{T_e}{m_e c^2}} = \sqrt{1 + \frac{T_e}{511 \text{keV}}} \quad (\text{C.24})$$

Ion thermal velocity:

$$v_{Ti} = 97900 \sqrt{\frac{10^3 E_{\text{ion}}}{\mu}} \quad (\text{C.25})$$

Ion gyroradius: problem: Cary's spreadsheet uses the temperature to calculate this but calls it " $E_{ion}$ ". I think temperature should be used to accurately account for the energy in  $v_{perp}$

$$\rho_i = \frac{mv_{\perp}}{qB} = 3.22 \cdot 10^{-3} \frac{\sqrt{\mu E_{ion}}}{B_p} \quad (\text{C.26})$$

Whistler wavelength:

$$\lambda_{\text{whistler}} = \sqrt{\frac{2\pi\Omega_e c^2}{\Pi_e^2 f}} \quad (\text{C.27})$$

$$\lambda_{\text{whistler}} = \sqrt{\frac{90 f_{\text{ECH}}}{f_{pe}^2 f_{D,2\text{nd Harmonic}}}} \quad (\text{C.28})$$

The 2nd formula is what appears on the spreadsheet and is used to estimate the size of the RF wave used for HFW as compared to the size of the plasma. It takes into account the various constants and units used in the spreadsheet.

Collision rates (from NRL):

$$v_e = 2.91 \cdot 10^{-6} \frac{n_e \ln \Lambda}{T_e^{3/2}} \quad (\text{C.29})$$

$$v_i = 4.80 \cdot 10^{-8} \frac{Z_{\text{eff}}^4 n_i \ln \Lambda}{\mu^{1/2} T_i^{3/2}} \quad (\text{C.30})$$

These can be rearranged to give the following collision times (s): problem: this seems to assume  $\log \Lambda = 20$  (should be doubled check but doesn't probably make much of a difference – comparing to eq 4.8 in [Bal77]). problem: Depends on  $Z_{\text{eff}}$  which isn't accounted for during optimization/power balance. phil: Technically we should use  $T = \frac{2}{3}E_{ion}$  for the central cell since the distribution is likely approximately Maxwellian, but it only changes  $\tau_{ii}$  by a factor of 1.8.

$$\tau_{ee} = 10^{-4} \frac{T_e^{3/2}}{n_{20} \lambda_{ee}} \quad (\text{C.31})$$

$$\tau_{ii} = 1.25 \cdot 10^{-4} \frac{\mu^{1/2} E_{ion}^{3/2}}{n_{20} Z_{\text{eff}}^4} \quad (\text{C.32})$$

Slowing down times [Dol82] phil: I assume Z is Zeff? Need to double check. I put it as Zeff in the ipynb :

$$\tau_{i,\text{slow}} = 0.1 \frac{\mu T_e^{3/2}}{n_{20} Z^2 \lambda_{ei}} \quad (\text{C.33})$$

$$\tau_{i,\text{fast}} = \left( \left( \tau_{ii} 0.4 \log \frac{R_m}{\sqrt{1-\beta}} \right)^{-1} + \frac{1}{\tau_{\text{slow}}} \right)^{-1} \quad (\text{C.34})$$

Here, we can write  $Z = 2$  for alpha particles. The 2nd equation comes from substituting the expression for  $T_e$  in a purely NBI heated case seen above.

Coulomb logarithms:

$$\lambda_{ee} = 23.5 - 0.5 \ln n_e + 1.25 \ln T_e - \left( 10^{-5} + \frac{(\ln T_e - 2)^2}{16} \right)^{1/2} \quad (\text{C.35})$$

$$\lambda_{ei} = 24 - 0.5 \ln n_e + \ln T_e \quad (\text{C.36})$$

$$\lambda_{ii,\text{Cary}} = 31 - 0.5 \ln n_e + \ln T_e \quad (\text{C.37})$$

$$\lambda_{ii,\text{NRL}} = 23 - 0.5 \ln n_e + 1.5 \ln T_i \quad (\text{C.38})$$

The formula for  $\lambda_{ee}$  is from NRL. The formula for  $\lambda_{ei}$  is from NRL. However, the plasma does not fit into any of the 3 limiting cases described in the formulary. We have picked the formula based on the condition that is violated the least severely. There are 2 formulas for  $\lambda_{ii}$ . They do not have a large disagreement in the ranges of  $T_e$  and  $T_i$  of interest.

## C.5 Radial particle transport

As of the time of writing, diffusive radial transport in mirror reactors appears to be an open question. The goal here is to provide reasonable estimates of radial particle loss and how each scale, not necessarily going for high-accuracy predictions (though being close would be nice!)

### C.5.1 Classical diffusion

Assuming Fick's law and a linear density gradient from  $3n$  to 0 (from Chen 5.8):

$$\tau_{\text{classical}} = \frac{nV}{A \cdot \Gamma} = \frac{na}{-2D_{\perp} \nabla n} \quad (\text{C.39})$$

where  $D_{\perp}$  is defined as

$$D_{\perp} = \eta_{\perp} n \sum T / B^2 \quad (\text{C.40})$$

and the parallel and perpendicular conductivities are

$$\eta_{||} = 5.2 \cdot 10^{-5} \frac{Z \ln \Lambda}{T^{3/2}} \quad (\text{C.41})$$

$$\eta_{\perp} = 2 \cdot \eta_{||} \quad (\text{C.42})$$

Combining all of this together gives

$$\tau_{\text{classical}} = \frac{a^2 B^2 T_e^{3/2}}{3.12 \cdot 10^{-4} \cdot n Z \sqrt{\mu} \ln \Lambda \sum T} \quad (\text{C.43})$$

### C.5.2 Bohm diffusion

**phil:** I don't like how pessimistic the estimates are for this are. Reasonable values gets you 500  $\mu$ s confinement times for Bohm diffusion. Bohm diffusivity:

$$D_{\text{Bohm}} = \frac{1}{16} \cdot \frac{T_{i,cc} \cdot 10^3}{B_{cc}} \quad (\text{C.44})$$

Normalized gyroradius (assuming deuterium):

$$r_{\text{Larmor}} = \frac{\sqrt{2mE_{\perp}}}{2eB_{cc}} = \frac{0.00791 \sqrt{T_{i,cc}}}{B_{cc}} \text{ cm} \quad (\text{C.45})$$

$$\rho^* = \frac{r_{\text{Larmor}}}{a_{cc}} \quad (\text{C.46})$$

Again, using Fick's law and assuming a linear density gradient from  $3n$  to 0 (so that total particle number remains  $n \cdot V$ ), cross-field particle flux is:

$$\Gamma = -D_{\text{Bohm}} \cdot \nabla n_e \quad (\text{C.47})$$

$$= \frac{1}{16} \cdot \frac{T_{i,cc} \cdot 10^3}{B_{cc}} \cdot 3n_i \quad (\text{C.48})$$

which implies a characteristic confinement time of

$$\tau_{\text{Bohm}} = N_{\text{tot}} \left/ \frac{dN}{dt} \right. = n_i \cdot V / (\Gamma * A) \quad (\text{C.49})$$

$$= n_i \cdot \pi a^2 L \left/ \left( \frac{1}{16} \cdot \frac{T_{i,cc} \cdot 10^3}{B_{cc}} \cdot 3n_i \cdot 2\pi a_{cc} L \right) \right. \quad (\text{C.50})$$

$$= \frac{8aB_{cc}}{3T_{i,cc}10^3} \quad (\text{C.51})$$

### C.5.3 Gyro-Bohm diffusion

The gyro-Bohm scaling assumes cross-field transport is dominated by small ion-gyroscale turbulence. Though commonly used for tokamak scaling laws, we should be able to get some rough estimates for mirrors. Right now it can be estimated by just diving the Bohm confinement time by the normalized gyroradius  $\rho^*$ . The gyro-Bohm estimate is then:

$$\tau_{\text{gyro-Bohm}} = \frac{8aB_{cc}}{3T_{i,cc}10^3} \cdot \frac{1}{\rho^*} \quad (\text{C.52})$$

The  $\frac{1}{\rho^*}$  factor can boost the confinement time estimate by a factor of 50-100. phil: But the confinement times still seems a little low.

### C.5.4 ETG-driven transport

Cary's spreadsheet says phil: (I'm having trouble finding a derivation or hand-wavy justification)

:

$$\chi_{\text{ETG}} = 0.1 \frac{T_{e,cc}^{3/2}}{B_{cc}} \quad (\text{C.53})$$

$$\tau_{\text{ETG}} = \frac{a_{cc}^2}{\chi_{\text{ETG}}} \quad (\text{C.54})$$

## C.6 Mirror-specific derived quantities

### C.6.1 Temperatures and confinement time in a beam-heated mirror from Egedal et al 2022 [EEF22]

Electron and ion temperature (keV) via pure beam heating [EEF22]: we must solve a system of equations which considers the power balance of the machine. The ion temperature, given by eq. 22 in [EEF22] is:

$$\frac{3}{2} \frac{T_i}{E_{beam}} = \frac{\exp(-\alpha) - \alpha \Gamma(0, \alpha)}{\Gamma(0, \alpha)} \quad (\text{C.55})$$

Note that eq. 22 in [EEF22] is missing a factor of  $\alpha$  in the numerator in front of the  $\Gamma$  function. The electron temperature can be found in terms of  $T_i$  and  $\alpha$  by rearranging the definition of  $\alpha$  (eq 21):

$$\frac{T_e}{E_{beam}} = \left( \frac{T_i}{E_{beam}} \frac{2}{3} \frac{\alpha^2 \ln R_m^2}{(22.4)^2} \right)^{1/3} \quad (\text{C.56})$$

These can be solved for with the help of a power (really energy-per-particle) balance equation (eq. 24 in [EEF22]):

$$E_{beam} + p_{aux} = T_i + 6T_e \quad (\text{C.57})$$

where  $p_{aux}$  is the combined sources and losses, such as alpha-particle heating, plasma heat losses, RF heating, radial transport, and so on. By balancing the power lost with auxiliary heating power we can keep  $p_{aux} = 0$  to avoid iteratively solving this equation. Each ion loses  $T_i + e\Phi \approx T_i + 5T_e$  units of energy and each electron loses  $\approx T_e$  units because only hotter electrons can surmount the ambipolar potential.  $p_{aux}$  isn't so much a power as it is the energy gained/lost per particle – an actual power would require evaluation of the confinement time (eq 29 in [EEF22]):

$$\tau_p = \tau_{Ti}^{90} \frac{1}{\alpha_1 \lambda_1} \frac{\mathcal{H}}{T_i/E_{beam}} \int_0^1 M_1(\xi) d\xi \quad (\text{C.58})$$

where  $\tau_{Ti}^{90}$  is the "scattering reactivity",  $\alpha_1$ ,  $\lambda_1$ , and  $M_1$  are the normalization value, eigenvalue, and eigenfunction of the Lorentz scattering operator (eq 4 in [EEF22]). phil: I can't be bothered

to write a differentiable solver for the confinement time right now so we're just going to use the values of  $\tau_{\text{Fowler-Baldwin}}$  for the first rough optimizations (which Cary says will give pessimistic estimates (actually, not sure)). By particle conservation and because NBI will be the dominant fueling mechanism, confinement time relates to density and beam current by:

$$\tau_p = eVn_b/I_{\text{NBI}} \quad (\text{C.59})$$

For ion temperature, Cary's spreadsheet says:

$$T_i = \frac{2}{3}E_{\text{inj}} \quad (\text{C.60})$$

This emerges from the relation that  $E = \frac{1}{2}k_B T$  for every degree of freedom. For single particles, we assume 3 degrees of freedom to get  $E = \frac{3}{2}T$  where T is expressed in eV. problem: If referencing Egedal et al 2022 [EEF22], this is only true if the electrons are very hot, i.e.,  $T_e(\log R_M)^{2/3}/E_{\text{inj}} \approx 1$ . However, it is also shown in the paper that  $T_i/E_{\text{inj}} \sim 0.6$ . Assuming 2/3 is more conservative because a higher temperature means a lower reactivity and thus lower total fusion power at temperatures above 70-ish keV.

For electron temperature, Cary's spreadsheet says:

$$T_e = 0.089E_b \log_{10}(R_p)^{0.4} \quad (\text{C.61})$$

$$= 0.089E_b \log_{10}\left(\frac{R_p}{1-\beta}\right)^{0.4} \quad (\text{C.62})$$

which seems to give a roughly 2x higher electron temperature than the reduced model in Egedal 2022 [EEF22], which means that our estimate will be more optimistic. Kunal: Cary said this comes from working through the energy balance of a beam heated mirror device. Apparently it is in their new paper. I will go over this and figure it out. The  $1 - \beta$  term is from the finite beta corrections to the mirror ratio.

Particle confinement time (Convention:  $R_p = R_m$ ) found in Baldwin's end-loss paper [Bal77] equations 4.14 and 4.13. The same equation can be applied to tandem mirrors with thermal barriers

and plug cells [BL79]. According to Cary, this number will give pessimistic estimates. Equation 4.14 [Bal77] states:

$$n\tau_{\text{Fowler/Baldwin}} = \kappa \times 10^{10} E_b^{3/2} \log R_{\text{eff}} / \log 10 \quad (\text{C.63})$$

where  $[n]$  is  $\text{cm}^{-3}$  and  $[E_b]$  is keV, and

$$R_{\text{eff}} = R_m / (1 + (q\phi/mE_i)) \quad (\text{C.64})$$

For  $90^\circ$  NBI,  $\kappa$  falls between 2.4 and 2.8 according to Fokker-Planck calculations [Bal77]; it would be  $\sim 1.7$  if the ion distribution did not have a loss-cone hole because the average energy is higher.

**problem:** Angled injection can impact this significantly (but ignoring for reduced model optimization) **phil:** I don't understand what this  $(q\phi/mE_i)$  term is. This is a purely classical number – the main loss of ion energy is to electron drag, followed by ion-ion collisions / scattering into the loss cone (ions lost and accelerated by the ambipolar potential can be recaptured by direct energy conversion, but that is not accounted for here). Electrons are chilled by neutral beam injection and lost out the ends of the mirror if their energy exceeds the ambipolar potential.

Converting to  $[n]$  in  $\text{m}^{-3}$ :

$$\tau_{\text{Fowler/Baldwin}} = 2.8 \cdot 10^{16} \frac{E_b^{3/2}}{n_e} \log R_m / \log 10 \quad (\text{C.65})$$

We may also need finite- $\beta$  corrections to the mirror ratio.

### C.6.2 Confinement time given by classical transport

Classical confinement time estimates assumes that transport is dominated by diffusion of gyrocenters via Coulomb collisions (from Chen section 5.8[Che16]). The diffusivity is:

$$D_{\text{classical}} = \eta_{\perp} n \sum T / B^2 \quad (\text{C.66})$$

where the perpindicular conductivity (for hydrogen)  $\eta_{\perp}$  is (temperatures in eV):

$$\eta_{\perp} = 2 \cdot \eta_{\parallel}, \quad (\text{C.67})$$

$$\eta_{\parallel} = 5.2 \cdot 10^{-5} \frac{Z \ln \Lambda_{ei}}{T_e^{3/2}} \sqrt{\mu} \quad (\text{C.68})$$

The confinement time is then (summing over species):

$$\tau_{\text{classical}} = \frac{nV}{A \cdot \Gamma} \quad (\text{C.69})$$

$$= \frac{na}{-2D_{\text{perp}} \nabla n} \quad (\text{C.70})$$

$$\tau_{\text{classical}} = \frac{aB^2}{-2\eta_{\perp} \nabla n \sum T} \quad (\text{C.71})$$

Again assuming a linear radial density profile with a peak of  $3n_i$  to keep the total particle number  $n_i \cdot V$ :

$$\tau_{\text{classical}} = \frac{a^2 B^2 T_e^{\frac{3}{2}}}{3.12 \cdot 10^{-4} \cdot n Z \sqrt{\mu} \ln \Lambda \sum T} \quad (\text{C.72})$$

The aggregate confinement time is then:

$$\tau_{\text{tot}} = \frac{1}{\frac{1}{\tau_{\text{classical}}} + \frac{1}{\tau_{\text{Fowler/Bladwin}}} \quad (\text{C.73})}$$

### C.6.3 End Cells/Plugs

Mirror ratio:

$$R_{\text{plug}} = \frac{B_{p,m}}{B_p} \quad (\text{C.74})$$

Radius at the midplane (mapped from bore radius):

$$a_{\text{plug}} = r_b \sqrt{\frac{B_{p,m}}{B_p}} \quad (\text{C.75})$$

Volume:

$$V_p = L_p \pi a_p^2 \quad (\text{C.76})$$

Total particle number:

$$N_{\text{tot}} = V_p n_{\text{plug}} \quad (\text{C.77})$$

Particles lost per second:

$$\frac{dN}{dt} = \frac{N_{\text{tot}}}{\tau_{\text{Fowler/Baldwin}}} \quad (\text{C.78})$$

Number of gyroradii in the plasma radius:

$$N_{\text{gyro}} = \frac{a_p}{\rho_i} \quad (\text{C.79})$$

Density ( $m^{-3}$ ) at the  $\beta$  limit:

$$n_{\text{plug}} = B_p^2 \frac{\beta_{\text{limit}}}{2\mu_0|e|(T_{\text{ion}} + T_e)} \quad (\text{C.80})$$

Here,  $T_{\text{ion}}$  and  $T_e$  are expressed in eV. This can be found in Wesson page 115. Rolling all the constants together and with  $T_i$  and  $T_e$  in keV:

$$n_{20} = n_{\text{plug}}/10^{20} = B_p^2 \frac{\beta_{\text{limit}}}{0.04(T_{\text{ion}} + T_e)} \quad (\text{C.81})$$

NBI Current (A): phil: This should already account for  $dN/dt$  caused by fusion reactions if we assume that alphas have a similar confinement time? This is the current that the lost particles are reinjected after filtering out ash. Fusion reactions decrease the number of ions so  $N$  will actually be lower at a factor of around  $1 - \text{burnup fraction}$ .

$$I_{\text{NBI}} = |e| \frac{dN}{dt} \quad (\text{C.82})$$

The neutral beam current is enough to replace the particles lost by the end plugs. In reality, this number will be larger since the beam neutrals are ionized via charge exchange as well as ion/electron impact.

Electron heating by fast ions (MW):

$$P_{\text{e heating by fast ions}} = 10^{-3} \frac{I_{\text{NBI}} E_b}{\tau_{\text{slow}}} \quad (\text{C.83})$$

Synchrotron radiation power loss (MW) [Wes87]:

$$P_{\text{synch}} = 6 \cdot 10^{-3} V_p n_{20} T_e \gamma^2 B_p^2 \quad (\text{C.84})$$

Bremsstrahlung radiation power loss (MW) [Wes87]:

$$P_{\text{brem}} = 5.35 \cdot 10^{-3} n_{20}^2 Z_{\text{eff}} \sqrt{T_e} V_p \quad (\text{C.85})$$

Power loss from escaping electrons (MW):

$$P_{e,\text{endloss}} = 10^{-3} (I_{\text{NBI}} + I_{\text{cooling}}) \cdot 7T_e \quad (\text{C.86})$$

$I_{\text{cooling}}$  is non-zero when there is current in the expander/divertor. The  $7T_e$  is because only electrons with an energy greater than the ambipolar potential can escape.

Power loss from escaping fast ions (MW):

$$P_{i,\text{endloss}} = 10^{-3} I_{\text{NBI}} (E_b - T_e) \quad (\text{C.87})$$

Injected NBI Power (MW):

$$P_{\text{NBI}} = 10^{-3} I_{\text{NBI}} E_b \quad (\text{C.88})$$

Injected ECH Power (MW): problem: Roll this into power balance equation (eq 24 in [EEF22]). But this will take considerable effort. phil: Electron endloss power should already be accounted for in the reduced model, but heating from fast ions is not. Synchotron + fast ion heating + Bremsstrahlung must be included in ECH to have a consistent  $T_e$ .

$$P_{\text{ECH}} = \frac{P_{\text{synch}}}{20} + P_{e,\text{endloss}} - (\text{Electron heating from fast ions}) \quad (\text{C.89})$$

Divide by 20 since the plasma recaptures most of the synchrotron losses are reabsorbed.

Lawson Triple Product ( $10^{20}\text{keV}\cdot\text{s}/\text{m}^3$ ):

$$\tau_{\text{Fowler/Baldwin}} n_{20} T_i \quad (\text{C.90})$$

Neutron Flux ( $\text{MW}/\text{m}^2$ ): problem: This should include DD and cat-DD neutrons.

$$\frac{14}{17.6} \frac{P_{\text{plug}}}{4\pi a_{\text{wall}}^2} \quad (\text{C.91})$$

phil: Does DD vs DT neutron flux significantly affect breeding ratios? For 400 keV ion temperatures it could lower the DT TBR requirements by like 10% or so – definitely significant when targeting TBRs of like 1.1. This info can be found on <https://www-nds.iaea.org/exfor/endf.htm>

using the targets LI-6; LI-7, reactions MT-105 and 205: N,T;N,XT, and extending the energy above 10 MeV.

**phil:** Burnup fraction, alpha particle density, and Zeff aren't really used in the optimization anywhere. It'd be tricky to include the effects of alpha particle density because that may change the slowing-down times which effects the power balance of the end plugs and so on. These effects would require time-evolution, which is beyond the scope of this "0D" analysis. We would expect the density and reaction rate error to be on the order of the burnup fraction, because ash can be filtered out and exhausted while the fuel is reinjected.

Burnup fraction:

$$\frac{R_{x,\text{plug,DT}}}{dN/dt} \quad (\text{C.92})$$

$\alpha$  particle density ( $10^{20} m^{-3}$ ):

$$n_\alpha = \frac{I_{\text{NBI}} Q_{\text{plug}} \tau_\alpha E_b}{16 V_p E_\alpha} \quad (\text{C.93})$$

but a more intuitive way of putting it may be **phil:** (need to double check this) :

$$n_\alpha = \frac{\tau_\alpha (R_{x, \text{DT}} + \frac{1}{2} R_{x, \text{DD}})}{V} \quad (\text{C.94})$$

$Z_{\text{eff}}$ : (from Wesson section 2.16 [Wes87]) **phil:** We assume no impurities! :

$$Z_{\text{eff}} = \frac{\sum_j n_j Z_j^2}{\sum_j n_j Z_j} = \frac{n + 4n_\alpha}{n + 2n_\alpha} \quad (\text{C.95})$$

$Q_{\text{plug}}$ :

$$Q_{\text{plug}} = \frac{P_{\text{plug}}}{P_{\text{injected}}} \quad (\text{C.96})$$

**phil:** These quantities below are for a simple mirror. These will be duplicated for a tandem system and will be unused in any optimization since simple mirrors are unlikely to make a compelling reactor.

$P_{\text{electric,in}}$ :

$$P_{\text{electric,in}} = P_{\text{total}} \left( \frac{1}{\eta_{HS}} - \eta_{DC} \left( 1 - \frac{T_e}{E_b} \right) \right) \quad (\text{C.97})$$

$P_{\text{electric,out}}$ : phil: The 0.8 represents the heating contribution from neutrons.

$$P_{\text{electric,out}} = 0.8 \eta_{HS} P_{\text{plug}} \quad (\text{C.98})$$

$Q^*$ : phil: The 0.2 represents the alpha particle contribution. Note that

$$Q^* = \frac{Q_{\text{plug}}}{\frac{1}{\eta_{HS}} - \eta_{DC} \left( 1 - \frac{T_e}{E_b} + 0.2 Q_{\text{plug}} \right)} \quad (\text{C.99})$$

$Q_{\text{electric}}$ :

$$Q_{\text{electric}} = Q^* \cdot 0.8 \cdot \eta_{HS} \quad (\text{C.100})$$

#### C.6.4 Tandem mirror — central cell

Radius at the midplane:

$$a_{cc} = r_b \sqrt{\frac{B_{p,m}}{B_{cc}}} \quad (\text{C.101})$$

Central cell mirror ratio:

$$R_{cc} = \frac{B_{p,m}}{B_{cc}} \quad (\text{C.102})$$

Central cell beta:

$$\beta_{cc} = \frac{2\mu_0|e|n_{cc}(T_{cc,i} + T_{cc,e})}{B_{cc}^2} \quad (\text{C.103})$$

$\beta_{cc} \geq 1$  will lead to an infinite Pastukhov factor, so the  $\beta$ -enhanced mirror ratio  $R_{cc,\text{eff}} = R_{cc} \left( \sqrt{1 - \beta_{cc}} \right)^{-\frac{1}{2}}$  will be limited by keeping  $\beta_{cc} \leq 0.9$ .

In a tandem mirror (without a thermal barrier), we assume that the central cell electrons and plug cell electrons are Maxwellian and in thermal equilibrium, and that the central cell ions are also at the same temperature (Introduction to Tandem Mirror Physics, eq 1-3 (pg 78)):

$$T_{cc,i} = T_{cc,e} = T_{\text{plug},e} \cdot T_{\text{fudge factor}} \quad (\text{C.104})$$

The plug cell electron temperature is reduced by some fudge factor because they are heating the central cell plasma. Since the electrons follow a Maxwellian distribution along field lines, they

follow the Maxwell-Boltzmann relationship, where the potential difference between the plug and central cells are given by:

$$\Phi_i = \Phi_p - \Phi_c = T_{ep} \ln \left( \frac{n_p}{n_c} \right) \quad (\text{C.105})$$

The enhancement in ion confinement time in the central cell is then given by the Pastukhov factor (Pastukhov 1974, eq. 21 [Pas74], Kesner et al. eqs. 1-3 [KGL83]):

$$n_c \tau_i = n_c \tau_{ii} g(R) \frac{\Phi_i}{T_{ic}} \exp \left( \frac{\Phi_i}{T_{ic}} \right) \quad (\text{C.106})$$

where  $g(R)$  is a weak function of the mirror ratio. We assume the  $g(R)$  is:

$$g(R) = \log \left( 2R_{cc} \frac{1}{\sqrt{1-\beta_{cc}}} + 1 \right) \quad (\text{C.107})$$

The ion confinement time is then:

$$\tau_E = \text{Pastukhov} \cdot \tau_{cc,ii} \quad (\text{C.108})$$

$$= \log \left( 2R_{cc} \frac{1}{\sqrt{1-\beta_{cc}}} + 1 \right) \frac{T_{ep}}{T_{ic}} \ln \left( \frac{n_p}{n_{cc}} \right) \left( \frac{n_p}{n_{cc}} \right)^{T_{p,e}/T_{c,i}} \cdot \tau_{cc,ii} \quad (\text{C.109})$$

Since  $T_{p,e} = T_{c,i}$ , this reduces to

$$\tau_E = \log \left( 2R_{cc} \frac{1}{\sqrt{1-\beta_{cc}}} + 1 \right) \ln \left( \frac{n_p}{n_{cc}} \right) \left( \frac{n_p}{n_{cc}} \right) \cdot \tau_{cc,ii} \quad (\text{C.110})$$

Thermal barriers are not considered in this analysis, which enhance the central cell confinement by elevating plug electron temperatures instead of only modifying the plug-central cell density ratio (see Post 1987 eq. 10-110[Pos87]). Thermal barriers require additional heating and ion pumpout methods. If estimates of the power requirements of thermal barriers are available, they can be easily included in this analysis and optimization process.

Power lost from the reactor by central cell particles, per meter (MW, T in keV):

$$P_{cc,loss} = 10^{-3} \pi \cdot a_{cc}^2 n_{cc} \cdot e \frac{3}{2} (T_{cc,i} + T_{cc,e}) / \tau_E \quad (\text{C.111})$$

Since this is axial power lost, it's assumed that this power (at least the ion contribution) is recovered by the DECs.

The power lost can be account for by lowering  $T_e$  by some fudge factor, or re-heating the electrons back up to the self-consistent temperature by injecting ECH:

$$P_{aux,ECH} = P_{cc,loss} \quad (\text{C.112})$$

The central cell will be fueld using cold gas puffing and is ionized and heated by electrons from the plugs. The fueling current is then:

$$I_{cc,fuel} = \frac{dN_{cc}}{dt} = \pi a_{cc}^2 L_{cc} n_{cc} / \tau_E \quad (\text{C.113})$$

Fusion Power per meter (MW/m): phil: here for legacy reasons. In the actual optimization procedure length will be one of the quantities that is optimized

$$P_{fusion} = 17.6 |e| R_x \quad (\text{C.114})$$

Breakeven length:

$$L_{breakeven} = \frac{2P_{\text{plug,injected}}}{P_{\text{fusion per m}}} \quad (\text{C.115})$$

phil: Cary's spreadsheet solves for  $L_{cc}$  given  $Q$  but we probably won't want  $Q$  directly in the cost function since we'll be optimizing for dollar cost or something else that depends on  $Q$ . Central cell length:

$$L_{cc} = Q \cdot L_{breakeven} \quad (\text{C.116})$$

Total fusion power (MW):

$$P_{\text{total}} = 2P_{\text{plug}} + L_{cc} P_{\text{fusion}} \quad (\text{C.117})$$

### C.6.5 Overall power balance and plant power estimates

Total electric power in:

$$P_{\text{electric,in}} = \eta_{ECH} P_{ECH} + \eta_{NBI} P_{NBI} + \eta_{RF} P_{RF} \quad (\text{C.118})$$

Recirculating power:

$$P_{\text{recirculating}} = \eta_{DEC} (P_{\text{fusion,charged}} + P_{cc,i,\text{endloss}} + P_{\text{plug,i,endloss}}) \quad (\text{C.119})$$

Thermal power, ignoring power generated by the blanket (the last term is thermal losses caused by DEC inefficiencies):

$$P_{\text{thermal}} = P_{\text{fusion,neutrons}} + (1 - \eta_{DEC}) \left( \frac{P_{\text{recirculating}}}{\eta_{DEC}} \right) \quad (\text{C.120})$$

Net electric power:

$$P_{\text{electric,net}} = -P_{\text{electric,in}} + P_{\text{recirculating}} + \eta_{\text{thermal}} P_{\text{thermal}} \quad (\text{C.121})$$

$Q$  electric:

$$Q_{\text{electric}} = \frac{P_{\text{recirculating}} + \eta_{\text{thermal}} P_{\text{thermal}}}{P_{\text{electric,in}}} \quad (\text{C.122})$$

### C.6.6 Instabilities

DCLC ratio (need to keep  $\sim 1,000$ ) [KCP17, Pos66]:

$$\text{DCLC ratio} = \left( \frac{f_{pi}}{f_{ci,D}} \right)^2 \quad (\text{C.123})$$

The DCLC ratio must be kept  $\sim 1,000$  as the radial density gradient needed to trigger the DCLC instability is very small ( $I_{\text{gradient}} < 0.01\rho_{g,i}$  for stability). The above condition keeps the plasma radius large enough to prevent radial gradients that are sharper than those needed to trigger the DCLC instability from forming.

Interchange growth rate ( $s^{-1}$ ):

$$\gamma_{\text{interchange}} = \frac{v_{Ti}}{L_p} \quad (\text{C.124})$$

Electron temperature gradient... something problem: need to understand

$$\chi_{\text{ETG}} = 0.1 \frac{T_{cc,e}^{3/2}}{B_{cc}} \quad (\text{C.125})$$

$$\tau_{\text{ETG}} = \frac{a_{cc}^2}{\chi_{\text{ETG}}} \quad (\text{C.126})$$

## C.7 Costs and economics

### C.7.1 Heating

problem: Citations needed

ECH: \$10/W

RF: \$1/W

NBI: \$5/W

### C.7.2 Magnets

problem: Citations needed

kA-turns of coil needed for a given field and radius:

$$I_{\text{kA-turns}} = \frac{2 \cdot B \cdot a}{1000 \cdot \mu_0} \quad (\text{C.127})$$

kA-m of superconductor needed:

$$S = 2\pi R \cdot I_{\text{kA-turns}} \quad (\text{C.128})$$

Cost per kA·m =  $10^{-4}$  M\$ / kA·m

Cost of magnet =  $S \cdot (\text{cost per kA·m})$

Radii of magnet coils needed: phil: The numbers below are from Cary's spreadsheet. I can't quite follow the thought process that went into these – the ones with my highlight are the quantities I'm using. problem: Rethink and justify these.

1. Mirror:  $r_{\text{bore}} + d_{\text{vv}}$  (0.1m) +  $d_{\text{blanket}}$  (0.6m)

phil:  $r_{\text{bore}} \cdot a_{\text{wall, ratio}} + d_{\text{vv}}$  (0.1m) +  $d_{\text{blanket}}$  (0.6m)

2. Plug midplane:  $(a_{\text{wall, ratio}} \cdot a_{\text{plasma}}) + d_{\text{blanket}} + d_{\text{vv}}$  (0.2m)

phil: This will need to change depending on the length of the plug: we may need a solenoid or Maxwell coil instead of just a simple coil to keep

3. Plug divertor: beta limit + 0.2 problem: Doesn't make sense – ignoring for now

4. Central cell:  $(a_{\text{wall, ratio}} \cdot a_{\text{plasma}}) + d_{\text{blanket}}$

phil:  $(a_{\text{wall, ratio}} \cdot a_{\text{plasma}}) + d_{\text{vv}} + d_{\text{blanket}}$

For the central cell solenoid we are assuming a spacing of one coil per meter for diagnostic access. This is an adjustable parameter but will not be optimized because that would require energetic particle confinement estimates for coil ripple. For reference, the MARS study [LPG] had 42 central cell magnets spaced 3.16m apart with an inner radius of roughly 2m which led to 6% field ripple, which I assume is tolerable.

1. Solenoid field:  $B = \mu_0 \cdot n_{\text{cc, turns}} \cdot I$ , where  $n_{\text{cc, turns}}$  is number of turns per coil. This becomes

$$B = \mu_0 \cdot I_{\text{kA-turns}}$$

2. kA-m per meter length (or per coil):  $S_{\text{cc}} = 2\pi a_{\text{cc}} \cdot \frac{B}{\mu_0} \cdot (1/\text{coil spacing})$

## C.8 Optimization constraints

phil: This method doesn't work for constraining the minimum field!

### C.8.1 Midplane fields regularization via alpha particle confinement penalties

If we do not regularize field strengths, then the optimizer will bring the central cell (or plug) magnetic fields to 0 or negative. Only the midplane fields of the central cell and plugs will be regularized because the cost functions of interest tend towards higher reactor performance (and/or lower cost), and thus higher mirror ratios (and less HTS tape). The vacuum vessel should be, at minimum, four alpha gyroradii across. If an alpha is produced in the core, it will reach a distance of two gyroradii if all the energy is perpendicular to the field (aside: this is more likely with

spin-polarized fuels). Doubling the vacuum vessel radius to four alpha gyroradii is the safer bet. The 3.5 MeV alpha gyroradius is:

$$r_{\text{Larmor}} = \frac{\sqrt{2mE_{\perp}}}{2eB} = \frac{0.2694\text{cm}}{B} \quad (\text{C.129})$$

This regularization is enforced as a penalty coefficient on charged particle fusion power as an exponential function of the vessel wall:

$$\mathcal{C}_{\text{power penalty}} = \begin{cases} e^{a_{\text{diff}}/r_{\text{Larmor}}} & \text{if } a_{\text{diff}} > 0 \\ 1.0 & \text{otherwise} \end{cases} \quad (\text{C.130})$$

where  $a_{\text{diff}}$  is the difference between the vessel wall and 4 alpha gyroradii:  $a_{\text{diff}} = 4r_{\text{Larmor}}$ , 3.5 MeV alphas —  $a_{\text{vv}}$ . These particle losses depend on the radial plasma profile and should be simulated and implicitly affect the optimization instead of the explicit penalty as done here. Only the 3.5 MeV alpha gyroradius is considered because it's the largest of all the usual fusion products but we apply the penalty to all fusion products. This penalty aims to be a conservative estimate.

### C.8.2 Kunal's suggestions

**Kunal:** If we want to pursue Cary's NBI only reactor design concept, then we need to use  $\geq 100\text{keV}$  beams since the DT reaction cross section peaks at a center of mass energy of  $\sim 65\text{keV}$ . Currently, Cary is using  $1\text{MeV}$  beams in his code.

I think we should just assume we are shooting for something that is  $Q=10$  and has a usable power out of  $200\text{MW}$ . This should stop our coding analysis from making something dumb like a  $Q=1,000$  reactor which has a total power out of  $5\text{W}$  by just using a very low beam current.

Cary calculates a lot of stuff with regards to the growth rate of various instabilities. Do we have/want to take all/some of the them into account in our optimization? For example, keeping the DCLC parameter at 1,000,

Per Kunal's suggestion we'll be operating under the following constraints:

1. Minimum usable power out-  $200\text{MW}$

2. Maximum NBI energy- 1MeV
3. Maximum Central cell length- 300m
4. Maximum plasma radius- 0.6m
5. Maximum field strength- 25T
6. Maximum beta- 0.8
7. Minimum DCLC ratio- 1000

These constraints will be soft — either a quadratic or exponential penalty for exceeding them — so that the cost function is differentiable.

## C.9 Optimizing mirror configurations

### C.9.1 Gradient descent using SymPy and JAX

Optimization is performed via gradient descent, that is, taking the gradient of some cost function  $\mathcal{C}$  with respect to some input parameter vector  $\vec{x}$ :

$$\vec{x} := \vec{x} - \nabla_{\vec{x}} \mathcal{C} \cdot \lambda \quad (\text{C.131})$$

where  $\lambda$  is the step size. Specific input values can be frozen by multiplying the gradient by a mask.

Equations are defined in SymPy, which are then lambdified to JAX expressions and then compiled by JAX’s just-in-time (JIT) compiler on first run, or when `jax.jit` is called. JAX [jax] calculates the gradients of  $\mathcal{C}$  with respect to  $\vec{x}$  automatically. The step size  $\lambda$  may be tuned; larger step sizes may not be able to be used because propagating gradients through exponential functions in the temperature calculations can be unstable. We also use 64-bit floats so that large values of  $\alpha$  (in the reduced temperature model from Egedal 2022 [EEF22]) remain calculable.

### C.9.2 Example: optimizing Q in a simple mirror

As an example of a simple optimization task, we optimize to increase the  $Q$  of a simple mirror with classical radial transport. In this case,  $Q$  is just fusion power over NBI and ECH power. ECH power is only used to replace Bremsstrahlung and electron cyclotron losses to maintain self-consistent temperatures without requiring iterative solving. D-D fusion products are assumed to be burned instantly, though this only increases fusion power by roughly 7%.

Because the optimal solution is to decrease  $B_p$  until the mirror ratio explodes, we will add a  $1/B_p$  penalty term to keep values reasonable. The cost function is then:

$$\mathcal{C} = -Q + 1/B_p \quad (\text{C.132})$$

This cost function has no meaningful physical interpretation.

For this optimization case, we hold constant auxiliary heating power ( $p_{aux} = 0$  MW), plasma beta ( $\beta = 0.8$ ), mirror bore radius ( $r_b = 0.25$  m), length ( $L_p = 20$  m), tritium fraction ( $T_{frac} = 0.5$ ), and beam energy ( $E_b = 1000$  keV) and optimize only the mirror field ( $B_{pm}$ , T) and central (midplane) field ( $B_p$ , T),  $Z_{eff}$  is assumed to be 1.  $B_p$  is initialized to 6 T, and eight different values of  $B_{pm}$  are initialized between 7 and 20 T.

In this optimization, the step size  $\lambda$  is set to 1. The optimization was run for 1000 steps which was chosen arbitrarily—it doesn't converge in that step range (and we don't expect it to in this case).

Plots of the cost function  $\mathcal{C}$  and the gradient L2 norm for each different configuration can be seen in fig. C.4. The effects of the optimization on the fields  $B_{pm}$  and  $B_p$  can be seen in fig. C.5. The optimization favors lowering  $B_p$  until the regularization cost becomes significant at around step 60. The dramatic increase in mirror ratio leads to greater axial confinement, which decreases NBI current and power, leading to increased  $Q$  and decreased fusion power. Plots of  $Q$  and fusion power can be seen in fig. C.6. The effects of this optimization on the temperatures (or average energy in the ion case) can be seen in fig. C.7. The increased confinement time allows the beam ions more time to slow on the background electrons, decreasing  $T_i$  and increase  $T_e$ . The decreased  $T_i$  decreases D-D reactivity but *increases* D-T reactivity at a faster rate, leading to higher fusion power.

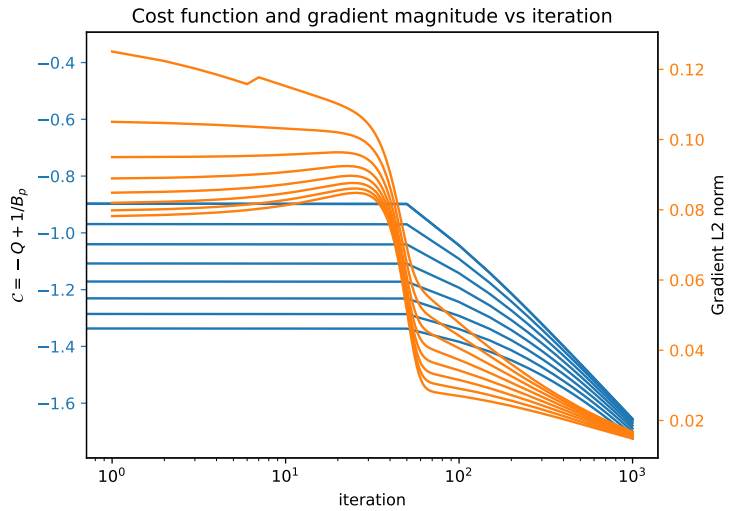


Figure C.4: The cost function and gradient magnitude for each optimization step.

However, the lower density caused by the lower midplane field (as mandated by the  $\beta$  limit) causes a net *decrease* in fusion power. phil: The increased axial confinement time implies increased confinement of fusion alphas. The estimated total fuel burnup fraction  $f_{\text{burnup}} = \frac{2R_x(\text{DT+DD})}{\frac{dN}{dt} + 2R_x(\text{DT+DD})}$  is 24% which may lower fusion power by roughly 42% (since the density would be 24% lower?). Something to think about.

Two insights can be gleaned from this simplified optimization task. Firstly, given optimistic physics, excessively high beam energies, incredibly high field strengths, and ignored impurity and ash accumulation, the reactor still only tops out at Q of around 2.3. This low Q implies that simple mirrors will never be a viable source of electricity. Secondly, Q is a shockingly bad optimization target because it maximizes fusion power *and* minimizes heating power simultaneously, thus high Q's can be obtained at low fusion power as demonstrated here. An expensive, low-power reactor is not useful.

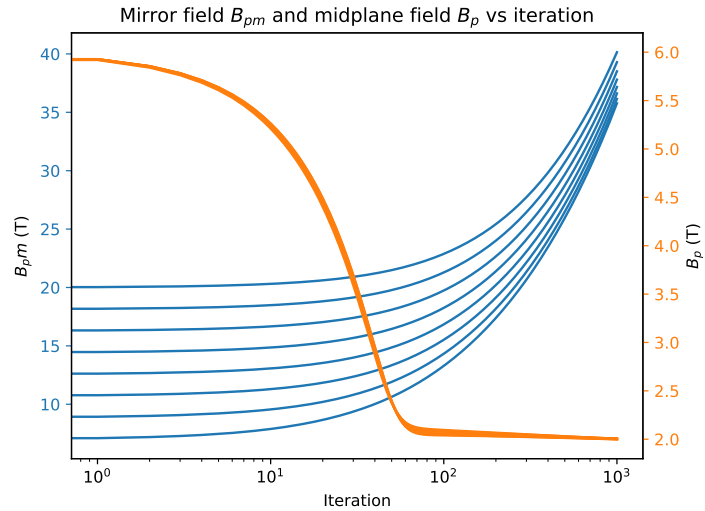


Figure C.5: The mirror and midplane fields for each optimization step. Note the logarithmic x-axis — the rate of increase of the mirror field  $B_{pm}$  with respect to optimization step decreases with iteration.

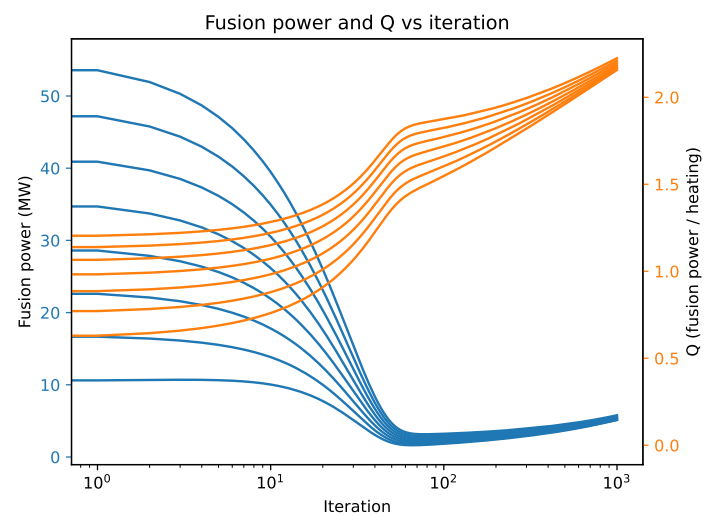


Figure C.6: The total fusion power and Q for each optimization step.

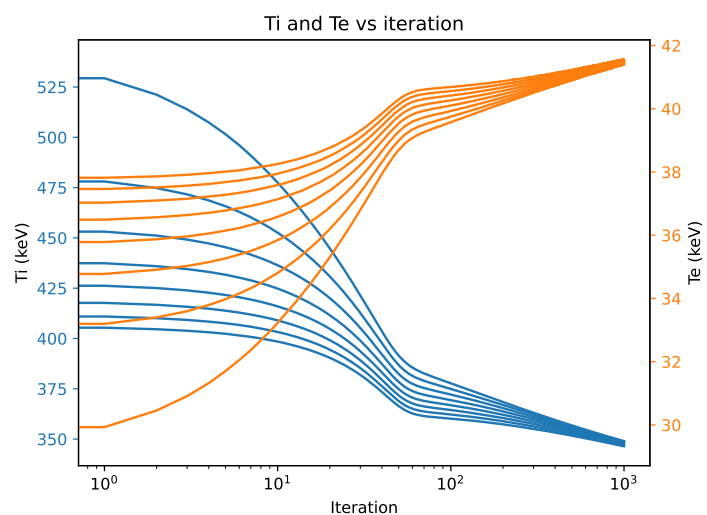


Figure C.7: The ion and electron temperatures for each optimization step

## **APPENDIX D**

**Automated Langmuir sweep analysis using machine learning**

## **APPENDIX E**

### **Wisdom acquired**

1. Simple stuff goes a long way. Try it first
2. Listen to your advisor
3. Write up as you go along. It helps with the thinking too
4. Wrap up projects (or at least get them to a terminal state) as soon as possible
5. Get a dog
6. Nothing really matters
7. Have two simultaneous projects ongoing, not more, not less
8. Good feedback is hard to find. Seek it out
9. Take risks (see item 6)
10. Don't do solo projects
11. Make lots of friends
12. When life gives you lemons, give them to Mel to make lemon bars

## REFERENCES

- [AAA23] Rushil Anirudh, Rick Archibald, M. Salman Asif, Markus M. Becker, Sadruddin Benkadda, Peer-Timo Bremer, Rick H. S. Budé, C. S. Chang, Lei Chen, R. M. Churchill, Jonathan Citrin, Jim A. Gaffney, Ana Gainaru, Walter Gekelman, Tom Gibbs, Satoshi Hamaguchi, Christian Hill, Kelli Humbird, Sören Jalas, Satoru Kawaguchi, Gon-Ho Kim, Manuel Kirchen, Scott Klasky, John L. Kline, Karl Krushelnick, Bogdan Kustowski, Giovanni Lapenta, Wenting Li, Tammy Ma, Nigel J. Mason, Ali Mesbah, Craig Michoski, Todd Munson, Izumi Murakami, Habib N. Najm, K. Erik J. Olofsson, Seolhye Park, J. Luc Peterson, Michael Probst, David Pugmire, Brian Sammuli, Kapil Sawlani, Alexander Scheinker, David P. Schissel, Rob J. Shalloo, Jun Shinagawa, Jaegu Seong, Brian K. Spears, Jonathan Tennyson, Jayaraman Thiagarajan, Catalin M. Ticoş, Jan Trieschmann, Jan Van Dijk, Brian Van Essen, Peter Ventzek, Haimin Wang, Jason T. L. Wang, Zhehui Wang, Kristian Wende, Xueqiao Xu, Hiroshi Yamada, Tatsuya Yokoyama, and Xinhua Zhang. “2022 Review of Data-Driven Plasma Science.” *IEEE Transactions on Plasma Science*, **51**(7):1750–1838, July 2023.
- [ACK21] J. Abbate, R. Conlin, and E. Kolemen. “Data-driven profile prediction for DIII-D.” *Nuclear Fusion*, **61**(4):046027, April 2021.
- [AHS85] D Ackley, G Hinton, and T Sejnowski. “A learning algorithm for boltzmann machines.” *Cognitive Science*, **9**(1):147–169, March 1985.
- [Bal77] D. E. Baldwin. “End-loss processes from mirror machines.” *Reviews of Modern Physics*, **49**(2):317–339, April 1977.
- [BBC10] Alexei D. Beklemishev, Peter A. Bagryansky, Maxim S. Chaschin, and Elena I. Soldatkina. “Vortex Confinement of Plasmas in Symmetric Mirror Traps.” *Fusion Science and Technology*, **57**(4):351–360, May 2010.
- [BBS07] P.A. Bagryansky, A.D. Beklemishev, and E.I. Soldatkina. “Influence of Radial Electric Field on High-Beta Plasma Confinement in the Gas Dynamic Trap.” *Fusion Science and Technology*, **51**(2T):340–342, February 2007.
- [BGB05] F. Brochard, E. Gravier, and G. Bonhomme. “Transition from flute modes to drift waves in a magnetized plasma column.” *Physics of Plasmas*, **12**(6):062104, June 2005.
- [BH92] H.-S Bosch and G.M Hale. “Improved formulas for fusion cross-sections and thermal reactivities.” *Nuclear Fusion*, **32**(4):611–631, 4 1992.
- [BKP82] J. M. Beall, Y. C. Kim, and E. J. Powers. “Estimation of wavenumber and frequency spectra using fixed probe pairs.” *Journal of Applied Physics*, **53**(6):3933–3940, 06 1982.
- [BL79] D. E. Baldwin and B. G. Logan. “Improved Tandem Mirror Fusion Reactor.” *Phys. Rev. Lett.*, **43**:1318–1321, 10 1979.

- [BLL21] Sam Bond-Taylor, Adam Leach, Yang Long, and Chris G. Willcocks. “Deep Generative Modelling: A Comparative Review of VAEs, GANs, Normalizing Flows, Energy-Based and Autoregressive Models.” *arXiv:2103.04922 [cs, stat]*, March 2021. arXiv: 2103.04922.
- [Comment: 21 pages, 10 figures.]*
- [BLZ03] P.A. Bagryansky, A.A. Lizunov, A.A. Zuev, E. Yu. Kolesnikov, and A.L. Solomachin. “Experiments with Controllable Application of Radial Electric Fields in GDT Central Cell.” *Fusion Science and Technology*, **43**(1T):152–156, January 2003.
- [BRT91] H. L. Berk, D. D. Ryutov, and Yu. A. Tsidulko. “Temperature-gradient instability induced by conducting end walls.” *Physics of Fluids B: Plasma Physics*, **3**(6):1346–1354, June 1991.
- [Car24] Davide Carbone. “Hitchhiker’s guide on Energy-Based Models: a comprehensive review on the relation with other generative models, sampling and statistical physics.”, June 2024. arXiv:2406.13661 [cs].
- [CC24] Taoli Cheng and Aaron Courville. “Versatile Energy-Based Probabilistic Models for High Energy Physics.”, January 2024. arXiv:2302.00695 [cs].
- [Comment: 17 pages, 9 figures. NeurIPS 2023 camera ready.]*
- [CCA24] Ian Char, Youngseog Chung, Joseph Abbate, Egemen Kolemen, and Jeff Schneider. “Full Shot Predictions for the DIII-D Tokamak via Deep Recurrent Networks.”, April 2024. arXiv:2404.12416 [physics].
- [Che16] F. Chen. *Introduction to Plasma Physics and Controlled Fusion*. Springer, third edition, 2016.
- [CM09] T. A. Carter and J. E. Maggs. “Modifications of turbulence and turbulent transport associated with a bias-induced confinement transition in the Large Plasma Device.” *Physics of Plasmas*, **16**(1):012304, January 2009.
- [CS82] T. A. Casper and Gary R. Smith. “Observation of Alfvén Ion-Cyclotron Fluctuations in the End-Cell Plasma in the Tandem Mirror Experiment.” *Phys. Rev. Lett.*, **48**:1015–1018, Apr 1982.
- [CYK05] T. Cho, M. Yoshida, J. Kohagura, M. Hirata, T. Numakura, H. Higaki, H. Hojo, M. Ichimura, K. Ishii, K. Md. Islam, A. Itakura, I. Katanuma, Y. Nakashima, T. Saito, Y. Tatematsu, M. Yoshikawa, Y. Kojima, S. Tokioka, N. Yokoyama, Y. Tomii, T. Imai, V. P. Pastukhov, and S. Miyoshi. “Observation of the Effects of Radially Sheared Electric Fields on the Suppression of Turbulent Vortex Structures and the Associated Transverse Loss in GAMMA 10.” *Physical Review Letters*, **94**(8):085002, March 2005.

- [DBO20] Yuntian Deng, Anton Bakhtin, Myle Ott, Arthur Szlam, and Marc’Aurelio Ranzato. “Residual Energy-Based Models for Text Generation.”, April 2020. arXiv:2004.11714 [cs].  
*[Comment: published at ICLR 2020. arXiv admin note: substantial text overlap with arXiv:2004.10188.]*
- [DEH23] Andreas Döpp, Christoph Eberle, Sunny Howard, Faran Irshad, Jinpu Lin, and Matthew Streeter. “Data-driven science and machine learning methods in laser–plasma physics.” *High Power Laser Science and Engineering*, **11**:e55, 2023.
- [DFH23] G A Daly, J E Fieldsend, G Hassall, and G R Tabor. “Data-driven plasma modelling: surrogate collisional radiative models of fluorocarbon plasmas from deep generative autoencoders.” *Machine Learning: Science and Technology*, **4**(3):035035, September 2023.
- [DLD21] Jiaolong Dong, Jianchao Li, Yonghua Ding, Xiaoqing Zhang, Nengchao Wang, Da Li, Wei Yan, Chengshuo Shen, Ying He, Xiehang Ren, and Donghui Xia. “Machine learning application to predict the electron temperature on the J-TEXT tokamak.” *Plasma Science and Technology*, **23**(8):085101, August 2021.
- [DLM19] Yilun Du, Toru Lin, and Igor Mordatch. “Model Based Planning with Energy Based Models.” p. 10, 2019.
- [DLM20] Yilun Du, Shuang Li, and Igor Mordatch. “Compositional Visual Generation and Inference with Energy Based Models.”, December 2020. arXiv:2004.06030 [cs].  
*[Comment: NeurIPS 2020 Spotlight; Website at <https://energy-based-model.github.io/compositional-generation-inference/>.]*
- [DLS21] Yilun Du, Shuang Li, Yash Sharma, Joshua B. Tenenbaum, and Igor Mordatch. “Unsupervised Learning of Compositional Energy Concepts.”, November 2021. arXiv:2111.03042 [cs].  
*[Comment: NeurIPS 2021, website and code at <https://energy-based-model.github.io/comet/>.]*
- [DLT21] Yilun Du, Shuang Li, Joshua Tenenbaum, and Igor Mordatch. “Improved Contrastive Divergence Training of Energy Based Models.” *arXiv:2012.01316 [cs]*, June 2021. arXiv: 2012.01316.  
*[Comment: ICML 2021, Project webpage at <https://energy-based-model.github.io/improved-contrastive-divergence/>.]*
- [DM20] Yilun Du and Igor Mordatch. “Implicit Generation and Generalization in Energy-Based Models.” *arXiv:1903.08689 [cs, stat]*, June 2020. arXiv: 1903.08689.
- [Dol82] Thomas James Dolan. *Fusion research*. Pergamon Press, 1982.

- [DPS23] Bhrugu Dave, Sarthak Patel, Rishi Shivani, Shishir Purohit, and Bhaskar Chaudhury. “Synthetic data generation using generative adversarial network for tokamak plasma current quench experiments.” *Contributions to Plasma Physics*, **63**(5-6):e202200051, June 2023.
- [EAB23] D. Endrizzi, J.K. Anderson, M. Brown, J. Egedal, B. Geiger, R.W. Harvey, M. Ialovega, J. Kirch, E. Peterson, Yu.V. Petrov, J. Pizzo, T. Qian, K. Sanwalka, O. Schmitz, J. Wallace, D. Yakovlev, M. Yu, and C.B. Forest. “Physics basis for the Wisconsin HTS Axisymmetric Mirror (WHAM).” *Journal of Plasma Physics*, **89**(5):975890501, October 2023.
- [EEF22] J. Egedal, D. Endrizzi, C.B. Forest, and T.K. Fowler. “Fusion by beam ions in a low collisionality, high mirror ratio magnetic mirror.” *Nuclear Fusion*, **62**(12):126053, 11 2022.
- [EPC09] E. T. Everson, P. Pribyl, C. G. Constantin, A. Zylstra, D. Schaeffer, N. L. Kugland, and C. Niemann. “Design, construction, and calibration of a three-axis, high-frequency magnetic probe (B-dot probe) as a diagnostic for exploding plasmas.” *Review of Scientific Instruments*, **80**(11):113505, November 2009.
- [FAE24] C.B. Forest, J.K. Anderson, D. Endrizzi, J. Egedal, S. Frank, K. Furlong, M. Ialovega, J. Kirch, R.W. Harvey, B. Lindley, Yu.V. Petrov, J. Pizzo, T. Qian, K. Sanwalka, O. Schmitz, J. Wallace, D. Yakovlev, and M. Yu. “Prospects for a high-field, compact break-even axisymmetric mirror (BEAM) and applications.” *Journal of Plasma Physics*, **90**(1):975900101, February 2024.
- [FCU13] B. Friedman, T. A. Carter, M. V. Umansky, D. Schaffner, and I. Joseph. “Nonlinear instability in simulations of Large Plasma Device turbulence).” *Physics of Plasmas*, **20**(5):055704, 05 2013.
- [FEE20] Yichen Fu, David Eldon, Keith Erickson, Kornee Kleijwegt, Leonard Lupin-Jimenez, Mark D. Boyer, Nick Eidietis, Nathaniel Barbour, Olivier Izacard, and Egemen Kolemen. “Machine learning control for disruption and tearing mode avoidance.” *Physics of Plasmas*, **27**(2):022501, February 2020.
- [FKR79] S. Fornaca, Y. Kiwamoto, and N. Rynn. “Experimental Stabilization of Interchange Mode by Surface Line Tying.” *Phys. Rev. Lett.*, **42**:772–776, Mar 1979.
- [FLM06] A. Fasoli, B. Labit, M. McGrath, S. H. Müller, G. Plyushchev, M. Podestà, and F. M. Poli. “Electrostatic turbulence and transport in a simple magnetized plasma.” *Physics of Plasmas*, **13**(5):055902, May 2006.
- [Fri13] Brett Cory Friedman. *Simulation Analysis of Zero Mean Flow Edge Turbulence in LAPD*. PhD thesis, 2013.

- [FWD83] John R. Ferron, Alfred Y. Wong, Guy Dimonte, and Bernard J. Leikind. “Interchange stability of an axisymmetric, average minimum-  $B$  magnetic mirror.” *The Physics of Fluids*, **26**(8):2227–2233, August 1983.
- [GH71] G. E. Guest and E. G. Harris. “Flute Stabilization Via Electrostatically Confined Cold Electrons.” *Phys. Rev. Lett.*, **27**:1500–1503, Nov 1971.
- [GKG22] S. Ghazaryan, M. Kaloyan, W. Gekelman, Z. Lucky, S. Vincena, S. K. P. Tripathi, P. Pribyl, and C. Niemann. “Thomson scattering on the large plasma device.” *Review of Scientific Instruments*, **93**(8):083514, August 2022.
- [GLZ18] Ruiqi Gao, Yang Lu, Junpei Zhou, Song-Chun Zhu, and Ying Nian Wu. “Learning Generative ConvNets via Multi-grid Modeling and Sampling.” In *2018 IEEE/CVF Conference on Computer Vision and Pattern Recognition*, pp. 9155–9164, Salt Lake City, UT, USA, June 2018. IEEE.
- [Gol95] R.J. Goldston. *Introduction to Plasma Physics*. CRC Press, Boca Raton, 1995.
- [GPL16a] W. Gekelman, P. Pribyl, Z. Lucky, M. Drandell, D. Leneman, J. Maggs, S. Vincena, B. Van Compernolle, S. K. P. Tripathi, G. Morales, T. A. Carter, Y. Wang, and T. DeHaas. “The upgraded Large Plasma Device, a machine for studying frontier basic plasma physics.” *Review of Scientific Instruments*, **87**(2):025105, February 2016.
- [GPL16b] W. Gekelman, P. Pribyl, Z. Lucky, M. Drandell, D. Leneman, J. Maggs, S. Vincena, B. Van Compernolle, S. K. P. Tripathi, G. Morales, T. A. Carter, Y. Wang, and T. DeHaas. “The upgraded Large Plasma Device, a machine for studying frontier basic plasma physics.” *Review of Scientific Instruments*, **87**(2):025105, February 2016.
- [GPM14] Ian J. Goodfellow, Jean Pouget-Abadie, Mehdi Mirza, Bing Xu, David Warde-Farley, Sherjil Ozair, Aaron Courville, and Yoshua Bengio. “Generative Adversarial Networks.”, June 2014. arXiv:1406.2661 [stat].
- [GPS17] Chuan Guo, Geoff Pleiss, Yu Sun, and Kilian Q. Weinberger. “On Calibration of Modern Neural Networks.” <http://arxiv.org/abs/1706.04599>, August 2017. arXiv:1706.04599 [cs].
- [HBF84] Jr. Hooper, E. B., D. E. Baldwin, T. K. Fowler, R. J. Kane, and W. C. Turner. “Radial transport reduction in tandem mirrors using end-wall boundary conditions.” *The Physics of Fluids*, **27**(9):2264–2267, 09 1984.
- [Hin02] Geoffrey E. Hinton. “Training Products of Experts by Minimizing Contrastive Divergence.” *Neural Computation*, **14**(8):1771–1800, August 2002.
- [Hop82] J J Hopfield. “Neural networks and physical systems with emergent collective computational abilities.” *Proceedings of the National Academy of Sciences*, **79**(8):2554–2558, April 1982.

- [Hor99] W. Horton. “Drift waves and transport.” *Reviews of Modern Physics*, **71**(3):735–778, April 1999.
- [HPC05] W. Horton, Jean C. Perez, Troy Carter, and Roger Bengtson. “Vorticity probes and the characterization of vortices in the Kelvin–Helmholtz instability in the large plasma device experiment.” *Physics of Plasmas*, **12**(2):022303, February 2005.
- [IP13] A A Ivanov and V V Prikhodko. “Gas-dynamic trap: an overview of the concept and experimental results.” *Plasma Physics and Controlled Fusion*, **55**(6):063001, may 2013.
- [JAC22] Azarakhsh Jalalvand, Joseph Abbate, Rory Conlin, Geert Verdoolaege, and Egemen Kolemen. “Real-Time and Adaptive Reservoir Computing With Application to Profile Prediction in Fusion Plasma.” *IEEE Transactions on Neural Networks and Learning Systems*, **33**(6):2630–2641, June 2022.
- [JAM24] Alexis Juven, Marie-Hélène Aumeunier, and Julien Marot. “Generative Models and Simulation to Assess Uncertainties for Tokamak Infrared Thermography.” In *2024 IEEE 34th International Workshop on Machine Learning for Signal Processing (MLSP)*, pp. 1–6, London, United Kingdom, September 2024. IEEE.
- [Jas72] D. L. Jassby. “Transverse Velocity Shear Instabilities within a Magnetically Confined Plasma.” *The Physics of Fluids*, **15**(9):1590–1604, September 1972.
- [jax] “JAX: High-Performance Array Computing.”
- [JKC24] Samuel Jackson, Saiful Khan, Nathan Cummings, James Hodson, Shaun De Witt, Stanislas Pamela, Rob Akers, and Jeyan Thiyyagalingam. “FAIR-MAST: A fusion device data management system.” *SoftwareX*, **27**:101869, September 2024.
- [JKS24] Azarakhsh Jalalvand, SangKyeun Kim, Jaemin Seo, Qiming Hu, Max Curie, Peter Steiner, Andrew Oakleigh Nelson, Yong-Su Na, and Egemen Kolemen. “Multimodal Super-Resolution: Discovering hidden physics and its application to fusion plasmas.”, November 2024. arXiv:2405.05908 [physics].
- [Kan79] B.I. Kanaev. “Stabilization of drift loss-cone instability (DCI) by addition of cold ions.” *Nuclear Fusion*, **19**(3):347, mar 1979.
- [Kar19] Andrej Karpathy. “A Recipe for Training Neural Networks.” <https://web.archive.org/web/20240709000647/http://karpathy.github.io/2019/04/25/recipe/>, April 2019. Accessed: 2024-07-12.
- [KCP17] Igor A. Kotelnikov, Ivan S. Chernoshtanov, and Vadim V. Prikhodko. “Electrostatic instabilities in a mirror trap revisited.” *Physics of Plasmas*, **24**(12):122512, 12 2017.
- [KGL83] J Kesner, MJ Gerver, BG Lane, BD Vey, RE Aamodt, PJ Catto, DA Ippolito, and JR Myra. “Introduction to tandem mirror physics.” 1983.

- [KHS87] Akio Komori, Yoshiya Higuchi, Yusuke Suetsugu, Akira Yonesu, and Yoshinobu Kawai. “Flute Stabilization of a Mirror-Confining Plasma by a Positive Ambipolar Potential.” *Journal of the Physical Society of Japan*, **56**(8):2607–2610, 1987.
- [KLZ21] Igor Kotelnikov, Andrej Lizunov, and Qiusun Zeng. “On the stability of small-scale ballooning modes in axisymmetric mirror traps.” *Plasma Science and Technology*, **24**(1):015102, 11 2021.
- [KST19] Julian Kates-Harbeck, Alexey Svyatkovskiy, and William Tang. “Predicting disruptive instabilities in controlled fusion plasmas through deep learning.” *Nature*, **568**(7753):526–531, April 2019.
- [KW22] Diederik P. Kingma and Max Welling. “Auto-Encoding Variational Bayes.”, December 2022. arXiv:1312.6114 [stat].  
*[Comment: Fixes a typo in the abstract, no other changes.]*
- [LCH06] Yann LeCun, Sumit Chopra, Raia Hadsell, Marc’Aurelio Ranzato, and Fu Jie Huang. “A Tutorial on Energy-Based Learning.” p. 59, 2006.
- [Len22] Lennart van Rijn. *Minimizing neoclassical transport in the Wendelstein 7-X stellarator using variational autoencoders*. PhD thesis, Eindhoven University of Technology, July 2022.
- [lhd] “LHD experiment data repository.” doi:10.57451/lhd.analyzed-data.
- [Lie85] Paulett C. Liewer. “Measurements of microturbulence in tokamaks and comparisons with theories of turbulence and anomalous transport.” *Nuclear Fusion*, **25**(5):543–621, May 1985.
- [LPB17] Balaji Lakshminarayanan, Alexander Pritzel, and Charles Blundell. “Simple and Scalable Predictive Uncertainty Estimation using Deep Ensembles.” <http://arxiv.org/abs/1612.01474>, November 2017. arXiv:1612.01474 [cs, stat].
- [LPG] B G Logan, L J Perkins, and J D Gordon. “Mirror Advanced Reactor Study (MARS): executive summary and overview.”
- [MCT07] J. E. Maggs, T. A. Carter, and R. J. Taylor. “Transition from Bohm to classical diffusion due to edge rotation of a cylindrical plasma.” *Physics of Plasmas*, **14**(5):052507, 05 2007.
- [MII91] A. Mase, A. Itakura, M. Inutake, K. Ishii, J.H. Jeong, K. Hattori, and S. Miyoshi. “Control of the radial electric field and of turbulent fluctuations in a tandem mirror plasma.” *Nuclear Fusion*, **31**(9):1725, sep 1991.
- [MM97] J. E. Maggs and G. J. Morales. “Fluctuations associated with a filamentary density depletion.” *Physics of Plasmas*, **4**(2):290–299, February 1997.

- [MMC05] J. E. Maggs, G. J. Morales, and T. A. Carter. “An Alfvén wave maser in the laboratory.” *Physics of Plasmas*, **12**(1):013103, January 2005.
- [MPL20] Andrea Murari, Emmanuele Peluso, Michele Lungaroni, Riccardo Rossi, Michela Gelfusa, and JET Contributors. “Investigating the Physics of Tokamak Global Stability with Interpretable Machine Learning Tools.” *Applied Sciences*, **10**(19):6683, September 2020.
- [MRP24] Andrew Maris, Cristina Rea, Alessandro Pau, Wenhui Hu, Bingjia Xiao, Robert Granetz, Earl Marmar, the EUROfusion Tokamak Exploitation team, the Alcator C.-Mod team, the ASDEX Upgrade team, the DIII-D. team, the EAST team, and the TCV team. “Correlation of the L-mode density limit with edge collisionality.”, June 2024. arXiv:2406.18442 [physics].
- [NHH20] Erik Nijkamp, Mitch Hill, Tian Han, Song-Chun Zhu, and Ying Nian Wu. “On the Anatomy of MCMC-Based Maximum Likelihood Learning of Energy-Based Models.” *Proceedings of the AAAI Conference on Artificial Intelligence*, **34**(04):5272–5280, April 2020.
- [NHZ19] Erik Nijkamp, Mitch Hill, Song-Chun Zhu, and Ying Nian Wu. “Learning Non-Convergent Non-Persistent Short-Run MCMC Toward Energy-Based Model.”, November 2019. arXiv:1904.09770 [cs, stat].
- [NKB19] Preetum Nakkiran, Gal Kaplun, Yamini Bansal, Tristan Yang, Boaz Barak, and Ilya Sutskever. “Deep Double Descent: Where Bigger Models and More Data Hurt.” <http://arxiv.org/abs/1912.02292>, December 2019. arXiv:1912.02292 [cs, stat].
- [NW94] D.A. Nix and A.S. Weigend. “Estimating the mean and variance of the target probability distribution.” In *Proceedings of 1994 IEEE International Conference on Neural Networks (ICNN’94)*, pp. 55–60 vol.1, Orlando, FL, USA, 1994. IEEE.
- [Pas74] V.P. Pastukhov. “Collisional losses of electrons from an adiabatic trap in a plasma with a positive potential.” *Nuclear Fusion*, **14**(1):3–6, 1 1974.
- [PBD06] F. M. Poli, S. Brunner, A. Diallo, A. Fasoli, I. Furno, B. Labit, S. H. Müller, G. Plyushchev, and M. Podestà. “Experimental characterization of drift-interchange instabilities in a simple toroidal plasma.” *Physics of Plasmas*, **13**(10):102104, October 2006.
- [PFC19] A. Pau, A. Fanni, S. Carcangiu, B. Cannas, G. Sias, A. Murari, F. Rimini, and the JET Contributors. “A machine learning approach based on generative topographic mapping for disruption prevention and avoidance at JET.” *Nuclear Fusion*, **59**(10):106017, October 2019.

- [PMC22] Conor Perks, Saskia Mordijck, Troy Carter, Bart Van Compernolle, Stephen Vincena, Giovanni Rossi, and David Schaffner. “Impact of the electron density and temperature gradient on drift-wave turbulence in the Large Plasma Device.” *Journal of Plasma Physics*, **88**(4):905880405, August 2022.
- [PMK23] A Pavone, A Merlo, S Kwak, and J Svensson. “Machine learning and Bayesian inference in nuclear fusion research: an overview.” *Plasma Physics and Controlled Fusion*, **65**(5):053001, May 2023.
- [Pos66] R. F. Post. “Electrostatic instabilities in Finite Mirror-confined plasmas.” *Physics of Fluids*, **9**(4):730, 1966.
- [Pos87] R.F. Post. “The magnetic mirror approach to fusion.” *Nuclear Fusion*, **27**(10):1579, 10 1987.
- [Pow74] E.J. Powers. “Spectral techniques for experimental investigation of plasma diffusion due to polychromatic fluctuations.” *Nuclear Fusion*, **14**(5):749, nov 1974.
- [PUC10] P. Popovich, M. V. Umansky, T. A. Carter, and B. Friedman. “Analysis of plasma instabilities and verification of the BOUT code for the Large Plasma Device.” *Physics of Plasmas*, **17**(10):102107, October 2010.
- [QGP23a] Yuchen Qian, Walter Gekelman, Patrick Pribyl, Tom Sketchley, Shreekrishna Tripathi, Zoltan Lucky, Marvin Drandell, Stephen Vincena, Thomas Look, Phil Travis, Troy Carter, Gary Wan, Mattia Cattelan, Graeme Sabiston, Angelica Ottaviano, and Richard Wirz. “Design of the Lanthanum hexaboride based plasma source for the large plasma device at UCLA.” *Review of Scientific Instruments*, **94**(8):085104, August 2023.
- [QGP23b] Yuchen Qian, Walter Gekelman, Patrick Pribyl, Tom Sketchley, Shreekrishna Tripathi, Zoltan Lucky, Marvin Drandell, Stephen Vincena, Thomas Look, Phil Travis, Troy Carter, Gary Wan, Mattia Cattelan, Graeme Sabiston, Angelica Ottaviano, and Richard Wirz. “Design of the Lanthanum hexaboride based plasma source for the large plasma device at UCLA.” *Review of Scientific Instruments*, **94**(8):085104, 08 2023.
- [RBC11] D. D. Ryutov, H. L. Berk, B. I. Cohen, A. W. Molvik, and T. C. Simonen. “Magneto-hydrodynamically stable axisymmetric mirrorsa).” *Physics of Plasmas*, **18**(9):092301, 09 2011.
- [RME19] C. Rea, K.J. Montes, K.G. Erickson, R.S. Granetz, and R.A. Tinguely. “A real-time machine learning-based disruption predictor in DIII-D.” *Nuclear Fusion*, **59**(9):096016, September 2019.
- [RWB08] C.M. Roach, M. Walters, R.V. Budny, F. Imbeaux, T.W. Fredian, M. Greenwald, J.A. Stillerman, D.A. Alexander, J. Carlsson, J.R. Cary, F. Ryter, J. Stober, P. Gohil, C. Greenfield, M. Murakami, G. Bracco, B. Esposito, M. Romanelli, V. Parail, P. Stubberfield,

- I. Voitsekhovitch, C. Brickley, A.R. Field, Y. Sakamoto, T. Fujita, T. Fukuda, N. Hayashi, G.M.D Hogeweij, A. Chudnovskiy, N.A. Kinerva, C.E. Kessel, T. Aniel, G.T. Hoang, J. Ongena, E.J. Doyle, W.A. Houlberg, A.R. Polevoi, ITPA Confinement Database and Modelling Topical Group, and ITPA Transport Physics Topical Group. “The 2008 Public Release of the International Multi-tokamak Confinement Profile Database.” *Nuclear Fusion*, **48**(12):125001, December 2008.
- [Sch13] David Schaffner. *Study of Flow, Turbulence and Transport on the Large Plasma Device*. PhD thesis, 2013.
- [SCR12] D. A. Schaffner, T. A Carter, G. D. Rossi, D. S. Guice, J. E. Maggs, S. Vincena, and B. Friedman. “Modification of Turbulent Transport with Continuous Variation of Flow Shear in the Large Plasma Device.” *Physical Review Letters*, **109**(13):135002, September 2012.
- [SCR13] D. A. Schaffner, T. A. Carter, G. D. Rossi, D. S. Guice, J. E. Maggs, S. Vincena, and B. Friedman. “Turbulence and transport suppression scaling with flow shear on the Large Plasma Device.” *Physics of Plasmas*, **20**(5):055907, May 2013.
- [SH09] Ruslan Salakhutdinov and Geoffrey Hinton. “Deep Boltzmann Machines.” In David van Dyk and Max Welling, editors, *Proceedings of the Twelfth International Conference on Artificial Intelligence and Statistics*, volume 5 of *Proceedings of Machine Learning Research*, pp. 448–455, Hilton Clearwater Beach Resort, Clearwater Beach, Florida USA, 16–18 Apr 2009. PMLR.
- [Sim76] T. C. Simonen. “Measurements of ion cyclotron instability characteristics in a mirror-confined plasma.” *The Physics of Fluids*, **19**(9):1365–1370, 09 1976.
- [SKJ24] Jaemin Seo, SangKyeun Kim, Azarakhsh Jalalvand, Rory Conlin, Andrew Rothstein, Joseph Abbate, Keith Erickson, Josiah Wai, Ricardo Shousha, and Egemen Kolemen. “Avoiding fusion plasma tearing instability with deep reinforcement learning.” *Nature*, **626**(8000):746–751, February 2024.
- [SKR23] Rylan Schaeffer, Mikail Khona, Zachary Robertson, Akhilan Boopathy, Kateryna Pistunova, Jason W. Rocks, Ila Rani Fiete, and Oluwasanmi Koyejo. “Double Descent Demystified: Identifying, Interpreting & Ablating the Sources of a Deep Learning Puzzle.” <http://arxiv.org/abs/2303.14151>, March 2023. arXiv:2303.14151 [cs, stat].
- [SNK21] Jaemin Seo, Y.-S. Na, B. Kim, C.Y. Lee, M.S. Park, S.J. Park, and Y.H. Lee. “Feedforward beta control in the KSTAR tokamak by deep reinforcement learning.” *Nuclear Fusion*, **61**(10):106010, October 2021.
- [SNK22] J. Seo, Y.-S. Na, B. Kim, C.Y. Lee, M.S. Park, S.J. Park, and Y.H. Lee. “Development of an operation trajectory design algorithm for control of multiple 0D parameters using deep reinforcement learning in KSTAR.” *Nuclear Fusion*, **62**(8):086049, August 2022.

- [STA22] Maximilian Seitzer, Arash Tavakoli, Dimitrije Antic, and Georg Martius. “On the Pitfalls of Heteroscedastic Uncertainty Estimation with Probabilistic Neural Networks.” <http://arxiv.org/abs/2203.09168>, April 2022. arXiv:2203.09168 [cs, stat].
- [SWP20] Prem Seetharaman, Gordon Wichern, Bryan Pardo, and Jonathan Le Roux. “AutoClip: Adaptive Gradient Clipping for Source Separation Networks.” <http://arxiv.org/abs/2007.14469>, July 2020. arXiv:2007.14469 [cs, eess, stat].
- [TFM09] G R Tynan, A Fujisawa, and G McKee. “A review of experimental drift turbulence studies.” *Plasma Physics and Controlled Fusion*, **51**(11):113001, November 2009.
- [Tie08] Tijmen Tielemans. “Training restricted Boltzmann machines using approximations to the likelihood gradient.” In *Proceedings of the 25th international conference on Machine learning - ICML '08*, pp. 1064–1071, Helsinki, Finland, 2008. ACM Press.
- [tra] “Turbulence and transport in mirror geometries in the Large Plasma Device.” **91**.
- [Tra25] Phil Travis. “physicistphil/lapd-isat-predict: 2025-3-11.”, March 2025. doi:10.5281/zenodo.15007853.
- [VG06] Stephen Vincena and Walter Gekelman. “Drift-Alfvén wave mediated particle transport in an elongated density depression.” *Physics of Plasmas*, **13**(6):064503, June 2006.
- [VGP11] B. Van Compernolle, W. Gekelman, P. Pribyl, and C. M. Cooper. “Wave and transport studies utilizing dense plasma filaments generated with a lanthanum hexaboride cathode.” *Physics of Plasmas*, **18**(12):123501, 12 2011.
- [VMD22] J. Vega, A. Murari, S. Dormido-Canto, G. A. Rattá, M. Gelfusa, and JET Contributors. “Disruption prediction with artificial intelligence techniques in tokamak plasmas.” *Nature Physics*, **18**(7):741–750, July 2022.
- [Vos24] J M Vos. *Discovery of hidden Neoclassical Transport variables in Wendelstein 7-X through Variational AutoEncoder Latent Space Exploration*. PhD thesis, 2024.
- [VS22] Matias Valdenegro-Toro and Daniel Saromo. “A Deeper Look into Aleatoric and Epistemic Uncertainty Disentanglement.” 2022. arXiv:2204.09308 [cs.LG].
- [Wes87] J. Wesson. *4.9 - Radiation losses*, p. 100–101. Clarendon Press, 1987.
- [WH84] Masahiro Wakatani and Akira Hasegawa. “A collisional drift wave description of plasma edge turbulence.” *The Physics of Fluids*, **27**(3):611–618, 03 1984.
- [WLH21] Y. Wei, J.P. Levesque, C.J. Hansen, M.E. Mauel, and G.A. Navratil. “A dimensionality reduction algorithm for mapping tokamak operational regimes using a variational autoencoder (VAE) neural network.” *Nuclear Fusion*, **61**(12):126063, December 2021.

- [WV82] Michael Wickham and Guy Vandegrift. “Curvature-induced interchange mode in an axisymmetric plasma.” *The Physics of Fluids*, **25**(1):52–58, January 1982.
- [WYP22] Chenguang Wan, Zhi Yu, Alessandro Pau, Xiaojuan Liu, and Jiangang Li. “EAST discharge prediction without integrating simulation results.” *Nuclear Fusion*, **62**(12):126060, December 2022.
- [YMM10] M. Yoshikawa, Y. Miyata, M. Mizuguchi, N. Imai, H. Hojo, M. Ichimura, T. Kariya, I. Katanuma, Y. Nakashima, R. Minami, H. Shidara, Y. Yamaguchi, Y. Shima, Y. Ohno, F. Yaguchi, and T. Imai. “Use of a Gold Neutral Beam Probe to Study Fluctuation Suppression During Potential Formation in the GAMMA 10 Tandem Mirror.” *Fusion Science and Technology*, **57**(4):312–319, May 2010.
- [P20] Vít Škvára, Václav Šmídl, Tomáš Pevný, Jakub Seidl, Aleš Havránek, and David Tskhakaya. “Detection of Alfvén Eigenmodes on COMPASS with Generative Neural Networks.” *Fusion Science and Technology*, **76**(8):962–971, November 2020.